2-P

NAS 9-11540

CR 115-561

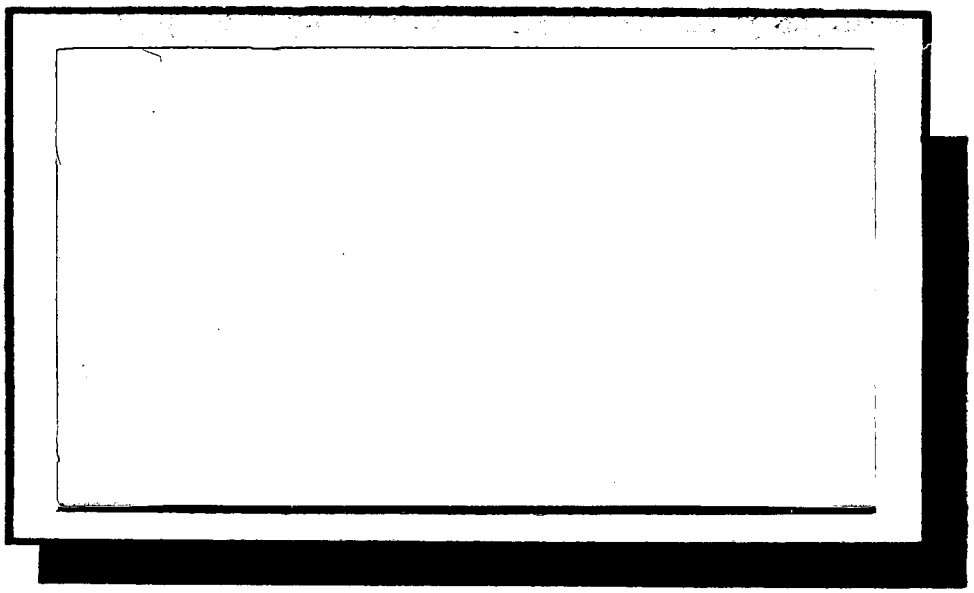

CENTER FOR SPACE RESEARCH
MASSACHUSETTS INSTITUTE OF TECHNOLOGY

N72-24160

PAGE 164

G3-07

OFFICE OF PRIME RESPONSIBILITY

EE3

Massachusetts Institute of Technology

Center for Space Research

Half Wavelength Dipole Antennas Over Stratified Media

CSR T-72-1 February 1972

by

Gerald A. La Torraca

Half Wavelength Dipole Antennas Over Stratified Media

by

Gerald A. La Torraca

ABSTRACT

In the Lunar Surface Electrical Properties experiment, radio frequency power is to be radiated through two multi-frequency, trapped, horizontal, electric field dipole antenna on the lunar surface. The magnetic field induced by these antennas is measured and recorded by a receiver mounted on the Lunar Roving Vehicle which traverses the lunar surface. The interference of reflected and direct waves is used to provide a measure of the subsurface electrical properties of the moon.

In this thesis, theoretical solutions of the fields induced by half-wavelength, horizontal, electric field dipoles (HEDs) are determined based on studies of infinitesimal, horizontal, electric field dipoles over low loss plane-stratified media by Annan,[1] Cooper,[2] and Sinha.[3] To determine these solutions, an approximation to the current distribution of a half-wavelength HED is derived and experimentally verified. Traverse and antenna measurements obtained on the Athabasca Glacier in the summer of 1971 are related to the characteristics of the transmitting antenna design, and the measurement techniques and field equipment used in the glacier trials are described and evaluated.

ACKNOWLEDGEMENTS

I wish to thank my Thesis Advisors, Professor Walter Wrigley of the Department of Aeronautics and Astronautics and Mr. Richard H. Baker of the Laboratory for Space Experiments for their assistance and encouragement throughout my thesis study.

I also wish to thank Professor M. Gene Simmons of the Department of Earth and Planetary Sciences (EPS) for his continued support and assistance.

I wish to thank E. John Groener of the Laboratory for Space Experiments (LSE) for providing the computer programs used in this thesis.

I also wish to thank Ved P. Nanda and William W. Cooper, respectively of LSE and the University of Rhode Island, for their thoughtful suggestions regarding the technical content of the thesis. I also want to thank Lawrence H. Bannister of LSE for his thoughtful suggestions regarding the content and presentation of this thesis.

I wish to thank all of the members of LSE and EPS for their efforts in preparation for the summer field trials for the SEP experiment and I also wish to thank James R. Rossiter, Professor David W. Strangway and Raymond D. Watts of the NASA Manned Spacecraft Center, (on leave from the University of Toronto), for providing printouts of data obtained during the field trials.

I wish to thank Mary E. De Sesa and Jennifer M. Kelley of LSE for typing this manuscript.

TABLE OF CONTENTS

Page No.

APPENDICES

LIST OF ILLUSTRATIONS

LIST OF TABLES

GLOSSARY OF TERMS

Electromagnetic Field Terms

Symbol	Quantity	Units
$\underline{B}$	Magnetic Flux Density	weber/square meter
$\underline{D}$	Electric Flux Density (dielectric displacement)	coulomb/square meter
$\underline{E}_i$	Electric Field Intensity (in any layer)	volt/meter
$\underline{H}_i$	Magnetic Field Intensity (in any layer)	ampere-turn/meter
$\underline{J}$	Current Density	ampere/square meter
$\rho(\omega)$	Charge Density	coulomb/cubic meter
$H\rho$	Radial Magnetic Field Intensity	ampere-turn/meter
$H\phi$	Tangential Mangetic Field Intensity	ampere-turn/meter
H_z	Vertical Magnetic Field Intensity	ampere-turn/meter

Coordinate System Terms

Symbol	Quantity	Units
$\underline{u}_z$	Vertical Unit Vector	
$\underline{u}_r$	Radial Unit Vector	
$\underline{u}_t$	Tangential Unit Vector	
γ	Angle between Transverse Propagation Vector and X axis in polar coordinates	degrees (or radians)
ψ	Angle between Transverse Propagation Vector and Radial Unit Vector	degrees (or radians)
ϕ	Bearing Angle (Measured with respect to Transmitting Antenna)	degrees (or radians)

Coordinate System Terms (cont'd)

Symbol	Quanity	Units
θ	Angle measured with respect to Z axis in spherical coordinates	degrees (or radians)
X	Distance along Horizontal Axis co-linear with the Transmitting Antenna	meters
Y	Horizontal Distance Perpendicular to the Line of the Transmitting Antenna	meters
Z	Vertical Distance Perpendicular to the Line of the Transmitting Antenna	meters
r	Radial Distance from the center of the Transmitting Antenna in Polar Coordinates	meters
R	Radial Distance from the Center of the Transmitting Antenna in Spherical Coordinates	meters

Electrical Properties

Symbol	Quantity	Units
ε_i	Permittivity of Layer i	farad/meter
M_i	Permeability of Layer i	henry/meter
tan δ	Loss Tangent	
K_{ε_i}	Dielectric Constant for Layer i	
$K_{\varepsilon_{eff}}$	Effective Dielectric Constant	
ε_{eff}	Effective Permittivity	farad/meter
	Wave Propagation Terms	
λ_o	Free Space Wavelength	meters
λ_i	Wavelength in Layer i	meters
λ_{eff}	Effective Wavelength	meters

Electrical Properties (cont'd)

Symbol	Quantity	Units
ω	Angular Frequency	radians/second
k_{c_i}	Medium Propagation Constant	radians/meter
k_i	Vertical Component of Medium Propagation Constant	radians/meter
k_t	Transverse Component of Medium Propagation Constant	radians/meter
k_{eff}	Effective Medium Propagation Constant	radians/meter
η_i	Transverse Wave Impedance	
(+)	Upward Travelling Waves	
(-)	Downward Travelling Waves	

Current Distribution Terms

Symbol	Quantity	Units
I(x)	Antenna Current Distribution[5]	ampere/meter
V_o	Antenna Driving Point Voltage	volts
$\sqrt{\varepsilon_r}$	Dielectric Constant of Dissipative Medium [5]	
ζ_o	Free Space Wave Impedance[5] for Plane Waves	ohms
ψ_{v_2}	Current Distribution Constant[5]	
ψ_u	Current Distrubution Constant[5]	
$\psi_c(\lambda/4)$	Current Distribution Term[5]	
$W(\lambda/4)$	Current Distribution Term[5]	
a	Current Distribution Coefficient (cosinusoidal term)	amperes/volt
b	Current Distribution Coefficient (non-cosinusoidal term)	amperes/volt

Current Distribution Terms (cont'd)

Symbol	Quantity	Units
c	Current Distribution Coefficient (cosinusoidal term)	amperes/volt
d	Current Distribution Coefficient (non-cosinusoidal term)	amperes/volt
I_i	Absolute-Value Current Distribution Term (cosinusoidal)	amperes/volt
I_2	Absolute Value Current Distribution Term (non-cosinusoidal)	amperes/volt
ψ_1	Phase between Driving Voltage and Current (cosinusoidal term)	
ψ_2	Phase between Driving Voltage and Current (non-cosinusoidal term)	

Radiation Pattern Terms

$dP/d\Omega_i$	Power per unit of Solid Angle	watts/square radian
P_i	Power	watts
G^I	Gain of Infinitesimal HED	
G	Gain of Half Wavelength HED	
M_i^ζ	Array Factor Term (cosinusoidal current)	
N_i	Array Factor Term (non-cosinusoidal current)	
O_i	Array Factor Term (non-cosinusoidal current)	

Mathematical Terms Related to Field Solutions

$\underline{a}_t$	Transverse Excitation Current for Infinitesimal HED	amperes/ cubic meter
$\delta(x)$	Delta-Dirac Function	
$J_i(K_t r)$	Bessel Function of order i	
Φ	Half Space Stationary Phase Term	
Φ_n	Stationary Phase Term for Three-Layer Geometry	

Chapter 1

Introduction

1.0 Description of the Surface Electrical Properties Experiment

The Surface Electrical Properties (SEP) experiment planned for Apollo 17 is designed to use a radio frequency (RF) interferometry technique[1] to determine the dielectric constant and loss tangent of the lunar subsurface, to determine the thickness of electrically contrasting subsurface layers, and to provide a measure of the subsurface scattering of RF energy. The radio frequency interferometry technique consists of the measurement of interfering fields induced by sources at or near the interface between two contrasting dielectric media.

For the SEP application, six radio frequencies are radiated sequentially through two alternately energized, orthogonal, multi-frequency, horizontal, electric field dipole antennas deployed on the lunar surface. The transmitting antennas are effectively half wavelength at each frequency. Reception for the induced fields is provided by a tri-loop antenna-receiver system synchronized with the transmitter and mounted at the rear of the Lunar Rover. Measurements of the induced fields are recorded automatically as the Lunar Rover traverses the Lunar surface as illustrated in Figure 1-1.

1.1 Purpose of Thesis

Knowledge of the nature of the fields induced by the transmitting antennas is necessary for the proper interpretation

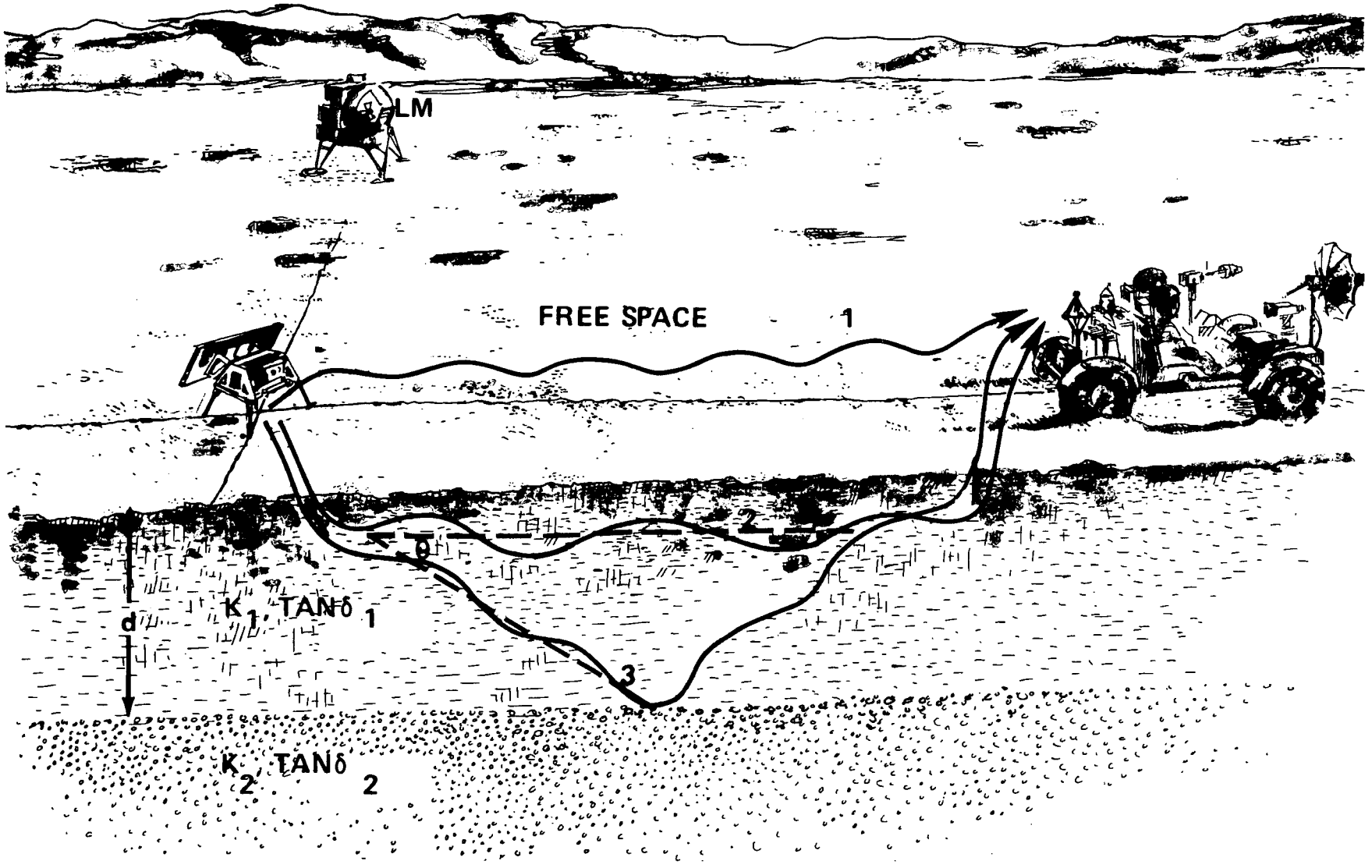

Fig. 1 The SEP transmitter is deployed about 200 meters from the LM and its orthogonal dipoles reeled out. The receiver on the LRV picks up the signal produced by propagation over the three paths shown in section: Path 1 in free space, Path 2 in the lunar regolith, and Path 3 produced by a reflection from a second layer at depth d.

of radio interferometry data. The purpose of this thesis is to formulate the field solutions for a half wavelength, horizontal, electric field dipole (HED) antenna deployed on the surface of a dielectric, plane-stratified medium. The field solutions for a half wavelength HED are based on a theoretically derived[5,6] and experimentally verified distribution of current along the antenna length in conjunction with a theoretical solution[2] for an infinitesimal HED over plane-stratified dielectric media.

1.2 Historical Background

The radio interferometry technique was suggested as a method for sounding glaciers by Stern in 1927. The technique was used to determine the depth to the water table of a desert by El Said in 1956 and was used by Hermance in 1968 to depth sound the Divide Glacier in the Yukon. However, the first rigorous theoretical study of the radio interferometry technique was published in 1970 by Annan who determined the field solutions for infinitesimal horizontal electric and vertical magnetic field dipoles over stratified media and applied these solutions to the analysis of radio frequency interferometry data obtained on the Gorner Glacier (1969) in Switzerland and from laboratory scale model studies. Annan's theoretical results were extended by Cooper[2] in 1971. Cooper's field solutions include the radiation patterns and surface fields induced by an infinitesimal horizontal electric field dipole over a dielectric half space and are used in this thesis

to determine the field solutions for the near half wavelength SEP antennas.

1.3 Results of the Thesis

The solution for the surface fields and radiation patterns for a half wavelength HED antenna is determined in this thesis by replacing the delta function current density in Cooper's formulation[2] with a current distribution approximation based on studies by King[5] and Tsao.[6] The results are:

1. The transmitting antenna can be considered to be a half wavelength dipole in a medium whose dielectric constant is the average of the dielectric constants of the media above and below the antenna.
2. The current distribution for a half wavelength HED antenna can be approximated as a simple cosinusoidal distribution only for low loss tangents ($\tan\delta < 0.05$).
3. A closed form array factor is derived by which the radiation patterns of a half wavelength HED antenna are related to the radiation patterns of an infinitesimal HED.
4. The effect of the finite length of the half wavelength dipole antenna is to decrease TM subsurface radiation and to increase TE subsurface radiation.
5. The symmetry of the radiation patterns for the half wavelength dipole is the same as that of the

infinitesimal dipole, that is, TE and TM radiation pattern lobes exist in orthogonal azimuthal planes.

6. The surface fields for the half wavelength dipole are proportional to R^{-2} as are the surface fields for the infinitesimal dipole. However, the beam widths of the circular surface field patterns for the half wavelength dipole are narrower for TE fields and broader for TM fields.

Field trials using the radio frequency interferometry technique have been conducted on a large scale dielectric, the Athabasca Glacier in Alberta, Canada. The results of measurements designed to determine the characteristics of the transmitting antennas deployed on the glacier, and to calibrate the receiving antennas attached to an instrumented vehicle are:

1. The measured amplitudes of the current distribution of the multi-frequency HED antenna are approximately cosinusoidal. This trait is consistent with minimal phase variations along the length of the antenna.
2. The large reactive,non-radiating, impedance terms measured at the driving point of the transmitting antenna at the higher frequencies (shorter wavelengths) are indications of the roughness of the glacier surface and the sensitivity of the impedance to the position of isolating circuits (traps and suppressors) along the length of the antenna.

3. The reception pattern of each receiving loop antenna for rotation in the plane of the loop are not constant as in free space but are azimuthally symmetric.

1.4 Outline of Thesis

In the following chapters, the results listed in Section 1.3 are obtained. In Chapter 2 the determination of the fields induced by an infinitesimal HED over a stratified medium are described to provide the necessary background for the determination of the fields induced by a half wavelength HED antenna. In Chapter 3, the results of Chapter 2 in conjunction with a current distribution formulation are used to determine the fields induced by a half wavelength HED antenna over a stratified medium. In Chapter 4, the equipment used to gather radio frequency interferometry data for the SEP experiment is described. In Chapter 5, antenna measurements and radio frequency interferometry measurements conducted on the Athabasca Glacier during the summer of 1971 SEP field trials are described and related to the results of Chapter 2 and 3.

Chapter 2

The Electromagnetic Fields of an Infinitesimal Horizontal Electric Field Dipole Over Stratified Media

2.0 Introduction

The solution of the electromagnetic fields of a harmonically excited, horizontal, electric field dipole (HED) over stratified media has been studied by many authors since 1909. The list of writers includes: Annan,[1] Cooper,[2] Sinha,[3] Sommerfeld,[4] Van der Pol,[9] Wait,[10] Collin,[11] and Baños.[12] Cooper solved the specific problems of determining the radiation patterns and surface fields of various types of infinitesimal dipoles at the interface between two dielectric media.

Cooper's solutions encompass only the infinitesimal dipole fields and can be used as the basis for the study of the field formulations of practical, finite-size antennas. The primary purpose of this chapter is to review the approach used by Cooper. The far field and surface field solutions of the vertical magnetic field component (H_z) of an infinitesimal HED deployed at the interface between two dielectric half spaces are formulated in the following sections. This interface is designated as the surface in the remainder of the text. The purpose of formulating these solutions is to provide the necessary background for the determination of the radiation patterns and the surface fields of finite length HED antennas.

These solutions are shown to have the following salient characteristics:

1. Half-space surface fields are proportional to $1/R^2$
2. Far field are asymptotically proportional to $1/R$
3. TE fields vary azimuthally as $\sin \phi$
4. TM fields vary azimuthally as $\cos \phi$

2.1 Conceptual Description

The infinitesimal HED is assumed to be a Hertzian dipole deployed on the surface of an isotropic, planar stratified medium. The general approach used to find the field solutions is to assume a transverse current at the surface and solve the boundary conditions for the electric fields $\underline{E}$ and the magnetic fields $\underline{H}$. Since plane waves can be represented by wave numbers and a spherical wave can be represented by an infinite sum of plane waves, the excitation fields of a transverse current at the surface are decomposed into transverse electric (TE) and transverse magnetic (TM) fields with the transverse wave number $\underline{k}_t$ parallel to the excitation current density $\underline{a}_t$ for purely TM waves and $\underline{k}_t$ perpendicular to $\underline{a}_t$ for purely TE waves. The $\underline{E}$ and $\underline{H}$ fields are decomposed into TE and TM waves, since the boundary conditions for TE waves are independent of the boundary conditions for TM waves.

The transverse current density $\underline{J}$ is characterized as a delta-Dirac function of area $\underline{a}_t$. A spacial Fourier transform technique is used to allow the determination of the $\underline{E}$

and $\underline{H}$ fields in the k-space or wave number domain. The $\underline{E}$ and $\underline{H}$ fields are determined in the wave number domain by translating the current density $\underline{J}$ into components of the $\underline{E}$ and $\underline{H}$ fields in k-space and by performing the integrations of the k-space Fourier transform. The $\underline{E}$ and $\underline{H}$ fields are determined in the far field by applying a stationary phase approximation and a Fresnel integral identity to the integration operations of the k-space Fourier transforms.

The half-space surface fields (induction fields at the surface) are obtained by constraining the validity of the k-space integrals to the surface and by performing a geometric series approximation to the integrands of the k-space integrals. The geometric series is expanded about the singularities of the integrand, because the singularities of the integrand are the major contributors to the value of the integral. The final steps in the determination of the surface fields involve the substitution of derivatives of the Green's function which are equivalent to the k-space integrals at the surface.

The half-space radiation patterns for an infinitesimal HED are obtained by using the lowest order far field solutions for the determination of the Poynting vector. The Poynting vector is decomposed into the TM and TE modes of radiation.

The half-space solutions outlined above can be applied to the solution of an infinitesimal HED over stratified media by the use of a propagation matrix by which the fields in each layer are related to the excitation fields at the surface.

The propagation matrix contains the transmission and reflection coefficients at each interface, and the fields at the surface due to reflections from subsurface interfaces are superimposed upon the half-space solutions.

2.2 A Half-Space Field Solution

2.2.1 Introduction

In the following sections of this chapter, the far field solutions for the vertical magnetic field (H_z) of an infinitesimal HED at the surface are determined. The purpose of providing this example is to gain insight into Cooper's field solutions, and to provide the necessary background material for the study of finite-length HED's over stratified media.

2.2.2 Description of Notation and Assumptions

The solution for the fields associated with an infinitesimal HED involves the solution of Maxwell's equations for a given source distribution. The current density of an infinitesimal HED at the surface (illustrated in Figures 2-1A and 2-1B) can be represented by the equation:

$$\underline{J} = \underline{a}_t \, e^{-j \underline{k}_t \cdot \underline{r}} \, \delta(x)\delta(y)\delta(z) \qquad (2\text{-}1)$$

where

$$\underline{a}_t = \mathrm{Re}\left[A(\omega) \, e^{j\omega t} \right] \qquad (2\text{-}2)$$

Maxwell's equations for a time-harmonic, transverse current source, are:

$$\nabla \times \underline{E} = -j\omega \underline{B} \tag{2-3}$$

$$\nabla \times \underline{H} = j\omega \underline{D} + \underline{J} \tag{2-4}$$

$$\nabla \cdot \underline{D} = \rho(\omega) \tag{2-5}$$

$$\nabla \cdot \underline{B} = 0 \tag{2-6}$$

and the equation of continuity is:

$$-j\omega\rho = \nabla \cdot \underline{J} \tag{2-7}$$

All stratified media are assumed to be homogeneous and isotropic and the electric flux density vector $\underline{D}$ and the magnetic flux density vector $\underline{B}$ are related to the $\underline{E}$ and $\underline{H}$ fields by the equations:

$$\underline{D} = \epsilon_i \underline{E} \tag{2-8}$$

$$\underline{B} = \mu_i \underline{H} \tag{2-9}$$

$$(i = -n \ldots -2, -1, 1, 2, \ldots n)$$

The propagation constants are related by the equation:

$$K_i = \sqrt{K_{c_i}^2 - K_t^2} \tag{2-10}$$

where $$K_{c_i} = \omega\sqrt{\mu_i \epsilon_i} \tag{2-11}$$

and $$K_t = (K_x, K_y, 0) \tag{2-12}$$

$$K_i \triangleq K_{z_i} \tag{2-13}$$

The vector relationships of the propagation constants are illustrated in Figures (2-1A) and (2-1B). All $\underline{E}$ and $\underline{H}$ fields are assumed to have the same transverse spacial harmonicity ($k_t = k_{ti}$) in each layer, and the $\underline{E}$ and $\underline{H}$ fields are described by the equations:

$$\underline{H} = \underline{H}_i^+ e^{-j(\underline{k}_t \cdot \underline{r} + K_{z_i} z)} + \underline{H}_i^- e^{-j(\underline{k}_t \cdot \underline{r} - K_{z_i} z)} \tag{2-14}$$

$$\underline{E} = \underline{E}_i^+ e^{-j(\underline{K}_t \cdot \underline{r} + K_{z_i} z)} + \underline{E}_i^- e^{-j(\underline{K}_t \cdot \underline{r} - K_{z_i} z)} \tag{2-15}$$

where "+" is used for upward propagation and "-" is used for downward propagation.

The propagation vector is described by the equation:

$$\underline{K}_{c_i}^{\pm} = \underline{K}_t \pm \underline{u}_z K_{z_i} \tag{2-16}$$

Accordingly, Maxwell's equations for TE and TM $\underline{E}$ and $\underline{H}$ fields can be written in the form:

$$\underline{K}_{c_i}^{\pm} \times \underline{E}_i^{\pm} = \omega \mu_i \underline{H}_i^{\pm} \tag{2-17}$$

$$K_{c_i}^{\pm} \times \underline{H}_i^{\pm} = \omega \epsilon_i \underline{E}_i^{\pm} \tag{2-18}$$

From equations (2-17) and (2-18), $\underline{k}_{ci}^{\pm}$, $\underline{E}_i^{\pm}$ and $\underline{H}_i^{\pm}$ are seen to be mutually orthogonal vectors.

Combining equation (2-10) with equations (2-17) and (2-18), the following relationship is obtained:

$$\left| \frac{\underline{E}_i}{\underline{H}_i} \right| = \sqrt{\frac{\underline{H}_i}{\epsilon_i}} \tag{2-19}$$

For TE waves as illustrated in Figure (2-1A), equation (2-19) can be written in the form:

$$\left| \frac{E_i}{H_{i,t} \frac{K_{c_i}}{K_{z_i}}} \right| = \sqrt{\frac{\mu_i}{\epsilon_i}} \tag{2-20}$$

$$\left| \frac{E_{i,t}}{H_{i,t}} \right| = \frac{K_{c_i}}{K_{z_i}} \sqrt{\frac{\mu_i}{\epsilon_i}} = \frac{\omega \mu_i}{K_{z_i}} \tag{2-21}$$

and for TM waves as illustrated in Figure (2-1B), equation

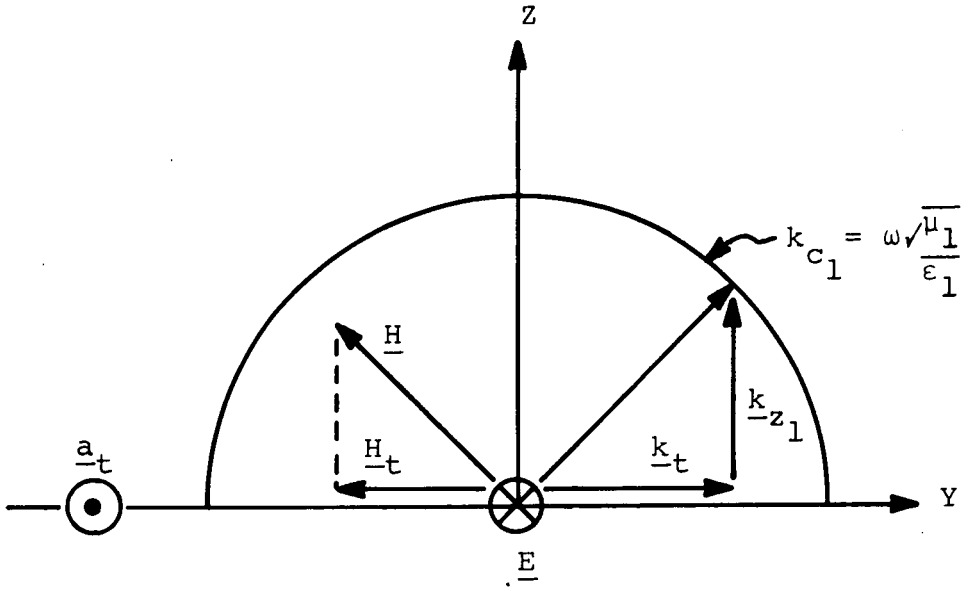

Figure 2-1A TE Fields

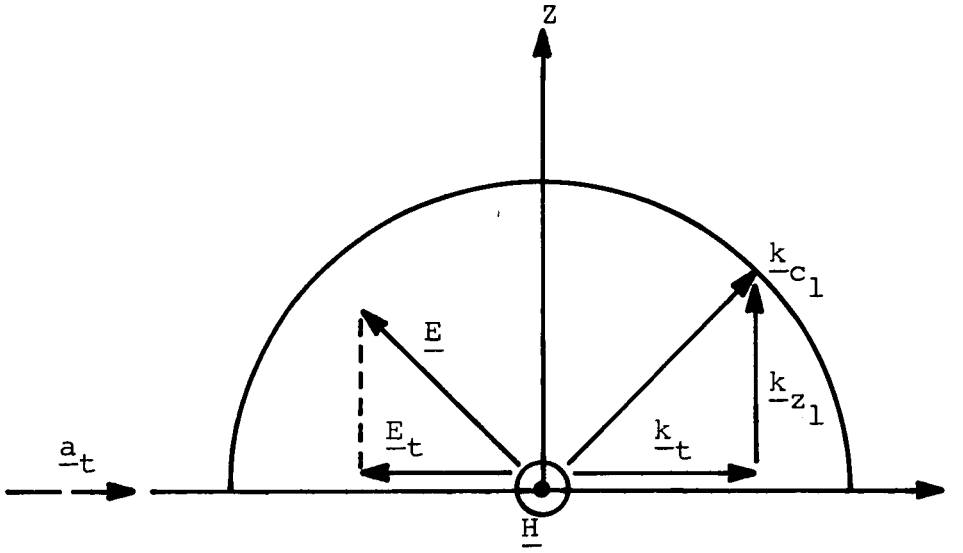

Figure 2-1B TM Fields

(2-19) can be written in the form:

$$\left| \frac{E_{i,t} \frac{K_{ci}}{K_{z_i}}}{H_i} \right| = \sqrt{\frac{M_i}{\epsilon_i}} \qquad (2\text{-}22)$$

$$\left| \frac{E_{i,t}}{H_{i,t}} \right| = \frac{K_{z_i}}{\omega \epsilon_i} \qquad (2\text{-}23)$$

Combining equations (2-21) and (2-23), the transverse impedance may be described as:

$$\eta_i = \left| \frac{E_{i,t}}{H_{i,t}} \right| = \left\{ \begin{array}{l} \frac{\omega M_i}{K_{z_i}} \text{ , TE} \\ \frac{K_{z_i}}{\omega \epsilon_i} \text{ , TM} \end{array} \right\} \qquad (2\text{-}24)$$

The boundary conditions for fields at the surface are used to determine the excitation fields. The tangential component of the electric field density $\underline{E}$ is continuous across the surface boundary, i.e.

$$E_{+1,t} - E_{-1,t} = 0 \qquad (2\text{-}25)$$

but the magnetic field intensity is discontinuous at this boundary because a current exists on the surface. As shown in Appendix A-1, the tangential (or transverse) components of the magnetic field at the surface may be represented by the equation:

$$\underline{H}_{+1,t} - \underline{H}_{-1,t} = -\underline{u}_z \times \underline{q}_t \tag{2-26}$$

By combining equation (2-24) with the transverse impedance equation (2-23), the following equation is obtained:

$$\eta_1 \underline{H}_{+1,t} - \eta_{-1} \underline{H}_{-1,t} = 0 \tag{2-27}$$

Since each field component consists of upward and downward propagating waves, equations (2-16) and (2-17) can be put in the form:

$$\underline{E}_i^{\pm} = \pm \eta_{i,(TE,TM)} \underline{H}_i^{\pm} \times \underline{u}_z \tag{2-28}$$

and equations (2-26) and (2-27) can be put in the form:

$$\left(H_{+1,t}^{+} + H_{+1,t}^{-}\right) - \left(H_{-1,t}^{+} + H_{-1,t}^{-}\right) = -\underline{u}_z \times \underline{q}_t \tag{2-29}$$

and

$$\eta_1 \left(\underline{H}_{+1,t}^{+} - \underline{H}_{+1,t}^{-}\right) - \eta_1 \left(\underline{H}_{-1,t}^{+} - \underline{H}_{-1,t}^{-}\right) = 0 \tag{2-30}$$

From equations (2-13) and (2-14), the tangential $\underline{E}$ and $\underline{H}$ fields can be written in the form:

$$\underline{H}_{i,t} = H_{i,t}^{+} + H_{i,t}^{-} \tag{2-31}$$

and $$\underline{E}_{i,t} = \underline{E}^{+}_{i,t} + \underline{E}^{-}_{i,t} \qquad (2\text{-}32)$$

Equations (2-29) and (2-30) together with equations (2-31) and (2-32) can be expressed in matrix form and inverted to obtain the matrix equation:

$$\begin{bmatrix} H_{+1,t} \\ H_{-1,t} \end{bmatrix} = \frac{\begin{bmatrix} \Pi_1 & 1 \\ -\Pi_1 & 1 \end{bmatrix}}{(\Pi_1 + \Pi_{-1})} \begin{bmatrix} \underline{u}_z \times \underline{a}_t \\ 0 \end{bmatrix} \qquad (2\text{-}33)$$

The vertical magnetic field component $\underline{H}^{\pm}_{i,z}$ is related to the tangential magnetic field component parallel to the transverse propagation vector $\underline{k}_t$ by the equation:

$$H^{\pm}_{i,z} = \pm \frac{K_t}{K_{z_i}} \operatorname{sign}\left(H_{i,t} \cdot \underline{u}_t\right) H_{i,t} \qquad (2\text{-}34)$$

where $$\underline{u}_t = \frac{\underline{k}_t}{K_t} \qquad (2\text{-}34A)$$

The current density $\underline{J}$ may be described by a delta-Dirac function in the real space domain or a constant in the k-space domain. The vertical magnetic field components can be obtained from the tangential field components by applying equation (2-34)

and the current density $\underline{J}$ is Fourier transformed in two dimensions only, as illustrated in equation (2-35).

$$\tilde{J}(k_x, k_y) = \int_{-\infty}^{\infty}\int_{-\infty}^{\infty} J(x,y) e^{j\underline{k}_t \cdot \underline{r}} \, dx\, dy = \underline{a}_t \tag{2-35}$$

The two dimensional Fourier transforms of the $\underline{E}$ and $\underline{H}$ fields from k-space to real space are described by the equation:

$$\begin{Bmatrix} E_i(r) \\ H_i(r) \end{Bmatrix} = \frac{1}{(2\pi)^2} \int_{-\infty}^{\infty}\int_{-\infty}^{\infty} \begin{Bmatrix} E_i(k_x, k_y, z) \\ H_i(k_x, k_y, z) \end{Bmatrix} e^{-j\underline{k}_t \cdot \underline{r}} \, dk_x\, dk_y \tag{2-36}$$

When equation (2-36) is written in a set of cylindrical coordinates (k_t, γ) as illustrated in Figure 2-2, the transform equation becomes:

$$\begin{Bmatrix} E_i(r) \\ H_i(r) \end{Bmatrix} = \frac{1}{(2\pi)^2} \int_{k_t=0}^{\infty} dk_t\, k_t e^{-jk_i z} \int_0^{2\pi} \begin{Bmatrix} E_i(k_t) \\ H_i(k_t) \end{Bmatrix} e^{-jk_t r \cos\psi} \, d\psi \tag{2-37}$$

2.2.3 The Solution for the H_z Component in Medium +1, $z \geq 0$ Far from the Source

By solving equation (2-37) for a transverse current

source, each component of the electromagnetic field is obtained. The analytical approach to the solution of each component of the $\underline{E}$ and $\underline{H}$ fields is the same and only the solution for the $H_{1,z}$ field component is presented below.

By combining equations (2-33) and (2-34) in section 2.2.2 for $z > 0$ ($i = 1$), the vertical magnetic field in k-space is represented by the equation:

$$\tilde{H}_{+1,z} = -\frac{K_t}{K_1}\left(\frac{\Pi_{-1}}{\Pi_1 + \Pi_{-1}}\right)\left(a_t \sin\gamma\right) \tag{2-38}$$

Applying equation (2-24) for a TE wave, equation (2-38) becomes:

$$\tilde{H}_{+1,z} = -\frac{H_{-1} K_1}{H_{-1} K_1 + H_1 K_{-1}}\left(\frac{K_t}{K_1}\right)\left(a_t \sin\gamma\right) \tag{2-39}$$

and substituting equation (2-39) into equation (2-37):

$$H_{1,z}(\rho) = \frac{1}{(2\pi)^2}\int_{K_t=0}^{\infty} dK_t\, K_t\, e^{-jK_1 z}\int_0^{2\pi}\left(\frac{H_{-1} K_t}{H_{-1}K_1 + H_1 K_{-1}}\right)\left(a_t \sin\gamma\right) e^{-jK_t\rho\cos\psi}\, d\psi \tag{2-40}$$

The last exponential term in equation (2-40) can be written as an infinite series of Bessel functions represented by equation (2-41).

$$e^{-jK_t\rho\cos\psi} = J_0(K_t\rho) - j2J_1(K_t\rho)\cos\gamma - 2J_2(K_t\rho)\cos 2\gamma - \cdots \tag{2-41}$$

where $$\gamma = \phi + \psi \tag{2-42}$$

$$\cos\gamma = \cos\phi\cos\psi - \sin\phi\sin\psi \tag{2-43}$$

$$\sin\gamma = \sin\phi\cos\psi + \cos\phi\sin\psi \tag{2-44}$$

$$\left\{\begin{matrix}\cos^2\psi \\ \sin^2\psi\end{matrix}\right\} = \frac{1 \pm \cos 2\psi}{2} \tag{2-45}$$

The angular relationships between ψ, γ, and ϕ are illustrated in Figure (2-2). Substituting equation (2-41) into equation (2-40) and using the integral relationship:

$$\frac{1}{2\pi}\int_0^{2\pi} d\psi \cos m\psi \cos n\psi = \left\{\begin{matrix} 0 & m \neq n \\ \frac{1}{2} & m = n \neq 0 \\ 1 & m = n = 0 \end{matrix}\right\} \tag{2-46}$$

equation (2-40) becomes:

$$H_{1,2}(r) = \frac{a_t \sin\phi}{2\pi}\int_{K_t=0}^{\infty} K_t\left(\frac{H_{-1}K_t}{H_1K_1 + H_1K_{-1}}\right) j\,\overline{J}_1(K_t r)\,dK_t \tag{2-47}$$

Letting

$$F(K_t) = \frac{1}{2} a_t \sin\phi \left(\frac{H_{-1}K_t}{H_{-1}K_1 + H_1K_{-1}}\right) \tag{2-48}$$

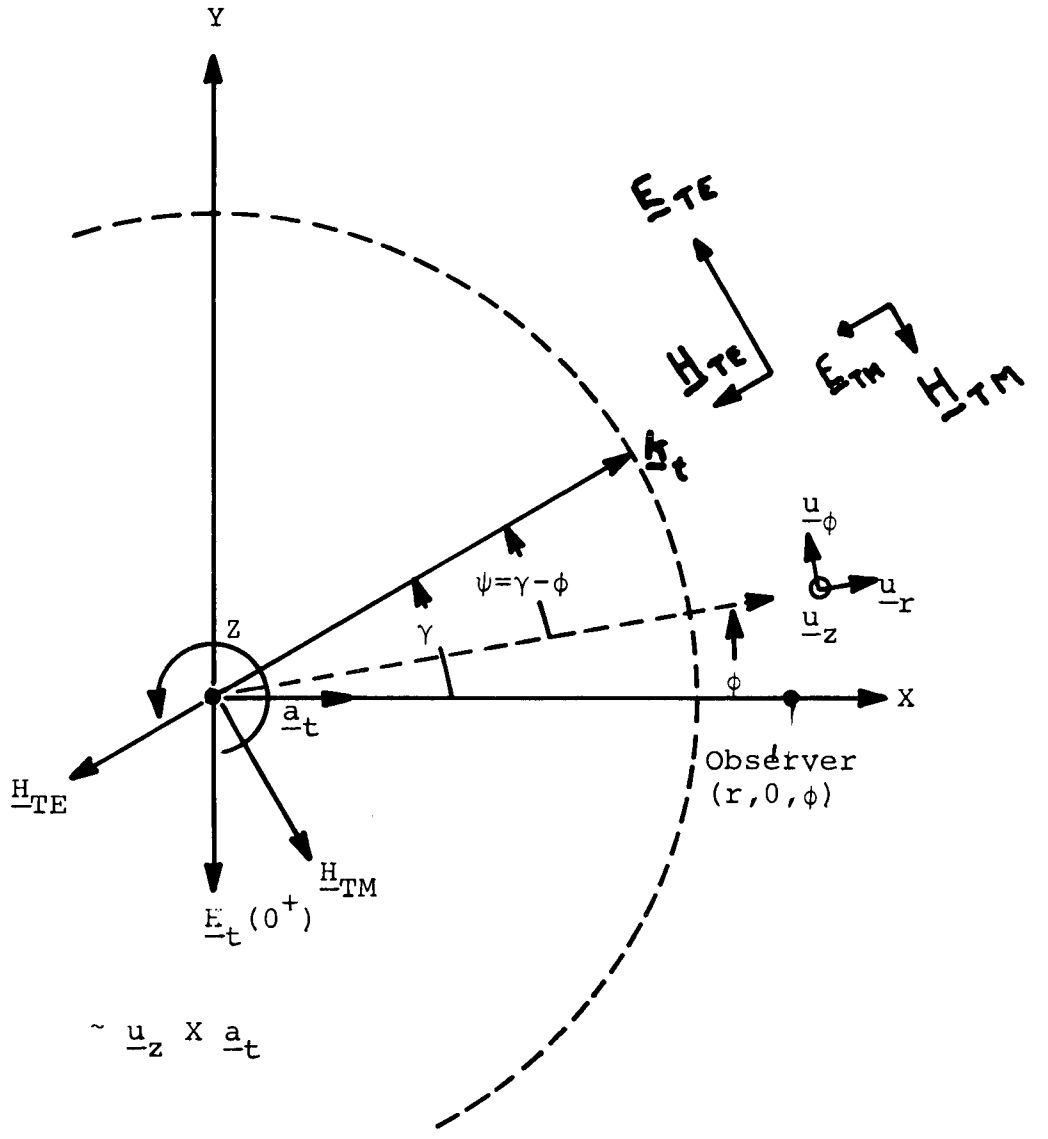

Figure 2-2 Angular Dependence of Wave Excitation

equation (2-49) becomes:

$$H_{1,z}(r) = \frac{1}{2\pi} \int_{K_t=0}^{\infty} K_t e^{-jk_1 z} J_1(K_t r) F(k_t) \, dK_t \qquad (2\text{-}49)$$

To obtain the far field solutions of equation (2-49), $F(k_t)$ is assumed to be constant or slowly varying with respect to the term $J_1(k_t r)\, e^{-jk_1 z}$ and a stationary phase approximation to the integral of equation (2-49) is obtained below.

An asymptotic form of the Bessel function $J_1(k_t r)$ for $k_t >> 1$ may be described by the equation:

$$e^{-jk_1 z} J_1(K_t r) \simeq \sqrt{\frac{2}{\pi K_t r}} \cos\left(K_t r - \frac{3\pi}{4}\right) e^{-jk_1 z} \qquad (2\text{-}50)$$

$$\simeq \sqrt{\frac{2}{\pi K_t r}} \, Re\left\{ e^{-j\left(K_t r - \frac{3\pi}{4}\right)} \right\} e^{-jk_1 z} \qquad (2\text{-}51)$$

With this asymptotic form of the Bessel Function, the phase terms of equation (2-51) are expanded in a series centered at the maximum value of the phase terms. The phase terms Φ are described by the equation:

$$\Phi \simeq -\left(K_t r + k_1 z\right) \qquad (2\text{-}52)$$

The maximum value of the phase terms is obtained by taking the first and second derivatives of the phase terms as illustrated below.

$$\frac{d\Phi}{dk_t} = -r + \frac{k_t}{k_1} z = 0 \tag{2-53}$$

$$\frac{k_t}{k_1} = \frac{r}{z} \tag{2-54}$$

$$\frac{d^2\Phi}{dk_t^2} = z\left(\frac{1}{k_1} + \frac{k_t^2}{k_1^3}\right) = \frac{R^3}{k_{c_1} z^2} \tag{2-55}$$

where $R = \sqrt{r^2 + z^2}$ (2-56)

and the values of $k_t/k_1 = r/z$ are substituted in the second derivative of Φ. The phase terms Φ are expanded about the point $(k_t - k_{to})$ with the resulting equation:

$$\Phi(k_t) = \Phi(k_{t_o}) + \frac{1}{2}\Phi''(k_{t_o})(k_t - k_{t_o})^2 + \cdots \tag{2-57}$$

where k_{t_o} is the value for k_t when Φ is a maximum. By substituting this stationary phase approximation in equation (2-49), the far field solution for $H_{1,z}$ is formulated as:

$$H_{1,z}(r) \cong e^{-jk_{c_1}R} \frac{F(k_{t_o})}{2} \frac{1}{2\pi} \int_{k_t=0}^{\infty} dk_t \, k_t \sqrt{\frac{2}{\pi k_t r}} e^{j\frac{3\pi}{4}} e^{j\frac{R^3(k_t - k_{t_o})}{2k_{c_1}z^2}} \tag{2-58}$$

Letting

$$k_t - k_{t_o} = \delta k_t \tag{2-59}$$

equation (2-58) can be written in the form:

$$H_{1,z}(r) \cong e^{-jk_{c_1}R} F(k_{t_o}) \frac{1}{2\pi} \int_{\delta k_t=-\infty}^{\infty} d(\delta k_t) \, k_t \left(\frac{1}{2}\right) \sqrt{\frac{2}{\pi k_t r}} e^{j\frac{3\pi}{4}} e^{j\frac{R^3(\delta k_t)^2}{2k_{c_1}z^2}} \tag{2-60}$$

Noting that the propagation constants are related by the equations:

$$k_1 = \sqrt{k_{c_1} - k_t^2} \tag{2-61}$$

$$\frac{r}{k_t} = \frac{R}{k_{c_1}} \tag{2-62}$$

the field component $H_{1,z}$ can be written in the form:

$$H_{1,z}(r) = e^{-jk_{c_1}R} F(k_{t_o}) \frac{1}{2\pi} \int_{\delta k_t=-\infty}^{\infty} d(\delta k_t) \left(k_{c_1}\frac{r}{R}\right)\left(\frac{1}{2}\right)^2 \cdot \left(e^{j\frac{3\pi}{4}}\right)\left(e^{j\frac{R^3(\delta k_t)^2}{2k_{c_1}z^2}}\right) \tag{2-63}$$

For $K^2 = \dfrac{R^3(\delta k_t)^2}{2 k_{c_1} z^2}$ (2-64)

and $dK = d(\delta k_t)\, \dfrac{R}{2} \sqrt{\dfrac{R}{2 k_{c_1}}}$ (2-65)

The Fresnel integral formulas listed below can be applied to equation (2-63),

$$\int_{-\infty}^{\infty} \cos K^2 dK = \int_{-\infty}^{\infty} \sin K^2 dK = \sqrt{\frac{\pi}{2}} \tag{2-66}$$

and equation (2-63) then can be written in the form:

$$H_{1,z}(\pi) = F(k_{t_0}) e^{-j k_{c_1} R} \frac{1}{2\pi} \int_{-\infty}^{\infty} dK \left[\frac{z}{R} \sqrt{\frac{2k_{c_1}}{R}} \left(\frac{1}{2}\right)^2 \cdot \left(e^{j\frac{3\pi}{4}}\right)\left(e^{jK^2}\right)\left(\sqrt{\frac{2R}{\pi k_{c_1} \pi^2}}\right)\left(k_{c_1} \frac{\pi}{R}\right)\right] \tag{2-67}$$

$$= F(k_{t_0}) e^{-j k_{c_1} R} \frac{1}{2\pi} \int_{-\infty}^{\infty} dK \left[\frac{z}{R} \left(\frac{1}{2}\right)\left(\sqrt{\frac{1}{\pi}}\right)\left(e^{j\frac{3\pi}{4}}\right)\left(e^{jK^2}\right) k_{c_1}\right] \tag{2-68}$$

$$= F(k_{t_0}) e^{-j k_{c_1} R} \frac{1}{2\pi} \int_{-\infty}^{\infty} \left\{ -j \cos K^2 \right\} \left(\frac{k_{c_1} z}{R^2}\right)\left(\frac{1}{2}\right) \sqrt{\frac{2}{\pi}}\, dK \tag{2-69}$$

Applying the Fresnel integral formulation (2-64) to equation (2-69) yields the equation:

$$H_{1,z} \cong F(k_{t_o})\left(\frac{-j}{4\pi}\right)\left(\frac{k_{c_1} z}{R^2}\right) e^{-jk_{c_1}R} \tag{2-70}$$

and substituting for $F(k_{t_o})$ from equation (2-48), $H_{1,z}$ can be written in the form:

$$H_{1,z}(R) \cong 2a_t \sin\phi \frac{k_{c_1} z}{R} \frac{e^{-jk_{c_1}R}}{4\pi R}\left\{\frac{\mu_{-1} k_t}{\mu_{-1} k_1 + \mu_1 k_{-1}}\right\} \tag{2-71}$$

For non-magnetic materials, the permeability of each medium is equal to that of free space such that:

$$\mu_{-1} = \mu_1 = \mu_0 \tag{2-72}$$

and now $H_{1,z}$ can be written in the form:

$$H_{1,z}(R) \cong 2a_t \sin\phi \left(\frac{k_{c_1} z}{R}\right)\left(\frac{e^{-jk_{c_1}R}}{4\pi R}\right)\left(\frac{k_t}{k_1 + k_{-1}}\right) \tag{2-73}$$

Far from the source and the z = 0 boundary $H_{1,z}$ is inversely proportional to the range R.

$$H_{1,z}(R) \longrightarrow 2a_t \sin\phi \frac{k_{c_1} k_t}{k_1 + k_{-1}} \frac{e^{-jk_{c_1}R}}{4\pi R} \tag{2-74}$$

$z \to \infty$
$R \to \infty$

2.3 A Surface Field Solution

To determine the surface magnetic field, the following Green's function identity, from Cooper,[2] is used:

$$\frac{1}{2\pi}\int_{K_t=0}^{\infty} dK_t\, K_t e^{-jK_i z} J_0(K_t r) = 2\frac{\partial}{\partial z} G_i \tag{2-75}$$

where $$G_i = \frac{e^{-jK_{c_i} R}}{4\pi R} \tag{2-76}$$

Equation (2-47) is put into a form analogous to that of equation (2-75) and the magnetic field component at the surface (H_z^s) is formulated in terms of the Green's function G_i.

$$H_z^s = a_t \sin\phi \frac{1}{2\pi}\int_{K_t=0}^{\infty} K_t\left(\frac{H_{-1} K_t}{H_{-1}K_1 + H_1 K_{-1}}\right) J J_1(K_t r) e^{-jK_i z} dK_t \tag{2-77}$$

Using the Bessel function relationship:

$$\frac{\partial}{\partial r} J_0(K_t r) = -K_t J_1(K_t r) \tag{2-78}$$

and expanding the integrand of equation (2-77) about the singularities of the denominator:

$$\frac{M_{-1}}{M_{-1}K_1+M_1K_{-1}} = \frac{M_{-1}}{M_1K_{-1}}\left[1-\left(\frac{M_{-1}K_1}{M_1K_{-1}}\right)-\left(\frac{M_{-1}K_1}{M_1K_{-1}}\right)^2-\cdots\right]$$

$$+\frac{1}{K_1}\left[1-\left(\frac{M_1K_{-1}}{M_{-1}K_1}\right)-\left(\frac{M_1K_{-1}}{M_{-1}K_1}\right)^2-\cdots\right] \qquad (2\text{-}79)$$

Equation (2-77) for z = 0 can be written in the form:

$$H_z^s(r) = J a_t \sin\phi \left\{\frac{1}{2\pi}\int_{K_t=0}^{\infty} dK_t\, K_t \frac{M_{-1}}{M_1K_{-1}}\left[1-\frac{M_{-1}K_1}{M_1K_{-1}}-\cdots\right]\right.$$

$$\cdot\left(\frac{\partial}{\partial r}J_0(K_t r)\right)+\frac{1}{2\pi}\int_{K_t=0}^{\infty} dK_t \frac{K_t^2}{K_1}$$

$$\left.\cdot\left[1-\left(\frac{M_1K_{-1}}{M_{-1}K_1}\right)-\cdots\right]\frac{\partial}{\partial r}J_0(K_t r)\right\} \qquad (2\text{-}80)$$

With the following relationships and the Green's function identity listed in equation (2-75), H_z^s is put into the form of equation (2-83) below.

$$K_t \to K_{c_1}\ ;\ K_{-1} = \sqrt{K_{c_{-1}}^2 - K_t^2} \cong \sqrt{K_{c_{-1}}^2 - K_{c_1}^2} \triangleq \underline{K} \qquad (2\text{-}81)$$

$$k_t \to k_{c_{-1}} \; ; \; k_1 = \sqrt{k_{c_1}^2 - k_t^2} \cong \sqrt{k_{c_1}^2 - k_{c_{-1}}^2} = -j\,K \tag{2-82}$$

$$H_z^s(\pi) = 2\,a_t \sin\phi \left\{ \frac{M_{-1}}{M_1} \left[\frac{\partial^2}{\partial \pi \partial z} G_{+1} - \frac{M_{-1}}{M_1 K} \left(\frac{\partial^3}{\partial \pi \partial z^2} G_{+1} \right) - \cdots \right] \right.$$

$$\left. + \frac{1}{-jK} \left[\frac{\partial^2}{\partial \pi \partial z} G_{-1} - \frac{M_1}{M_{-1} - jK} \left(\frac{\partial 3}{\partial \pi \partial z^2} G_{-1} \right) - \cdots \right] \right\} \tag{2-83}$$

The applicable partial derivatives of the Green's function G_i are listed below:

$$\frac{\partial}{\partial z} G_i = \left(-j\, k_{c_i} \frac{z}{R} - \frac{z}{R^2} \right) G_i \tag{2-84}$$

$$\frac{\partial}{\partial \pi} G_i = \left(-j\, k_{c_1} \frac{\pi}{R} - \frac{\pi}{R^2} \right) G_i \tag{2-85}$$

$$\frac{\partial}{\partial \pi} \left(\frac{\partial^2}{\partial z^2} G_i \right) = \frac{\partial}{\partial \pi} \left(-j \frac{k_{c_i}}{R} - \frac{1}{R^2} - \frac{k_{c_i} z^2}{R} \right. \tag{2-86}$$

$$\left. + \frac{3\,k_{c_i} z^2}{R^3} + \frac{3\,z^2}{R^4} \right) G_i$$

Neglecting terms containing z in the numerator, equation (2-86) becomes:

$$\left(\frac{\partial}{\partial r}\right)\left(\frac{\partial^2}{\partial z^2}\right)G_i = -j\frac{k_{c_i}}{R}\left(-j\frac{k_{c_i}r}{R} - \frac{r}{R^2}\right)G_i$$

$$+ j\frac{k_{c_i}r}{R^3}G_i - \frac{1}{R^2}\left(-j\frac{k_{c_i}r}{R} - \frac{r}{R^2}\right)G_i + \frac{2r}{R^4}G_i \qquad (2\text{-}87)$$

Noting that r = R at z = 0 and neglecting terms in equation (2-87) of higher order than $1/R^2$, equation (2-87) is approximated as:

$$\left(\frac{\partial}{\partial r}\right)\left(\frac{\partial^2}{\partial z^2}\right)G_i \cong -\frac{k_{c_i}^2}{R}G_i \qquad (2\text{-}88)$$

Substituting equation (2-88) into equation (2-83), yields the following asymptotic solution for H_z^s:

$$H_z^s(R) \cong 2a_t \sin\phi \left\{\frac{M_{-1}^2}{M_1 K^2}\frac{k_{c_1}}{R}G_1 - \frac{M_1}{M_1 K^2}\frac{k_{c_{-1}}^2}{R}G_i\right\} \qquad (2\text{-}89)$$

which can be written in the alternate form:

$$H_z^s(R) \cong 2a_t \sin\phi \frac{M_{-1}^2 k_{c_1}^2}{M_1^2 K^2 R}\left[G_1 - \left(\frac{M_1}{M_{-1}}\right)\left(\frac{k_{c_{-1}}}{k_{c_1}}\right)^2 G_{-1}\right] \qquad (2\text{-}90)$$

Noting that all terms in the expansion contribute fields proportional $1/R^M$, only the terms proportional to k_{-1} and k_1 in the series expansion described by equation (2-80) are integrated in equation (2-83), since these terms contribute the lowest order fields to the integral.

The remaining $\underline{E}$ and $\underline{H}$ surface fields can be obtained in an analogous manner. These field solutions are tabulated by Cooper,[2] and, therefore, are not repeated here.

Since the far field component H_z in equation (2-74) is proportional to 1/R and the asymptotic surface field H_z^s is proportional to $1/R^2$ as illustrated in equation (2-90), an initial conclusion is that there is no radiation (1/R dependence) along the surface. This conclusion is verified by the calculation of the radiation pattern for an infinitesimal HED in the following section of this chapter.

2.4 Radiation Patterns of an Infinitesimal HED over a Half-Space

An example illustrating the approach used to determine the far field solutions of the electromagnetic fields of an infinitesimal HED is described in section 2.1 of this chapter. These far field solutions are used to determine the power radiated in the TE and TM fields. The field components $E\phi$ for TE radiation and $H\phi$ for TM radiation are sufficient to define the Poynting vector. $E\phi$ is directly related to the $H\rho$ and H_z components and $H\phi$ is directly related to the E_z and $E\rho$ components through transverse impedances (equation (2-24)). Cooper[2] has shown that the far fields $E\phi$ and $H\phi$ can be

approximated as:

$$\begin{Bmatrix} E_\phi(R) \\ H_\phi(R) \end{Bmatrix} = \frac{j2K_{c_i}z}{R} \frac{e^{-jK_{c_i}R}}{4\pi R} \begin{Bmatrix} E_\phi', TE \\ H_\phi', TM \end{Bmatrix} \tag{2-91}$$

where for z > 0

$$E_\phi' = a_t \sin\phi \frac{\omega M_1 M_{-1}}{M_{-1}K_1 + M_1 K_{-1}} \tag{2-92}$$

and

$$H_\phi' = -a_t \cos\phi \frac{\epsilon_1 K_{-1}}{\epsilon_{-1}K_1 + \epsilon_1 K_{-1}} \tag{2-93}$$

and for z < 0

$$E_\phi' = -a_t \sin\phi \frac{\omega M_1 M_{-1}}{M_{-1}K_1 + M_1 K_{-1}} \tag{2-94}$$

and

$$H_\phi' = -a_t \cos\phi \frac{\epsilon_{-1} K_1}{\epsilon_{-1}K_1 + \epsilon_1 K_{-1}} \tag{2-95}$$

Using Poynting's theorem, Cooper has determined that the power radiated per unit of solid angle is proportional to:

$$\frac{dP}{d\Omega_i}(\theta,\phi) \propto \sqrt{\frac{\mu_i}{\epsilon_i}}\left|\frac{k_i}{k_{c_i}} H'_{\phi,TM}\right|^2 + \sqrt{\frac{\epsilon_i}{\mu_i}}\left|\frac{k_i}{k_{c_i}} E'_{\phi,TE}\right|^2 \tag{2-96}$$

where E'_ϕ and H'_ϕ are described by equations (2-92) - (2-95) and θ is defined in terms of k_i, and k_{ci}. Graphs of the radiation patterns for an infinitesimal HED over glacial ice with a dielectric constant of 3.2 are shown in Figures (2-3) and (2-4). The electrical parameters of air, the upper medium, by the equations:

$$\mu_1 = \mu_{-1} = \mu_0 \tag{2-97}$$

$$\frac{\epsilon_{-1}}{\epsilon_1} = \frac{\epsilon_{-1}}{\epsilon_0} = 3.2 \tag{2-98}$$

To determine the gain of the infinitesimal HED relative to an isotropic source, the power per unit of solid angle, $dP/d\Omega_i$, is first integrated over all solid angles using the equation:

$$P_i = \int_0^{2\pi} d\phi \int_{k_t/k_{c_i}=0}^{1} \frac{dk_t}{k_{c_i}} \frac{k_t}{k_{c_i}} \frac{k_{c_i}}{k_i} \frac{dP}{d\Omega_i}(\theta,\phi) \tag{2-99}$$

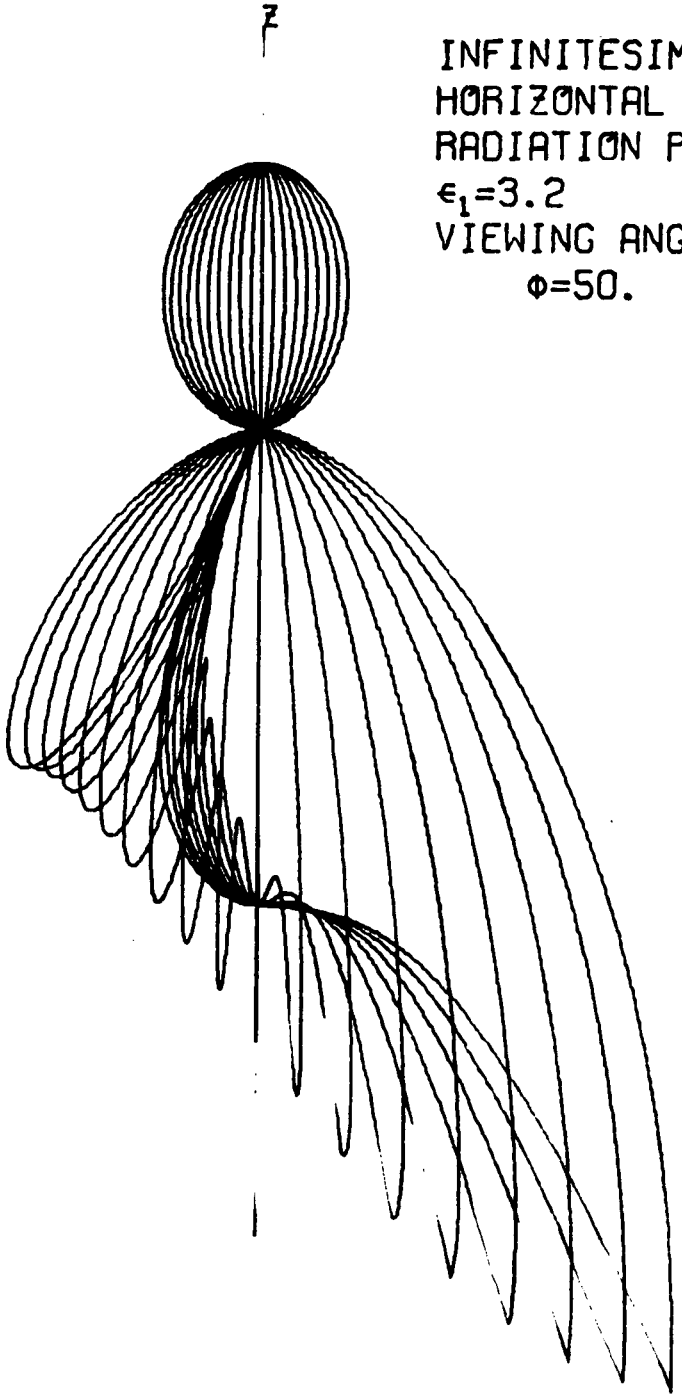
z
INFINITESIMAL
HORIZONTAL ELECTRIC DIPOLE
RADIATION PATTERN
ϵ_1=3.2
VIEWING ANGLE
Φ=50.
Θ=0.

Figure 2-3

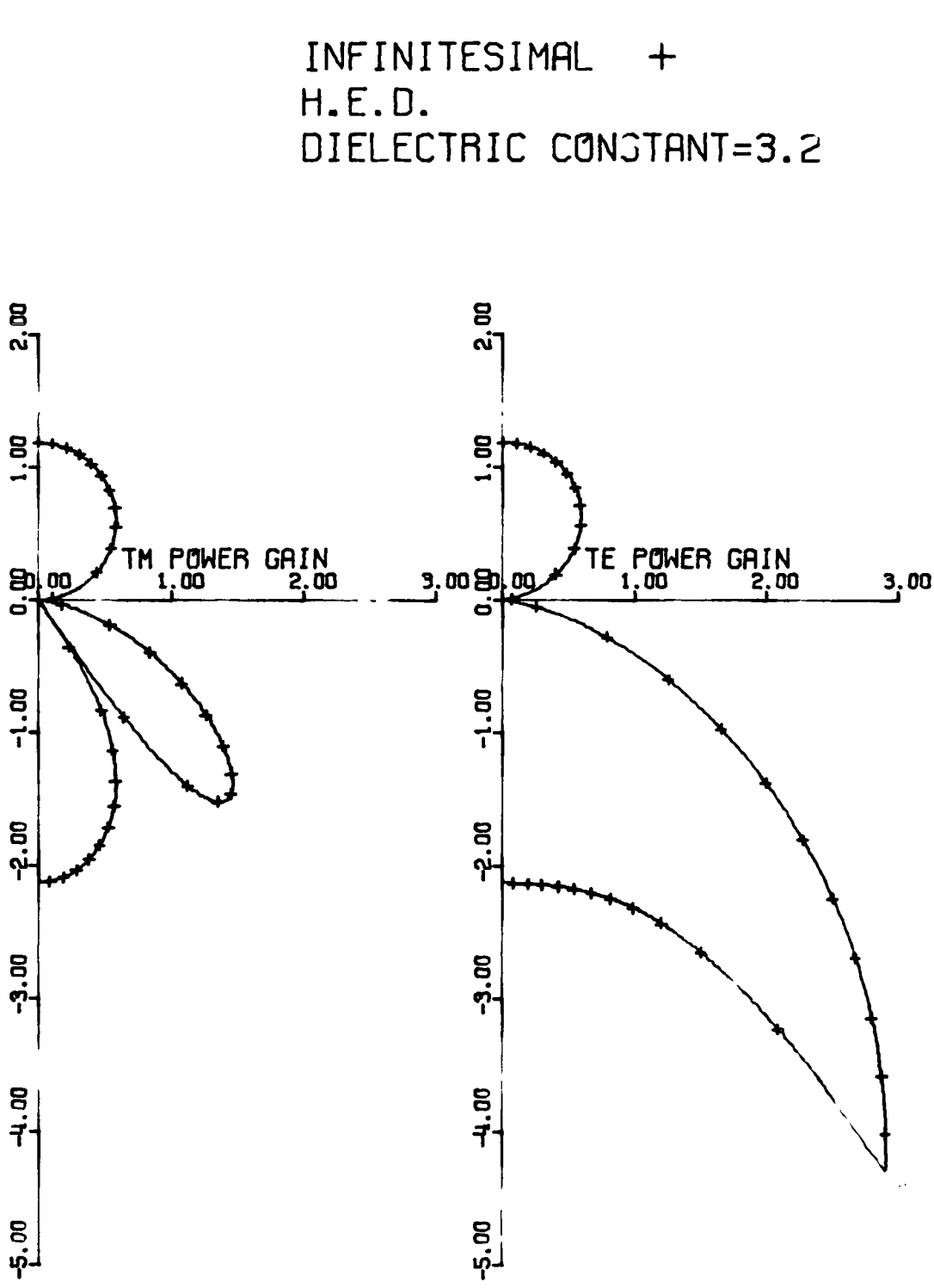
INFINITESIMAL +
H.E.D.
DIELECTRIC CONSTANT=3.2
TM POWER GAIN
TE POWER GAIN
2.00
1.00
0.00
-1.00
-2.00
-3.00
-4.00
-5.00
0.00
1.00
2.00
3.00

Figure 2-4

which becomes:

$$P_i = \pi \int_{k_t/k_{c_i}}^{1} \frac{dk_t}{k_{c_i}} \frac{k_t}{k_{c_i}} \frac{k_{c_i}}{k_i} \frac{dP}{d\Omega}(\theta) \qquad (2\text{-}100)$$

$$i = \pm 1 \qquad (2\text{-}101)$$

The gain relative to an isotropic source is described by the equation:

$$G = \frac{\frac{dP}{d\Omega_i}(\theta, \phi)}{\frac{1}{4\pi} \sum_{i=\pm 1} P_i} \qquad (2\text{-}102)$$

2.5 Waves Reflected from Subsurface Layers

The surface field solutions for an infinitesimal HED over a half-space have been described in section 2.3 When the lower medium consists of horizontally stratified, electrically contrasting layers, reflections from these layers must be considered to determine the surface fields. To illustrate the contribution of reflected fields to the surface fields, the reflected vertical magnetic component of the surface fields $H^s_{z,R}$ is presented here using the three-layer geometry illustrated in Figure (2-5).

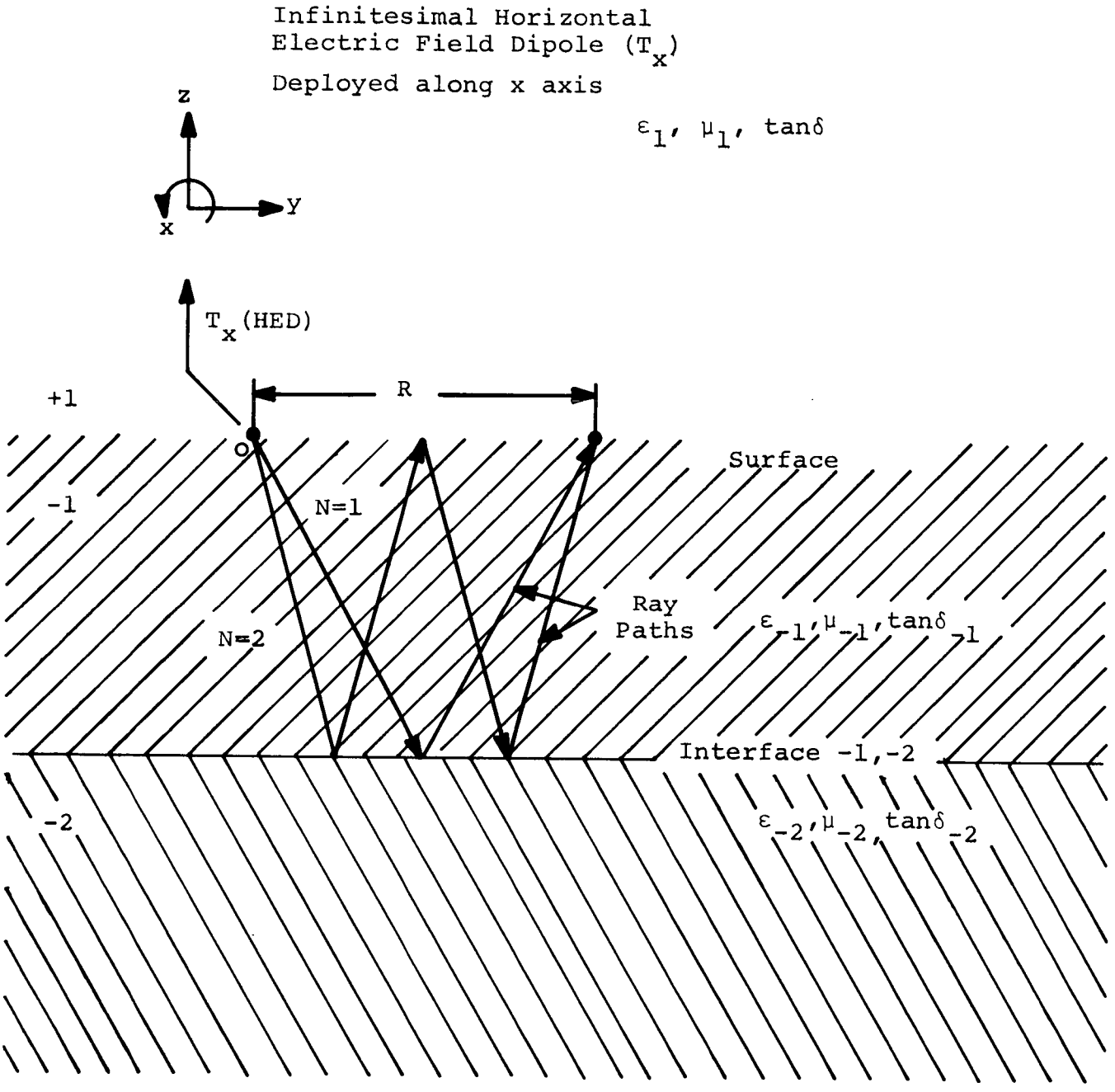

Figure 2-5 Three Layer Geometry

As illustrated in equation (2-49), the integral form of the half-space solutions of the vertical magnetic field $H_{i,z}$ is described by the equation:

$$H_{i,z}(r) = \frac{1}{2\pi} \int_{k_t=0}^{\infty} k_t e^{-jk_i z} J_1(k_t r) F(k_t) \, dk_t \tag{2-103}$$

Cooper[2] has shown that the term $F(k_t)$ can be expressed as a transformation matrix which contains the reflection and transmission coefficients of the subsurface layers. The fields in any layer are related to the excitation fields at the surface ($z = 0$) by this transformation matrix.

$$F_i(k_t) \triangleq F(k_t) \tag{2-104}$$

Since $F_i(k_t)$ is not a function of the angular variables γ and ϕ, the integration in equation (2-40), is valid when $F_i(k_t)$ is substituted for $F(k_t)$ in equation (2-49). Thus, equation (2-49) can be written as:

$$H_{i,z}(r) = \frac{1}{2\pi} \int_{k_t=0}^{\infty} dk_t \, k_t e^{-jk_i z} J_1(k_t) F_i(k_t) \tag{2-105}$$

By replacing $F_i(k_t)$ in equation (2-105) with the equivalent form:

$$e^{-jk_{i2}} F_i(k_t) = G_i(k_t)\, e^{-jk_{-1}(m\Delta)} \tag{2-106}$$

where n is the number of ray sections in the ray path (n = 2 for a single reflection), the stationary phase term Φ_n, as in equation (2-52), becomes:

$$\Phi_m \simeq -\left(k_t r + m k_{-1} \Delta\right) \; ; \; k_t r >> 1 \tag{2-107}$$

Differentiating Φ_n by k_t yields the equation:

$$\frac{d\Phi_m}{dk_t} = -r + \frac{k_t}{k_{-1}(m\Delta)} = 0 \tag{2-108}$$

and the second derivative is:

$$\frac{d^2\Phi_m}{dk_t^2} = m\Delta\left(\frac{1}{k_{-1}} + \frac{k_t}{k_{-1}^3}\right) = \frac{R_m}{k_{c_{-1}}(m\Delta)} \tag{2-109}$$

where

$$R_m = \sqrt{r^2 + (m\Delta)^2} \tag{2-110}$$

and Δ = the depth to the reflecting interface (2-111)

By performing the stationary phase approximation on equation (2-105) for a single reflection, the contribution of the reflected fields to the magnetic surface fields is described by the equation:

$$H_R^S(R) = -\underline{y}_z \times \underline{g}_t \left(\frac{-2\eta_1}{\eta_{-1}+\eta_{+1}}\right)\left(\frac{\eta_{-1}-\eta_{-2}}{\eta_{-1}+\eta_{-2}}\right)\left(\frac{\eta_{-1}}{\eta_{-1}+\eta_1}\right) \cdot \left(\frac{jk_{c_{-1}}(2\Delta)}{R_2}\right)\left(\frac{e^{-jk_{c_{-1}}R_2}}{4\pi R_2}\right) \tag{2-112}$$

for $k_t >> 1$ and $(k_{c_{-1}} - |k_{-1}|)\,\Delta >> 1$ (2-113)

$\frac{-2\eta_1}{\eta_{-1}+\eta_1}$ = the lower space excitation factor (2-114)

$\frac{\eta_{-1}-\eta_{-2}}{\eta_{-1}+\eta_{-2}}$ = the reflection factor for the surface at $z = -\Delta$ (2-115)

$\frac{\eta_1}{\eta_{-1}+\eta_1}$ = the transmission factor for the surface at $z = 0$ (2-116)

The vertical magnetic reflected field is $H^S_{z,R}$ obtained by applying equation (2-34) to equation (2-112) using the TE transverse impedance formulation in equation (2-24). The resulting equation for $H^S_{z,R}$ due to a single reflection is:

$$H^{S}_{z,R} \cong \left[2 a_t \sin\phi \left(j k_{c_{-1}} \frac{2\Delta}{R_2} \right) \left(\frac{e^{-j k_{c_{-1}} R_2}}{4\pi R_2} \right) \right]$$

$$\cdot \left[\frac{M_{-1} K_t}{M_{-1} K_1 + M_1 K_{-1}} \right] \cdot \left[-2 \frac{M_1 K_{-1}}{M_{-1} K_1 + M_1 K_{-1}} \right]$$

$$\cdot \left[\frac{M_{-1} K_{-2} - M_{-2} K_{-1}}{M_{-1} K_{-2} + M_{-2} K_{-1}} \right] \cdot \left[\frac{M_{-1} K_1}{M_{-1} K_1 + M_1 K_{-1}} \right] \qquad (2\text{-}117)$$

For non-magnetic materials $\mu_1 = \mu_{-1} = \mu_{-2} = \mu_0$ and equation (2-117) becomes:

$$H^{S}_{z,R} \cong \left(-j 4 a_t \sin\phi \right) K_{c_{-1}} \left(\frac{2\Delta}{R_2} \right) \left(\frac{e^{-j k_{c_{-1}} R_2}}{4\pi R_2} \right)$$

$$\cdot \left(\frac{K_t}{K_1 + K_{-1}} \right) \left(\frac{K_{-1}}{K_1 + K_{-1}} \right) \left(\frac{K_{-2} - K_{-1}}{K_{-2} + K_{-1}} \right) \qquad (2\text{-}118)$$

From the stationary phase equations (2-54) and (2-61), the vertical propagation constant k_{-1} can be written as:

$$K_{-1} = K_{c_{-1}} \frac{2\Delta}{R_2} \qquad (2\text{-}119)$$

and equation (2-118) becomes:

$$H^{S}_{z,R} = -\frac{J}{\pi} a_t \sin\phi \left(\frac{K_{-1} K_t}{R_2}\right)\left(\frac{1}{K_1 + K_{-1}}\right)\left(\frac{K_{-1}}{K_1 + K_{-1}}\right) \cdot \left(\frac{K_{-2} - K_{-1}}{K_{-2} + K_{-1}}\right) e^{-jK_{-1}R_2} \qquad (2\text{-}120)$$

The complete solution for the H_z surface fields includes the half-space terms presented in section 2-2 and the reflected terms such that:

$$H^{S}_{z,0} = H^{S}_{z,(+1)} + H^{S}_{z,(-1)} + H^{S}_{z,R} \qquad (2\text{-}121)$$

where the components of the above equation are listed in sections 2.2 and 2.4.

CHAPTER THREE

Field Solutions for a Half Wavelength, HED Antenna

3.0 Introduction

This chapter contains the electromagnetic field solutions and radiation patterns for a harmonically excited, finite length, (half wave) HED deployed at the interface between two dielectric media (See Figure 3-1). The approach used for the determination of these field solutions and radiation patterns is as follows: first, the distribution of current in a half wavelength HED antenna is determined theoretically and verified experimentally; second, the antenna is assumed to be composed of an array of infinitesimal HED's where the excitation amplitudes and phases of these infinitesimal dipoles are defined by the antenna current distribution. Third, by integrating over the antenna length the contributions to the electromagnetic field from each infinitesimal HED, the field solutions and radiation patterns are obtained. The results obtained in this chapter and related appendices include:

1. The measured amplitude of the current distribution of a near half wavelength HED antenna deviates from a cosinusoidal distribution by less than 10%.
2. The half wavelength HED antenna TE surface fields far from the antenna are shown to vary azimuthally as $\sin \phi \cdot M_i^{\xi}(\frac{\pi}{2}, \phi)$.

HALF WAVELENGTH HORIZONTAL DIPOLE
AT FREE SPACE-DIELECTRIC INTERFACE

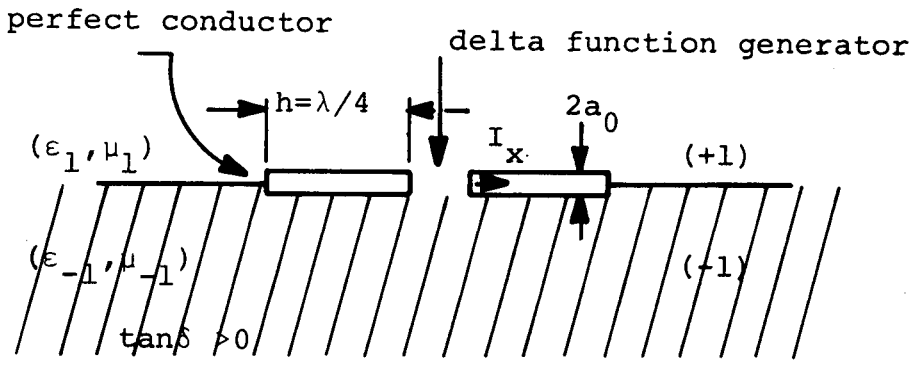

Figure 3-1

and the TM surface fields as $\cos\phi \cdot M_1^{\xi}(\frac{\pi}{2},\phi)$.

3. Near the half wavelength HED transmitting antenna, the horizontal TE and TM surface fields, H_{ρ}^{s} and H_{ϕ}^{s} respectively, are shown to be dependent and geometrically coupled.
4. The radiation patterns of the half wavelength HED and the infinitesimal HED are shown to be similar, with the exception of the gain of the lower space, TM, off-vertical lobe, which is smaller in the half wavelength TM radiation pattern by a factor of 0.75 for $\varepsilon_{-1}/\varepsilon_1 = 3.2$.
5. For a half wavelength HED antenna over a stratified medium having a thin upper layer over a thick electrically contrasting layer, the radiation pattern of the antenna is effectively that for a half wavelength antenna over the thick layer.

3.1 Current Distribution Calculation

The current distribution for a half wave HED deployed at the interface between two dielectric media is obtained by combining King's[5] formulation of the current distribution in a dissipative medium with Tsao's[6] formulation of the impedance of a half wave dipole deployed at the interface between two dielectrics.

The directly useful results of King's research are equations and graphs of the current distribution of a half wave dipole immersed in a dissipative medium. A slight

adaptation of these results is made for a half wave dipole at the interface between two dielectrics. The impedance of half wave dipoles at the interface of two dielectrics has been studied for the SEP experiment by Dr. J. de Bettencourt and C.Tsao, of Raytheon Corporation.

C. Tsao[6] indicates that an antenna situated at the interface between two media can be assumed for the purposes of impedance calculations to be immersed in a medium of dielectric constant equal to the average dielectric constant of the two dielectrics.

$$K_{\varepsilon_{eff}} = \frac{K_{\varepsilon_1} + K_{\varepsilon_{-1}}}{2} \qquad (3\text{-}1)$$

where $K_{\varepsilon_{+1}}$ = dielectric const. of medium +1 (3-2)

$K_{\varepsilon_{-1}}$ = dielectric const. of medium -1 (3-3)

A formulation of the current distribution of a half wave dipole at the interface between two dielectric media is determined by substituting the effective dielectric constant ($K_{\varepsilon_{eff}}$) for the medium dielectric constant (ε_r) in King's current distribution equations. The validity of this assumption has been corroborated by current distribution and dielectric constant measurements conducted on the Athabasca Glacier in the summer of 1971. These measurements are described in Chapter Five.

Throughout the text the finite length HED antennas are considered as half wavelengths from tip to tip in a medium whose phase velocity (V) is described by the equation:

$$V = \frac{1}{\sqrt{(\epsilon_{eff})_r \mu_0}} = \frac{C_0}{\sqrt{K_{\epsilon_{eff}}}} \tag{3-4}$$

and the effective wavelength is represented by the equation:

$$\lambda_{eff} = \frac{C_0}{f\sqrt{K_{\epsilon_{eff}}}} = \frac{\lambda_0}{\sqrt{K_{\epsilon_{eff}}}} \tag{3-5}$$

The current distribution and the phase relationship between the excitation voltage and current of half wavelength HED's in dissipative media are illustrated in Figure (3-2) and (3-3). In these figures, the current distribution is shown to vary approximately ten degrees for loss tangents (tan δ) of the order of 0.03. As indicated in Appendix A-2, the current distribution formulation[5] for a half wavelength HED antenna can be put in the form:

$$\frac{I_x}{V_0\sqrt{K_{\epsilon_{eff}}}} = a\cos K_{eff}x + b(\sin K_{eff}|x| - 1) \tag{3-6}$$

$$+ jc\cos K_{eff}x + jd(\sin K_{eff}|x| - 1)$$

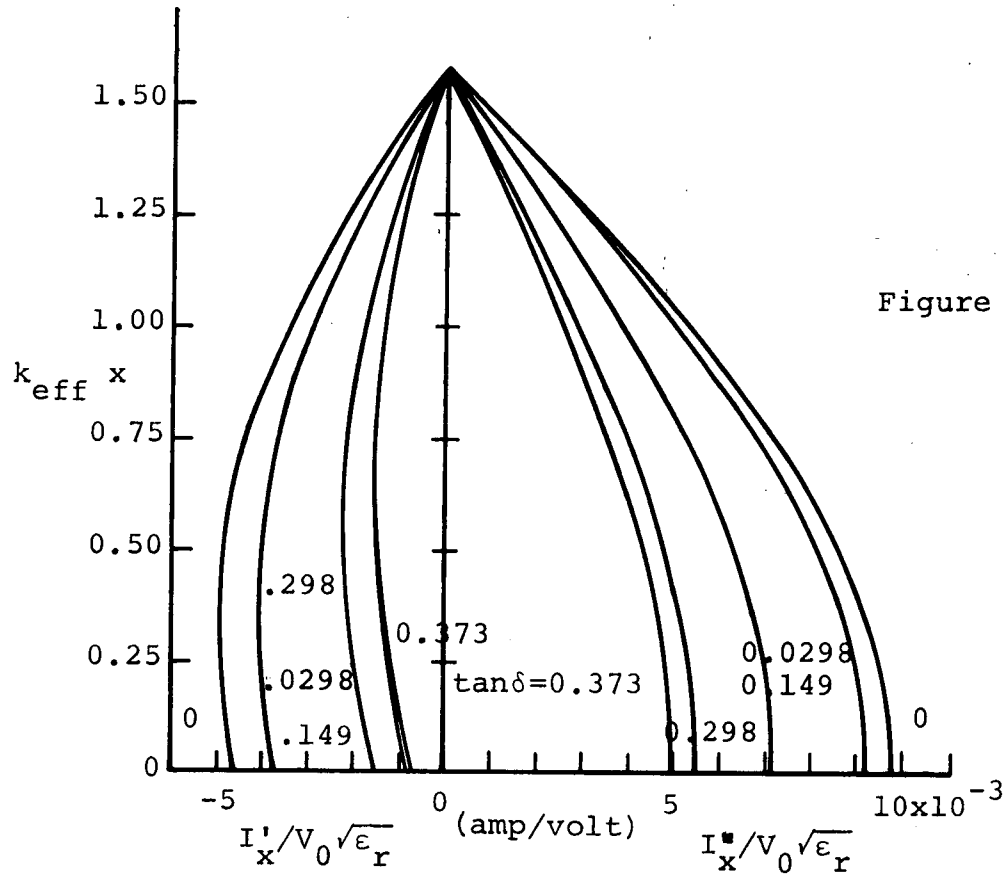

Figure 3-2

Current, $I_x = I_x + jI_x'$ in normalized form for a half wavelength dipole in a medium with dielectric constant (ε_r) and loss tangent (tanδ). I_x'' is in phase with the driving voltage V_0. (FROM R.W.P. KING)

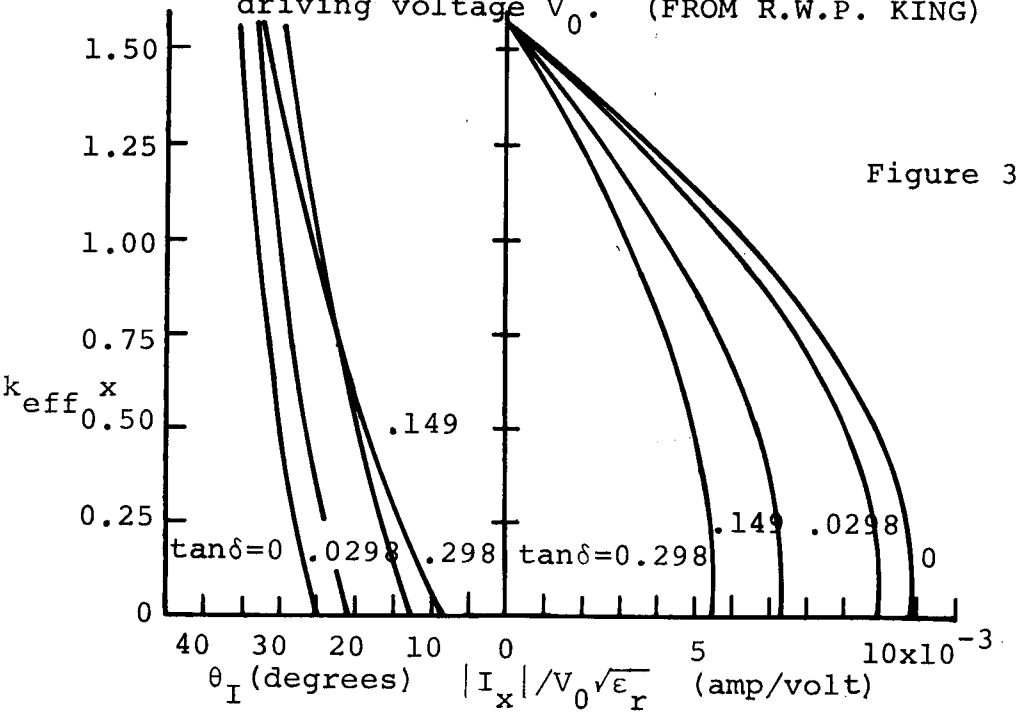

Figure 3-3

Current in Figure 3-2 in the form $|I_x|e^{j\theta}i$
(FROM R.W.P. KING)

where $K_{eff} = \left(\frac{2\pi}{\lambda_0}\right)\sqrt{K_{\epsilon_{eff}}}$ (3-7)

Another useful form of equation (3-6) is:

$$\frac{I_x}{V_0\sqrt{K_{\epsilon_{eff}}}} = I_1 e^{j\psi_1} \cos K_{eff} x + I_2 e^{j\psi_2}(\sin K_{eff}|x| - 1)$$

where $I_1 = \sqrt{a^2 + c^2}$ (3-8)

$I_2 = \sqrt{b^2 + d^2}$ (3-9)

$\psi_1 = \arctan \frac{c}{a}$ (3-10)

$\psi_2 = \arctan \frac{d}{b}$ (3-11)

Since near half wavelength HED antennas have been tested on a large scale dielectric, the Athabasca glacier, the current distribution parameters which represent the dielectric properties of the lower medium are specialized to those of ice. These parameters are represented by the equations:

$K_{\epsilon_{ice}} = 3.2$ (3-12)

$\tan\delta = 0.3/f$; f in MHz (3-13)

In addition, the antenna wire (#22 gauge) is assumed to be characterized by an infinite conductivity. The current distribution coefficients for half wavelength HED's at the SEP experiment frequencies (1,2,4,8,16 and 32 MHz) are listed in Table 3-1.

Current Distribution Coefficients

TABLE 3-1

Frequency	a	b	c	d	I_1	ψ_1	I_2	ψ_2
MHz	$\frac{ma}{volt}$	$\frac{ma}{volt}$	$\frac{ma}{volt}$	$\frac{ma}{volt}$	$\frac{ma}{volt}$	deg	$\frac{ma}{volt}$	deg
1	2.16	-0.20	-1.57	-1.03	2.67	-36.0	-1.05	77.5
2	4.03	-0.09	-1.96	-1.12	4.45	-25.7	-1.12	82.9
4	6.22	-0.03	-2.89	-1.24	6.86	-25.1	-1.24	88.6
8	8.03	+0.006	-4.21	-1.38	9.1	-27.7	-1.38	90.4
16	9.09	+0.04	-5.40	-1.59	10.5	-30.7	-1.59	91.4
32	9.58	+0.06	-6.20	-1.79	11.4	-33.0	-1.79	91.9

3.2 Current Distribution Measurements

The current distribution of a near half wavelength resonant antenna deployed at the interface between two dielectrics (air/ice) was measured on the surface of the Athabasca Glacier in Alberta, Canada during the summer of 1971. A multi-frequency, resonant, HED antenna was designed by Raytheon Co. for the SEP experiment field trials. Resonant circuit "traps" and "suppressors" were used to limit electromagnetic radiation to that portion of the antenna corresponding to the half wavelength of each of the experiment frequencies.

The measured amplitudes of the current distributions for each SEP experiment frequency are illustrated in Figures 3-4 through 3-9. The distribution curves deviate from cosinusoidal curves by less than 5% if discontinuities in the curves are neglected. These discontinuous points in Figures 3-4 through 3-9 are attributable to the experimental inaccuracy involved in the measurement of current distribution near traps and suppressors and the sensitivity of the antenna impedance to surface irregularities. A more complete description of the current distribution measurement is included in Chapter 5. However, an important conclusion to be drawn from Section 3.2 is that the measurements of the current distribution are consistent with small values of the current distribution coefficients b and d in Section 3.1 with the result that variations in phase along the length of the antenna can be assumed to be small.

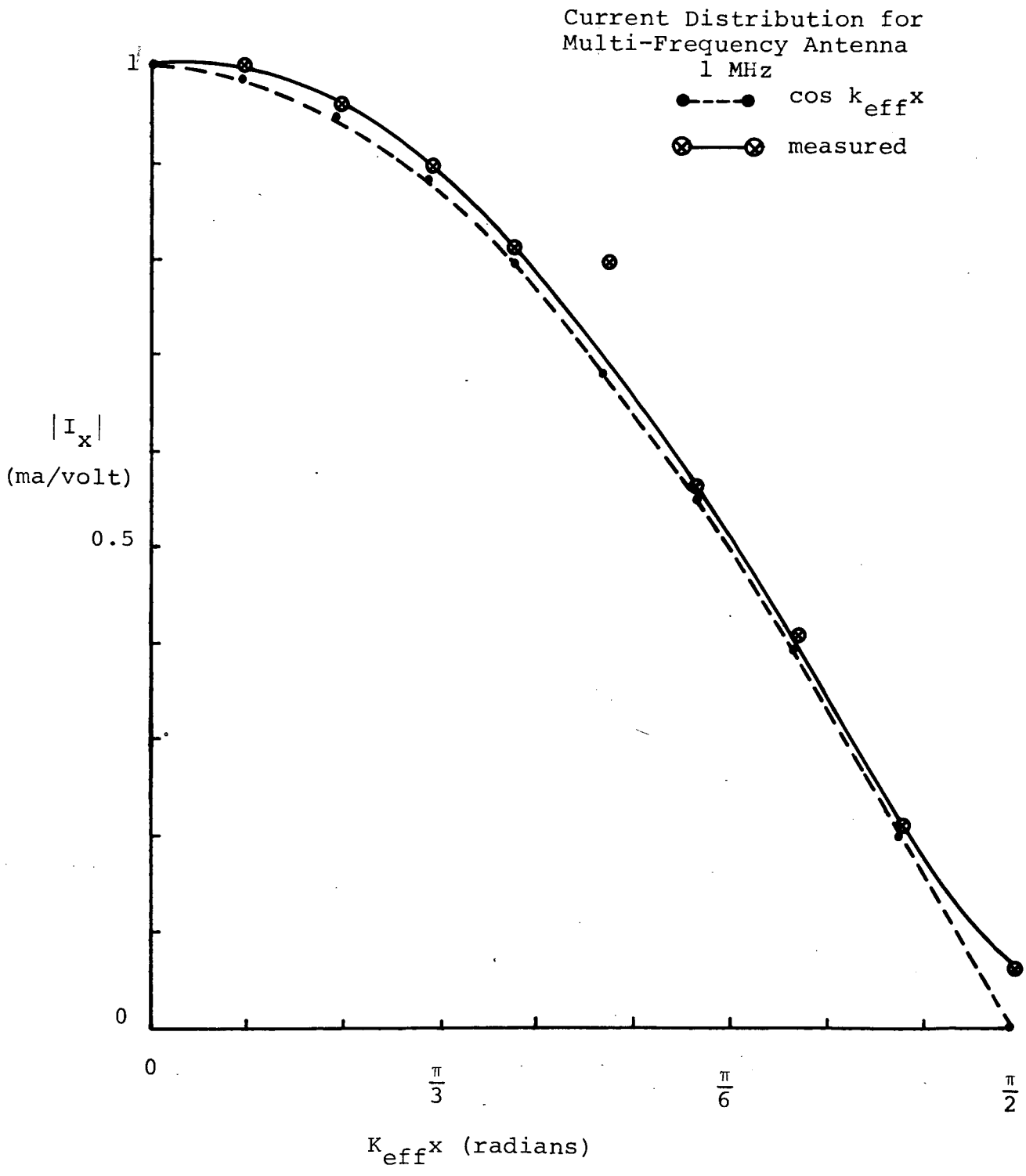
Current Distribution for
Multi-Frequency Antenna
1 MHz
cos $k_{eff}x$
measured
1
$|I_x|$
(ma/volt)
0.5
0
0
$\frac{\pi}{3}$
$\frac{\pi}{6}$
$\frac{\pi}{2}$
$K_{eff}x$ (radians)

Figure 3-4

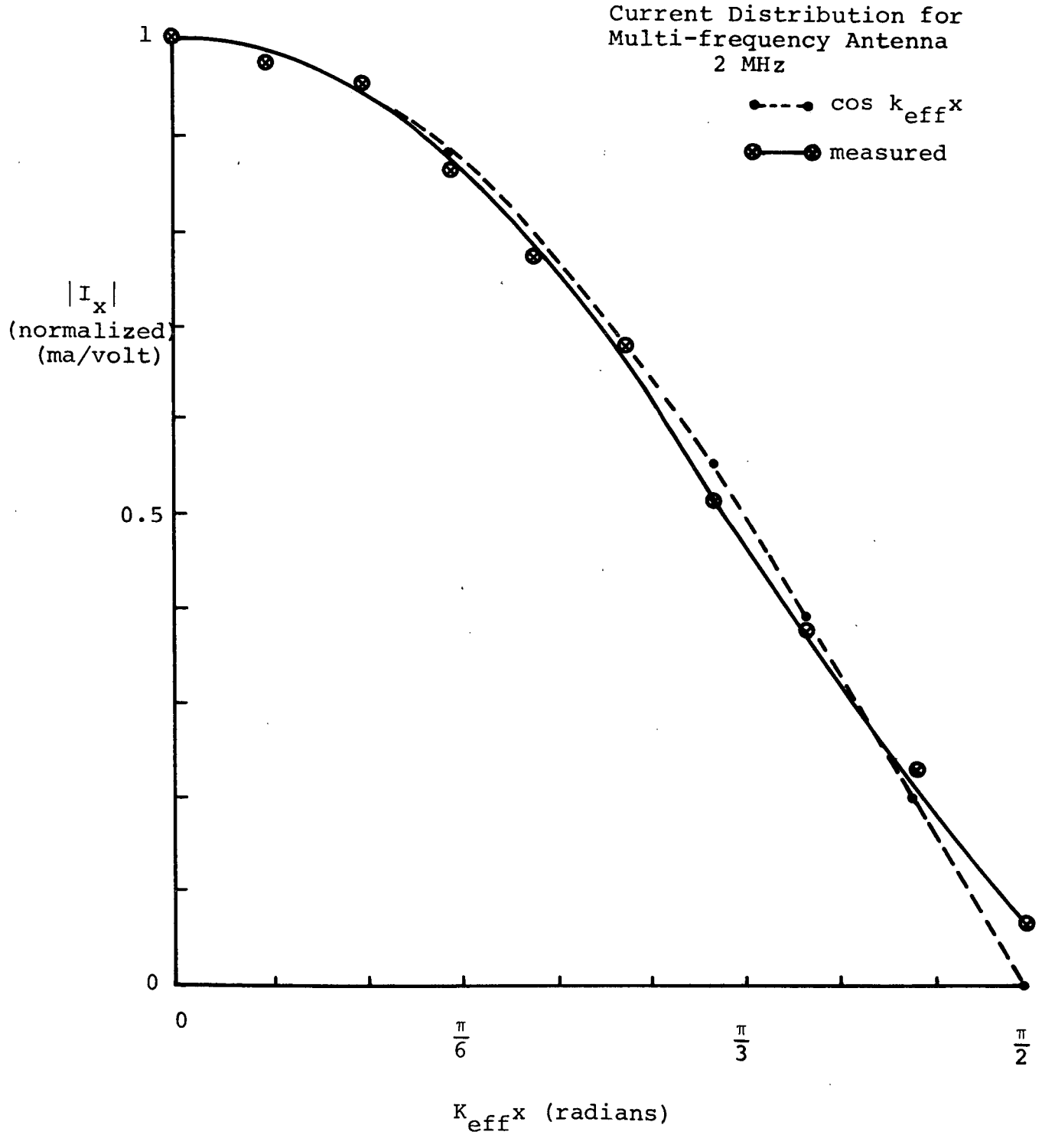
Current Distribution for
Multi-frequency Antenna
2 MHz
cos $k_{eff}x$
measured
1
0.5
0
$|I_x|$
(normalized)
(ma/volt)
0
$\frac{\pi}{6}$
$\frac{\pi}{3}$
$\frac{\pi}{2}$
$K_{eff}x$ (radians)

Figure 3-5

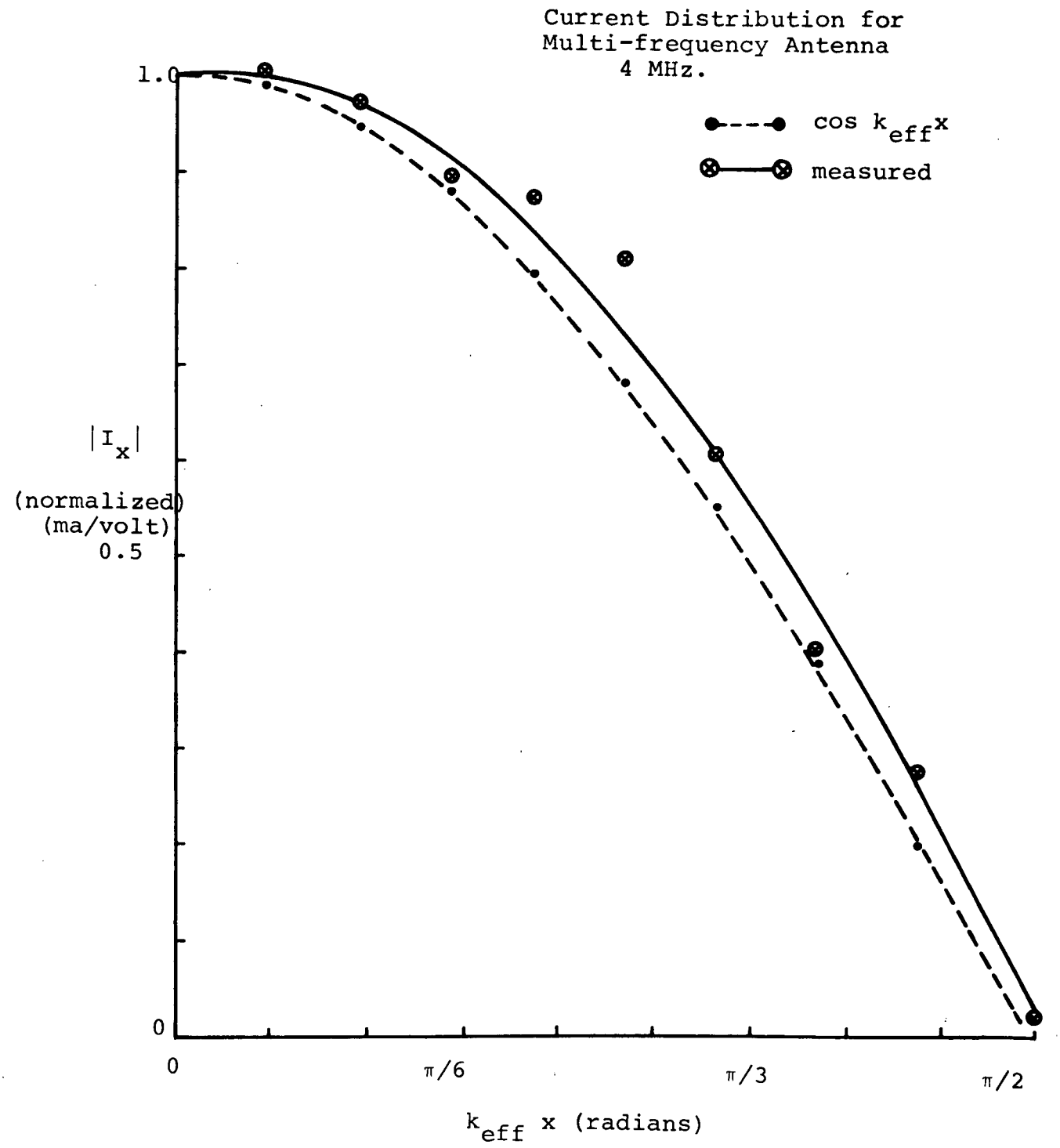
Current Distribution for
Multi-frequency Antenna
4 MHz.
cos $k_{eff}x$
measured
1.0
$|I_x|$
(normalized)
(ma/volt)
0.5
0
0
π/6
π/3
π/2
k_{eff} x (radians)

Figure 3-6

Current Distribution for
Multi-Frequency Antenna

8 MHz.

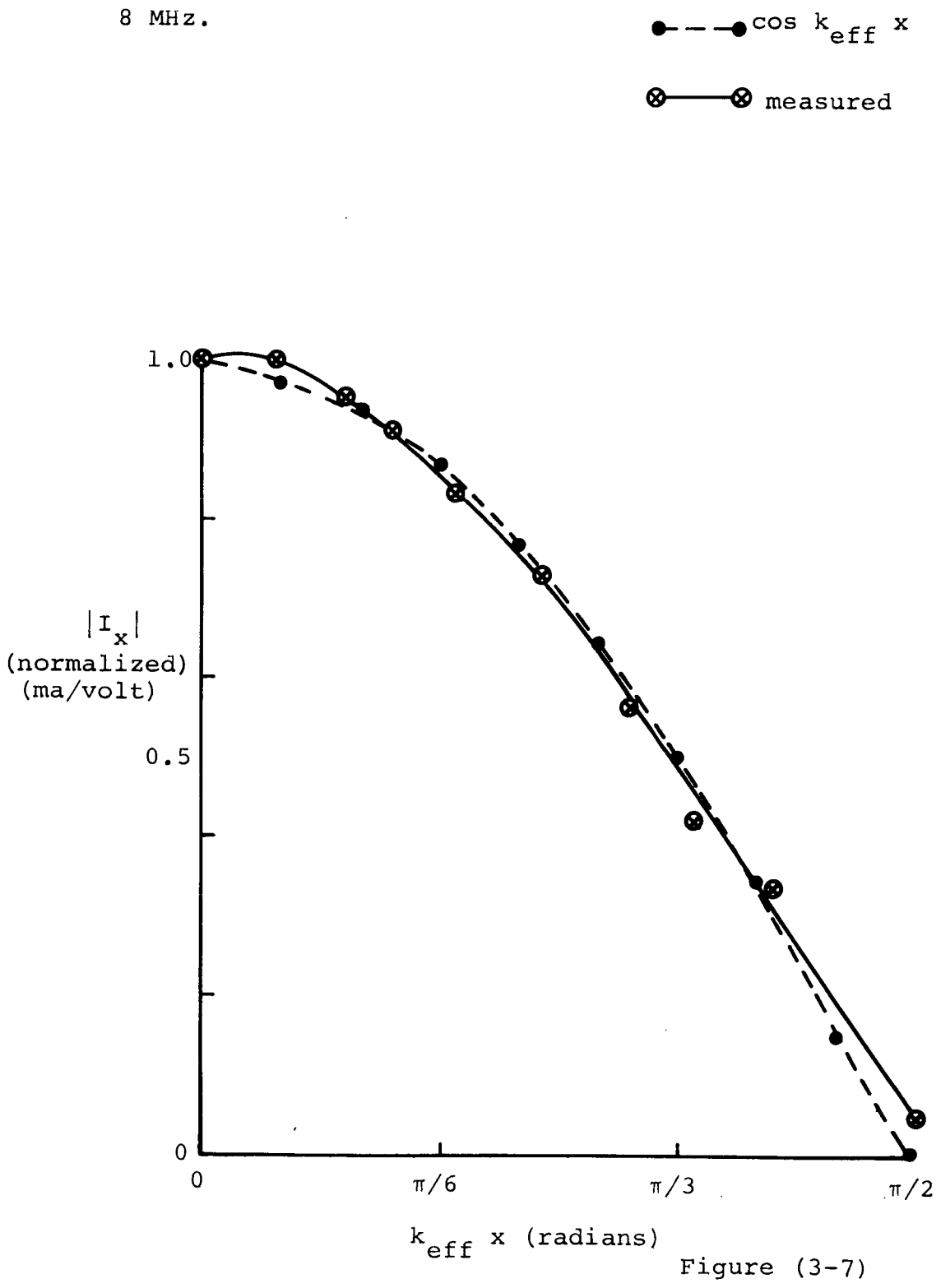

Figure (3-7)

Current Distribution for
Multi-Frequency Antenna
16 MHz.

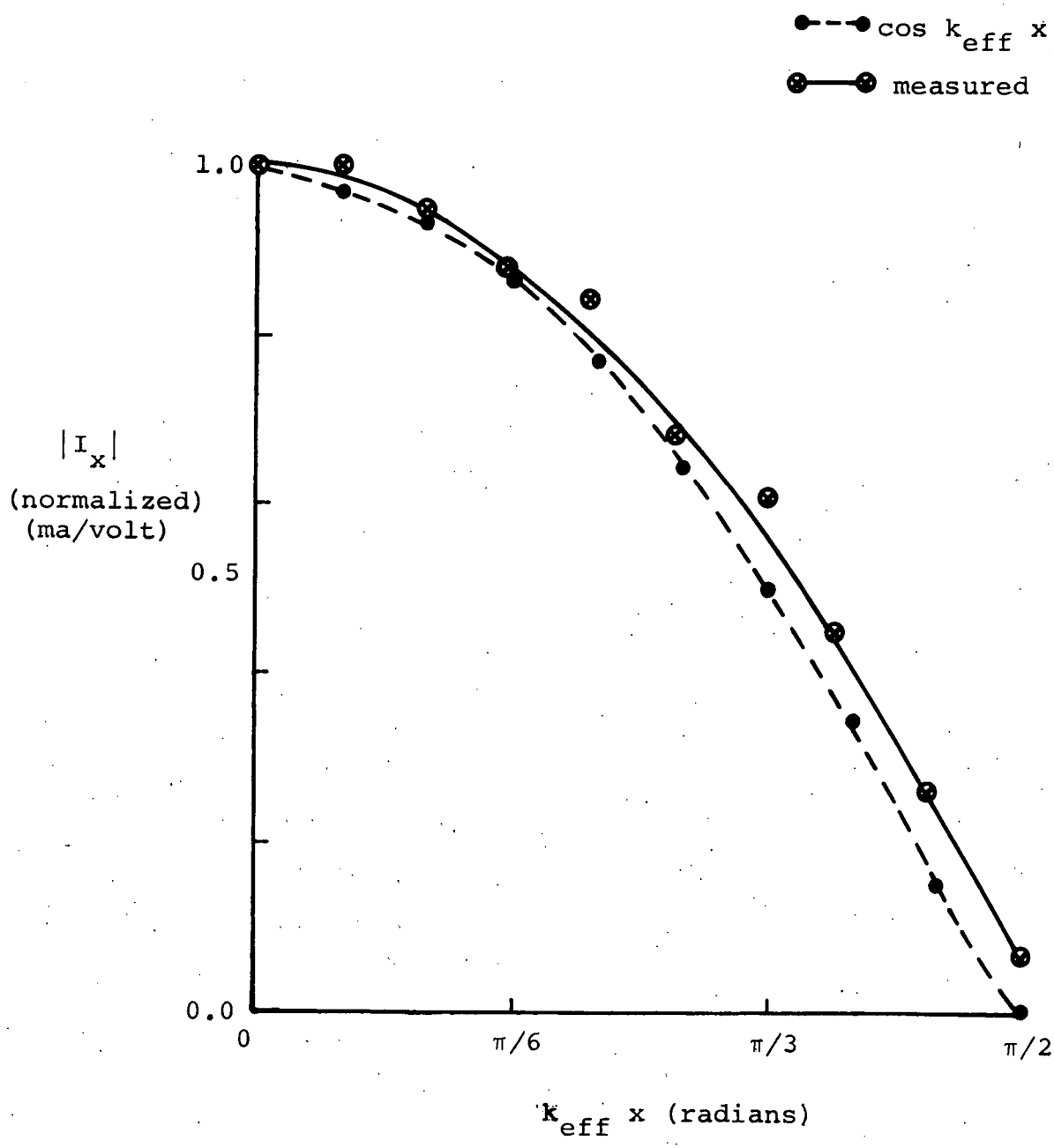

Figure (3-8)

Current Distribution for
Multi-Frequency Antenna
32 MHz.

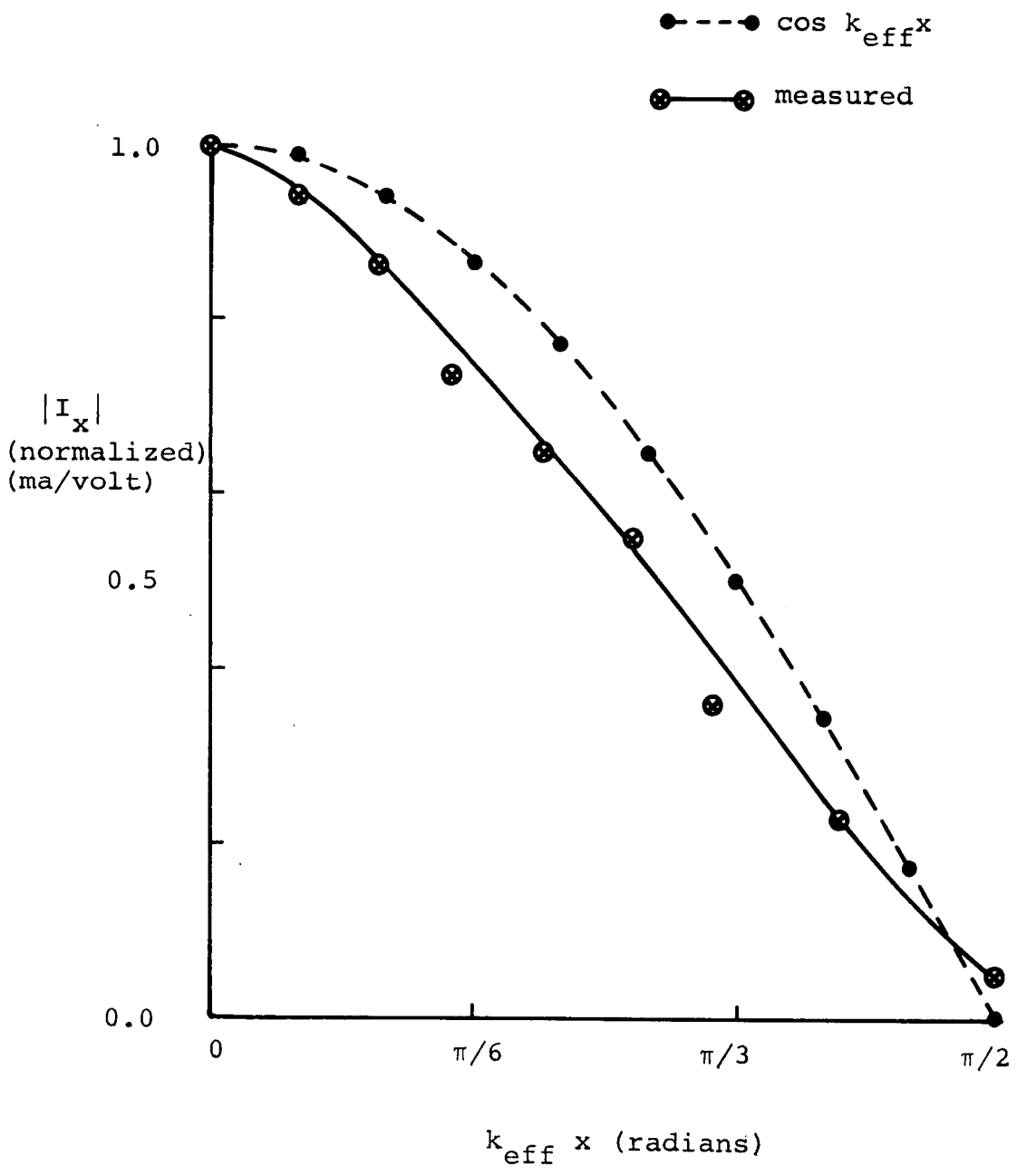

Figure 3-9

3.3 Field Calculations

3.3.1 Far Field Formulation

The equation for the current distribution for a half wavelength HED at the interface between two dielectrics can be approximated as:

$$I(x) = I_1 e^{j\psi_1} \cos k_{eff} x + I_2 e^{j\psi_2} (\sin k_{eff} |x| - 1) \qquad (3\text{-}14)$$

where x = the distance along the antenna length from the antenna phase center.

The half wavelength HED antenna is assumed to consist of a spatially continuous array of infinitesimal HED's whose excitation amplitudes are described by the amplitude of the current distribution at each point on the antenna length. As illustrated in Figure 3-10, the amplitude of the current of an infinitesimal HED at any point x on the half wavelength antenna is represented by the equation:

$$dI = I(x)\,dx \qquad (3\text{-}15)$$

As also illustrated in Figure 3-10, the distance from any point x on the antenna to the observation point P (r,θ,ϕ) is represented by the equation.

$$r_x = \left(r^2 + x^2 - 2xr\sin\theta\cos\phi\right)^{\frac{1}{2}} \qquad (3\text{-}16)$$

$$\cong r - x\sin\theta\cos\phi \qquad (3\text{-}17)$$

Half Wavelength Dipole
Over Stratified Medium

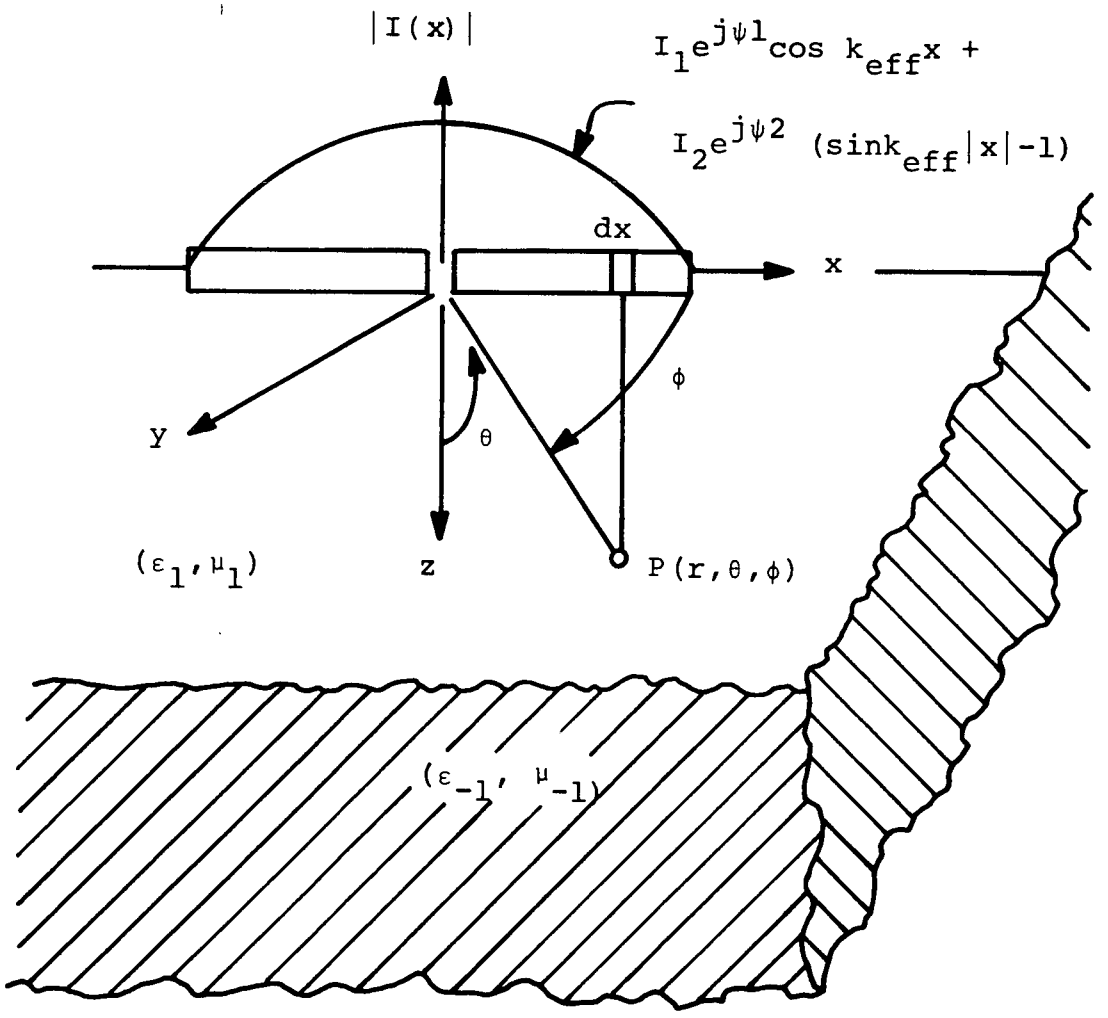

FIGURE (3-10)

and the half-space, far field solution for the normalized component of the vertical magnetic field per unit dipole moment is represented by the equation:

$$H_{z_i}^{N} = \frac{2}{L} \frac{H_{z_{0,i}}}{\sqrt{I_1^2 + I_2^2}} \int_{-\frac{L}{2}}^{\frac{L}{2}} I(x) e^{jk_{c_i} x \sin\theta \cos\phi} dx \qquad (3\text{-}18)$$

and the result of this integration (See Appendix A-3) is:

$$H_{z_i}^{N} = H_{z_{0,i}} \sin\phi \, M_i^{\xi}(\theta,\phi) \qquad (3\text{-}19)$$

where $$M_i^{\xi} = \frac{I_1}{\sqrt{I_1^2 + I_2^2}} e^{j\psi_1} M_i - \frac{I_2}{\sqrt{I_1^2 + I_2^2}} e^{j\psi_2} (N_i + O_i) \qquad (3\text{-}20)$$

$$M_i = \frac{4}{\pi} \left\{ \frac{\cos\left[\sqrt{\frac{\epsilon_i}{\epsilon_{eff}}} \frac{\pi}{2} \sin\theta \cos\phi\right]}{1 - \frac{\epsilon_i}{\epsilon_{eff}} \sin^2\theta \cos^2\phi} \right\} \qquad (3\text{-}21)$$

$$N_i = \frac{4}{\pi} \left\{ \frac{\left(\sqrt{\frac{\epsilon_i}{\epsilon_{eff}}} \sin\theta \cos\phi\right)\left(\sin\left(\sqrt{\frac{\epsilon_i}{\epsilon_{eff}}} \frac{\pi}{2} \sin\theta \cos\phi\right)\right)}{1 - \frac{\epsilon_i}{\epsilon_{eff}} \sin^2\theta \cos^2\phi} \right\} \qquad (3\text{-}22)$$

and

$$O_i = \frac{4}{\pi} \left\{ \frac{\sin\left[\sqrt{\frac{\epsilon_i}{\epsilon_{eff}}} \frac{\pi}{2} \sin\theta \cos\phi\right]}{\sqrt{\frac{\epsilon_i}{\epsilon_{eff}}} \sin\theta \cos\phi} \right\} \tag{3-23}$$

Correspondingly, far from the transmitting antenna the normalized radial and tangential magnetic field components can be represented by the equations:

$$H_{\rho_i}^N = H_{\rho_{o,i}} \sin\phi \, M_i^{\rho}(\theta,\phi) \tag{3-24}$$

$$H_{\phi_i}^N = H_{\phi_{o,i}} \cos\phi \, M_i^{\zeta}(\theta,\phi) \tag{3-25}$$

With equations (3-9) through (3-25) and the dual relationships for the electric field components, the half-space surface fields and the radiation patterns of a half wavelength HED antenna are determined in the following paragraphs.

3.3.2 Half-Space Surface Fields

The half-space surface fields are formulated by substituting the asymptotic solutions for the half-space magnetic fields $H_{z_{0,i}}$ $H\rho_{0,i}$, and $H\phi_{0,i}$ into equations (3-19) through (3-25). For example, the half-space surface magnetic field component $H\rho_0$ is represented by the equation[2]:

$$H_{\rho_o} = -2a_t \sin\phi \left\{ \frac{H_{-1}}{H_1 \underline{K}} \frac{K_{c_1}}{R} G_1 - \frac{H_1}{H_{-1}(-j\underline{K})} \frac{K_{c_{-1}}}{R} G_{-1} \right\} \tag{3-26}$$

where $$\underline{K} \triangleq \sqrt{K_{c_{-1}}^2 - K_{c_1}^2} = K_{c_1} K \tag{3.27}$$

$$K \triangleq \sqrt{c_{-1}} \tag{3-28}$$

$$c = \frac{\epsilon_{-1}}{\epsilon_1} \tag{3-29}$$

and $$G_i = \frac{e^{-jK_{c_i}R}}{4\pi R} \tag{3-30}$$

By combining equations (3-24) and (3-26) and neglecting the near field cross coupling between the radial and tangential surface fields as illustrated in Appendix A-3, the radial magnetic surface field component for the half wavelength HED antenna can be represented by the equation:

$$H_\rho^{SN} \cong -2a_t \sin\phi \left\{ \frac{H_{-1}}{H_1 \underline{K}} \frac{K_{c_1}}{R} G_1 M_{+1}^{\xi}\left(\tfrac{\pi}{2}, \phi\right) - \frac{H_1}{H_{-1}(-j\underline{K})} \frac{K_{c_{-1}}}{R} G_{-1} M_{-1}^{\xi}\left(\tfrac{\pi}{2}, \phi\right) \right\} \tag{3-31}$$

where M_i^{ξ} is described in equation (3-20).

The major effect of the finite size of the half wavelength antenna is to narrow the beamwidths of the TE circular field patterns and to broaden the beamwidths of the TM circular field patterns. The beamwidth is defined as angular spread over which the amplitude of the circular field pattern is

greater than 0.707 of its maximum value. To illustrate the effects of the finite size of the antenna, the circular far field patterns for TE and TM fields are shown in Figures (3-11) and (3-12) for the simplifying assumptions and subsurface electrical properties listed below:

Assume: $$I_2 << I_1 \tag{3-32}$$

and $$\psi_1 = 0 \tag{3-33}$$

with the result

$$M_i^{\xi} \cong M_i \tag{3-34}$$

The electrical properties of the subsurface are represented by equations:

$$\frac{\varepsilon_{-1}}{\varepsilon_1} = \frac{\varepsilon_{-1}}{\varepsilon_0} = 3.2 \tag{3-35}$$

$$\mu_{-1} = \mu_1 = \mu_0 \tag{3-36}$$

The beamwidth of the circular field pattern for TE fields in medium (+1) is larger than the beamwidth of the field pattern for TE fields in medium (-1); however, the beamwidths of the TM circular field patterns are larger in medium (-1) than in medium (+1) as illustrated in Table 3-2 for $K_{\varepsilon_{-1}} = 3.2$.

TE Circular Patterns for
Half Space Surface Fields

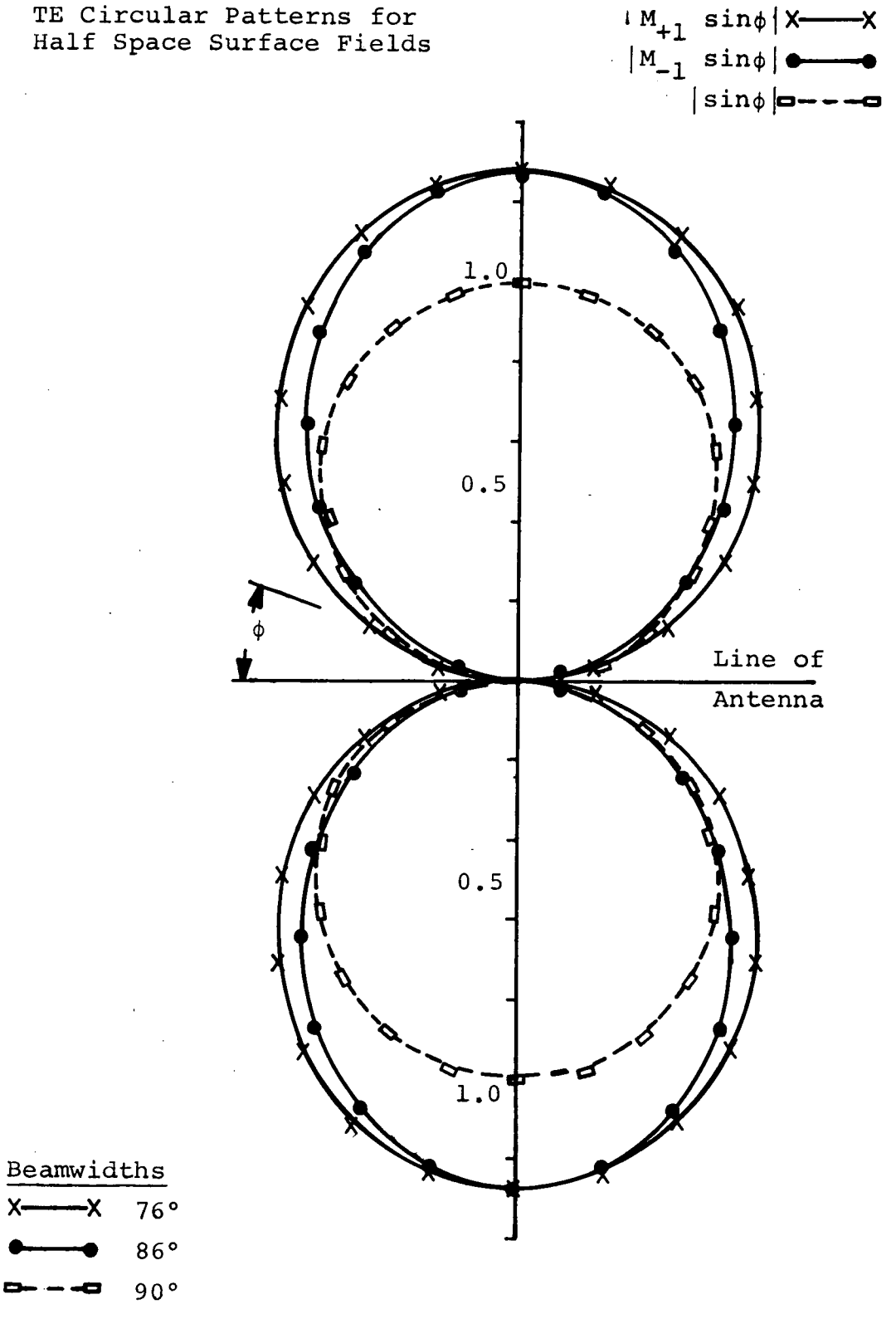

Figure 3-11

TM Circular Patterns for
Half-Space Surface Fields

$|M_{+1} \cos \phi|$ X——X
$|M_{-1} \cos \phi|$ ●——●
$|\cos \phi|$ □- - -□

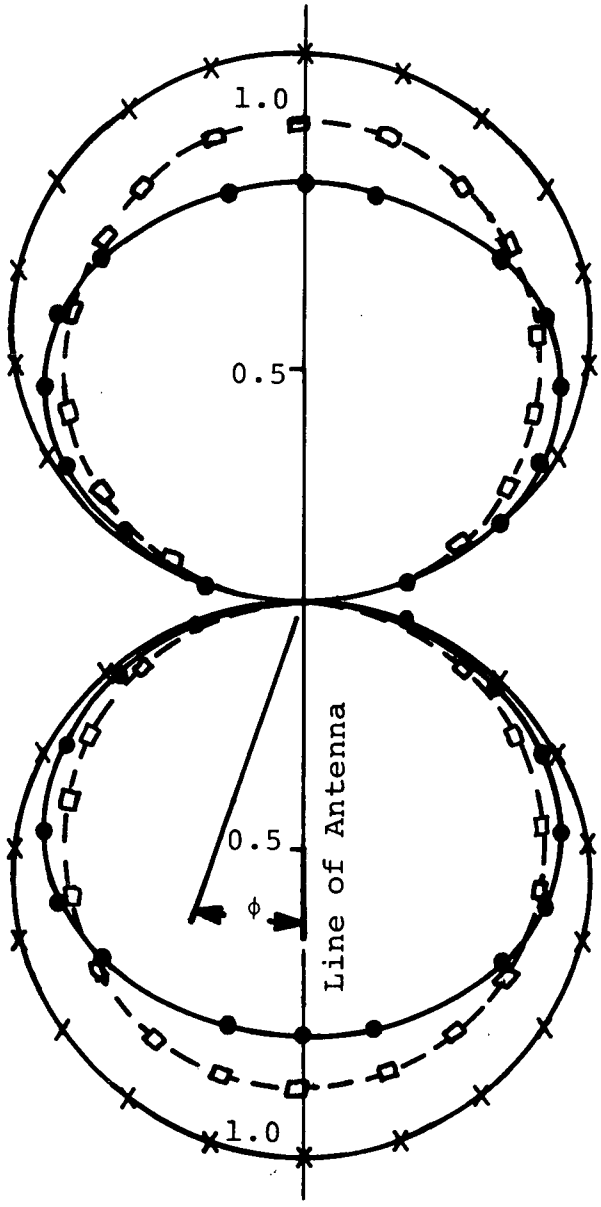

Beamwidths

X——X —— 100°

●——● —— 116°

□- -□- - - 90°

Figure 3-12

TABLE 3.2 SURFACE FIELD PATTERN BEAMWIDTHS

Medium	TE BEAMWIDTH Half Wavelength HED	TM BEAMWIDTH Half Wavelength HED	TE BEAMWIDTH Infinite-simal HED	TM BEAMWIDTH Infinite-simal HED
+1	86°	100°	90°	90°
-1	76°	116°	90°	90°

As the dielectric constant in medium (-1) is increased (with $K_{\varepsilon+1} = 1$ and $K_{eff}\left(\frac{L}{2}\right) = \frac{\pi}{2}$, the TE beamwidth will approach (72°) in medium (-1) and 90° in medium (+1). The TM beamwidth in medium (+1) will approach 90° and the TM beamwidth in medium (-1) will approach 134°. These beamwidth calculations are obtained by noting that as ε_{-1} is increased, the array factor in term M_i in equation (3-20) asymptotically approaches the values:

$$M_{+1} \rightarrow \frac{4}{\pi}\left\{\frac{\cos\left(\sqrt{\frac{2}{K_{\epsilon_{-1}}}}\,\frac{\pi}{2}\cos\phi\right)}{1-\frac{2}{K_{\epsilon_{-1}}}\cos^2\phi}\right\} \underset{K_{\epsilon_{-1}}\rightarrow\infty}{\rightarrow} \frac{4}{\pi} \qquad (3\text{-}37)$$

$$M_{-1} \rightarrow \frac{4}{\pi}\left\{\frac{\cos\left(\sqrt{2}\,\frac{\pi}{2}\cos\phi\right)}{1-2\cos^2\phi}\right\} \qquad (3\text{-}38)$$

$K_{\epsilon_{-1}} \rightarrow \infty$

and by calculating the beamwidths from the asymptotic patterns. To reiterate, the above solutions are valid only for the assumption represented by equation (3-32). However, this assumption is accurate to within 15% for loss tangents of the order of 0.075 which is near the upper limit of the expected loss tangents of the lunar subsurface. At 1 and 2 MHz, the loss tangents of glacial ice are approximately 0.3 and 0.15, respectively, for which equation (3-32) is not valid. Using the current distribution coefficients in Table 3-1, plots of the TE and TM surface field patterns for the one MHz antenna are illustrated in Figures 3-13 and 3-14, for the parameters listed in equations 3-35 and 3-36.

3.3.3 Half-Space Radiation Patterns

An infinitesimal HED oriented along the x axis on the surface has a TE radiation pattern in the yz plane ($x = 0$, $\phi = \pi/2$) and a TM radiation pattern in the xz plane ($y = 0$, $\phi = 0$) as illustrated in Figures 2-3 and 2-4. The gain of the infinitesimal HED is described below as a function of the bearing angle:

$$G^{I} = G_{TE}^{I} \sin^2\phi + G_{TM}^{I} \cos^2\phi \qquad (3\text{-}39)$$

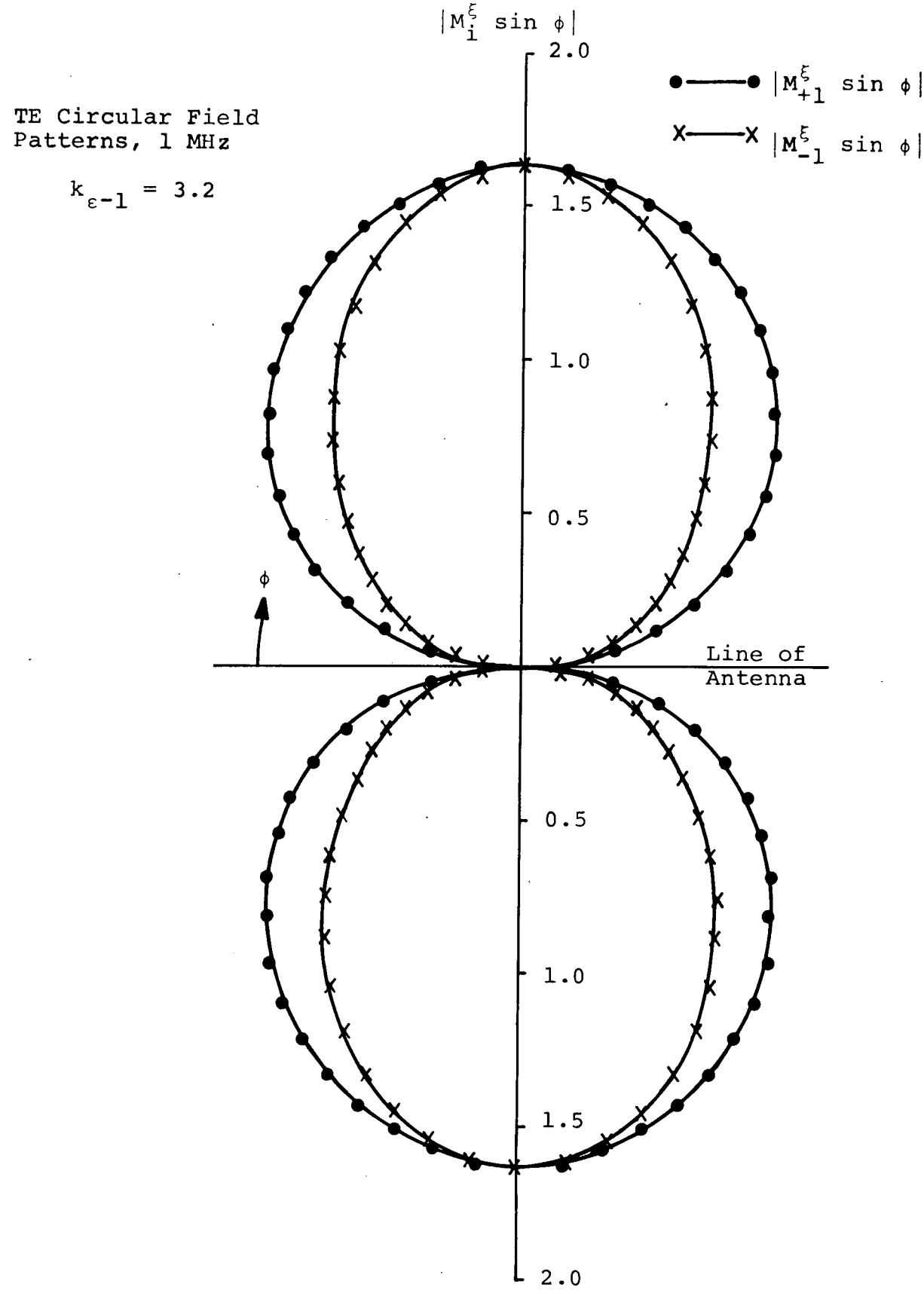
$|M_i^\xi \sin \phi|$
2.0
$|M_{+1}^\xi \sin \phi|$
$|M_{-1}^\xi \sin \phi|$
TE Circular Field
Patterns, 1 MHz
$k_{\varepsilon-1} = 3.2$
1.5
1.0
0.5
ϕ
Line of
Antenna
0.5
1.0
1.5
2.0

Figure 3-13

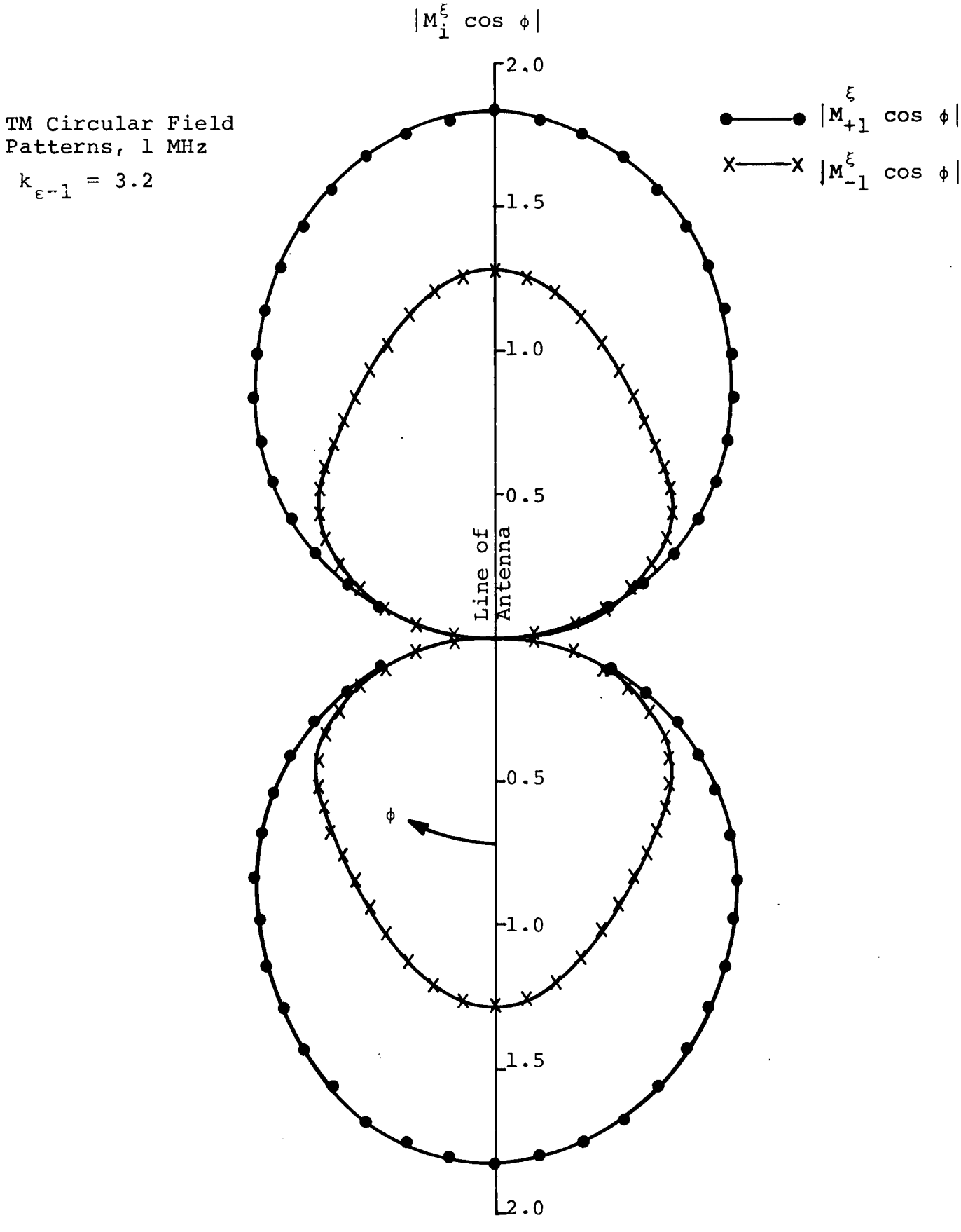
$|M_i^{\xi} \cos \phi|$
TM Circular Field Patterns, 1 MHz
$k_{\varepsilon-1} = 3.2$
$|M_{+1}^{\xi} \cos \phi|$
$|M_{-1}^{\xi} \cos \phi|$
2.0
1.5
1.0
0.5
Line of Antenna
0.5
1.0
1.5
2.0
ϕ

Figure 3-14

where

$$G_{TE} = \frac{\frac{dP}{d\Omega_i}\left(\theta, \frac{\pi}{2}\right)}{\frac{1}{4\pi}\sum_{\pm 1} P_i} \qquad (3\text{-}40)$$

and

$$G_{TM} = \frac{\frac{dP}{d\Omega_i}\left(\theta, 0\right)}{\frac{1}{4\pi}\sum_{\pm 1} P_i} \qquad (3\text{-}41)$$

For a half wavelength HED antenna, however, the gain equation from Appendix A-4 is:

$$G = G_{TE}\sin^2\phi\left|M_i^{\xi}\left(\theta, \tfrac{\pi}{2}\right)\right|^2 + G_{TM}\cos^2\phi\left|M_i^{\xi}\left(\theta, 0\right)\right|^2 \qquad (3\text{-}42)$$

where M_i^{ξ} is described by equation (3-20), and the TE and TM gains are described by the equations:

$$G_{TE} = \frac{\frac{dP}{d\Omega_i}\left(\theta, \frac{\pi}{2}\right)\left|M_i^{\xi}\left(\theta, \frac{\pi}{2}\right)\right|^2}{\frac{1}{4\pi}\sum_{i=\pm 1} P_i} \qquad (3\text{-}43)$$

and

$$G_{TM} = \frac{\frac{dP}{d\Omega_i}(\theta,0)\left|M_i^{\xi}(\theta,0)\right|^2}{\frac{1}{4\pi}\sum_{i=\pm 1} P_i} \qquad (3\text{-}44)$$

A single quadrant of a three-dimensional isometric drawing of the radiation pattern for a half wavelength dipole is shown in Figure 3-15 and the TE and TM radiation patterns for infinitesimal and half wavelength dipoles are illustrated in Figure 3-16 for the parameters listed in equations (3-35) and (3-36) and the assumptions listed below:

$$I_1^2 >> I_2^2 \qquad (3\text{-}45)$$

and

$$|M_i^{\xi}|^2 \cong M_i^2 \qquad (3\text{-}46)$$

With this assumption for the array factor, the radiation patterns are accurate to within 13% at 1 MHz and 4% at all other frequencies for the current distribution coefficients listed in Table 3-1. The TE and TM radiation patterns for the 1 MHz antenna without the assumption represented by equation (3-45) is illustrated in Figure (3-17).

The radiation patterns for the half wavelength and infinitesimal HED's in Figure (3-16) differ in the following respects:

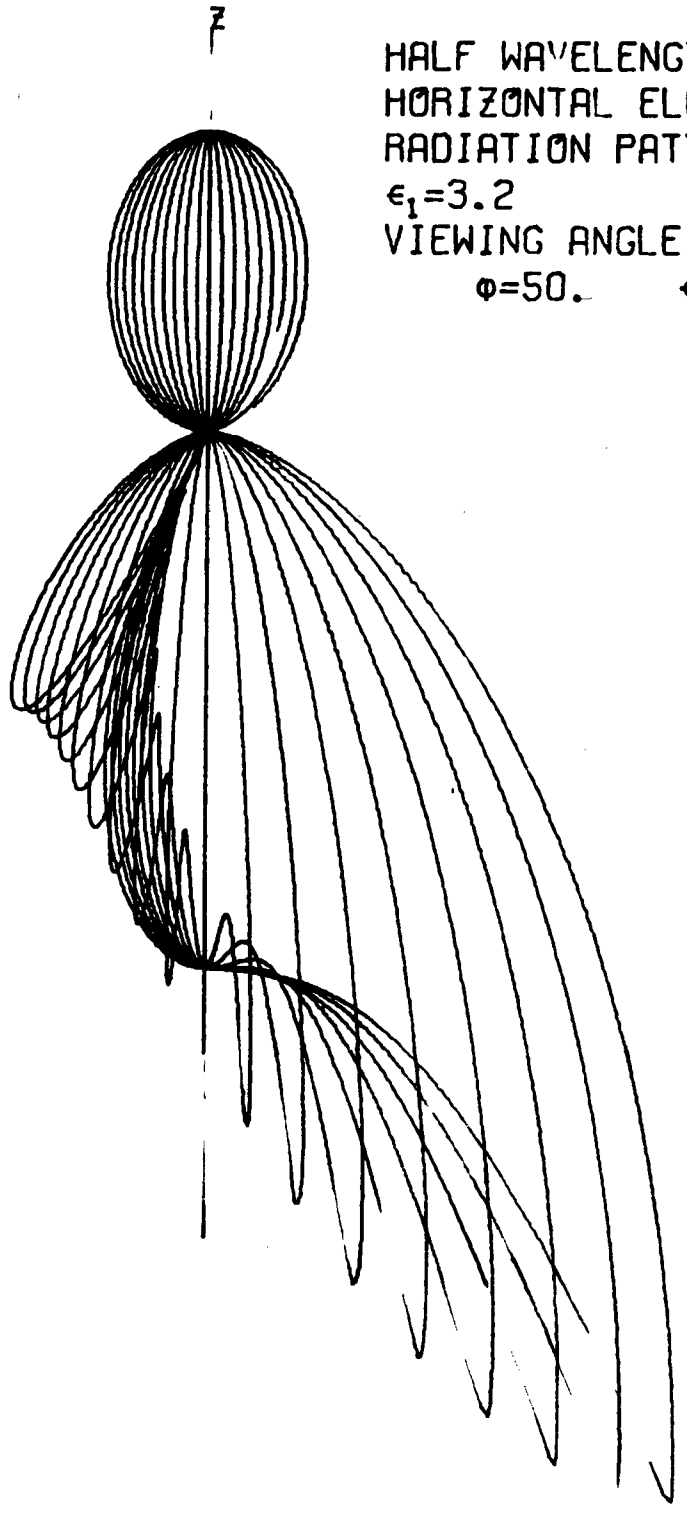
z
HALF WAVELENGTH
HORIZONTAL ELECTRIC DIPOLE
RADIATION PATTERN
ϵ_1=3.2
VIEWING ANGLE
φ=50.
θ=0.

Figure 3-15

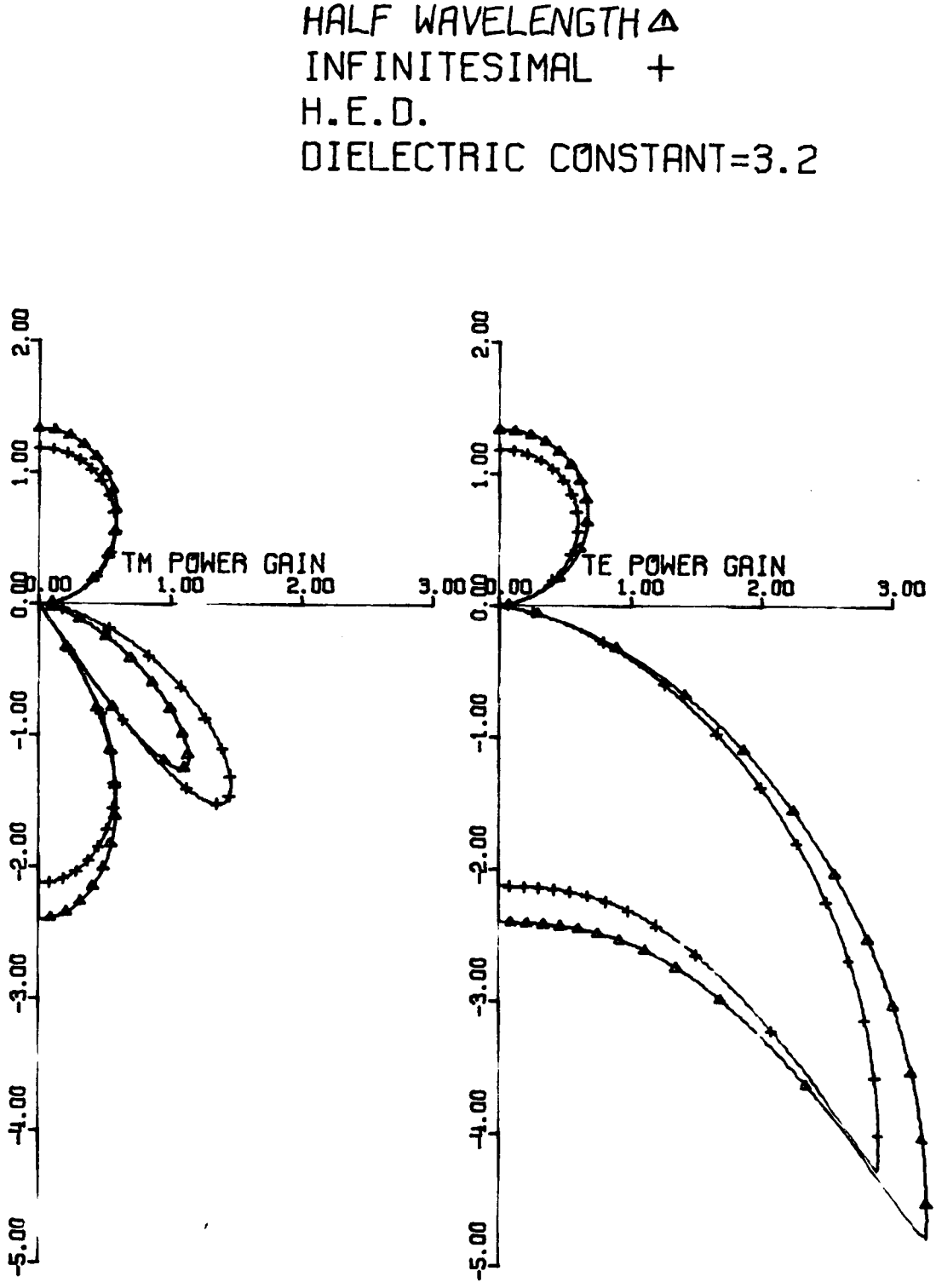
HALF WAVELENGTH Δ
INFINITESIMAL +
H.E.D.
DIELECTRIC CONSTANT=3.2
TM POWER GAIN
TE POWER GAIN
2.00
1.00
0.00
-1.00
-2.00
-3.00
-4.00
-5.00
1.00
2.00
3.00

Figure 3-16

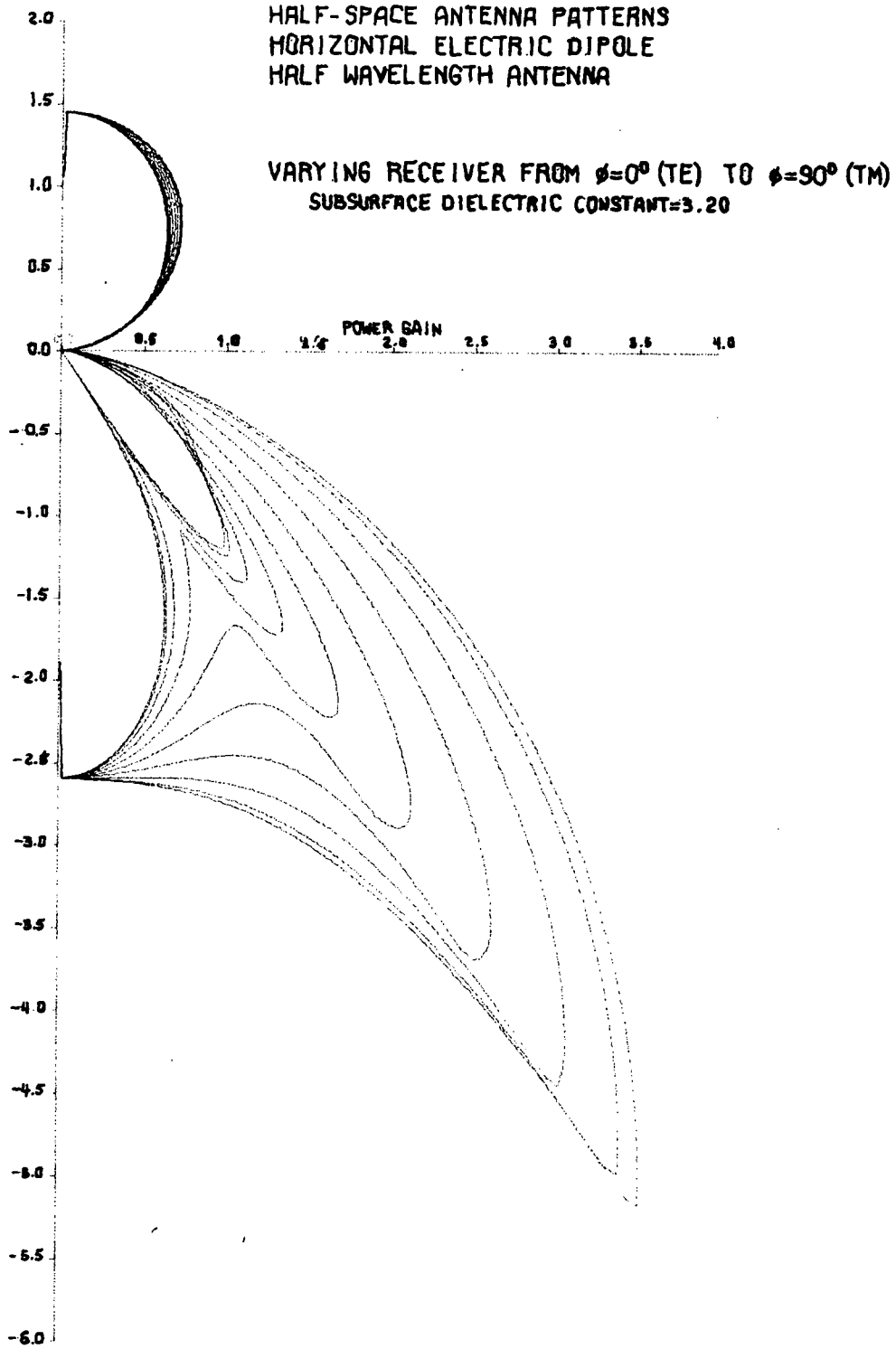
HALF-SPACE ANTENNA PATTERNS
HORIZONTAL ELECTRIC DIPOLE
HALF WAVELENGTH ANTENNA
VARYING RECEIVER FROM ϕ=0° (TE) TO ϕ=90° (TM)
SUBSURFACE DIELECTRIC CONSTANT=3.20
POWER GAIN
2.0
1.5
1.0
0.5
0.0
-0.5
-1.0
-1.5
-2.0
-2.5
-3.0
-3.5
-4.0
-4.5
-5.0
-5.5
-6.0
0.5
1.0
2.0
2.5
3.0
3.5
4.0

Figure 3-17

1. The TE lower space gain for the half wavelength antenna is larger than that for the infinitesimal HED by a factor of 1.10.
2. The TE/TM lower space vertical peak gain for the half wavelength antenna is larger than that for the infinitesimal HED by a factor of 1.13.
3. The lower space peak gain for the off-vertical TM lobe for the half wavelength antenna is smaller than that for the infinitesimal HED by a factor of 0.75.
4. The infinitesimal HED, for $\varepsilon_{-1}/\varepsilon_1 = 3.2$, has 72% of its total power radiated into the lower medium and the half wavelength HED has 70% of its power radiated into the lower medium.

3.3.4 The Special Case of a Thin Surface Layer

A half wavelength HED deployed over a two layer medium is illustrated in Figure (2-5). If the uppermost layer of the subsurface is thin with respect to a wavelength of the transmitted frequency, and the transmitting antenna is designed to be a half wavelength HED in a medium whose dielectric constant is the average dielectric constant of the layers (+1) and (-1), the lower space radiation pattern of the antenna can be approximated as the radiation pattern of a half wavelength antenna over medium (-2). For example, if the thickness (Δ) of the uppermost layer is 10 meters and the frequency considered is 1 MHz, the ratio of the thickness to the free space

wavelength is:

$$\frac{\Delta}{\lambda_0} = \frac{10}{300} \simeq 0.033 \qquad (3\text{-}47)$$

For a thickness to wavelength ratio of this order, the radiation pattern[2] is approximately that of the antenna over medium (-2) and for the dielectric constants:

$$\frac{\epsilon_{-1}}{\epsilon_1} = \frac{\epsilon_{-1}}{\epsilon_0} = 3 \qquad (3\text{-}48)$$

$$\frac{\epsilon_{-2}}{\epsilon_1} = \infty \qquad (3\text{-}49)$$

and $$K_{\epsilon_{eff}} = 2 \qquad (3\text{-}50)$$

The array factor for the radiation pattern can be approximated as:

$$\left|M_i^{\xi}\right|^2 \simeq \left[\frac{4}{\pi}\left\{\frac{\cos(\pi \sin\theta\cos\phi)}{1-4\sin^2\theta\cos^2\phi}\right\}\right]^2 \qquad (3\text{-}51)$$

Approximate radiation patterns as functions of the bearing angle are illustrated in Figures (3-18) and (3-19) for the constraints listed in equations (3-47) through (3-51) and for the extreme dielectric contrasts represented by the equations:

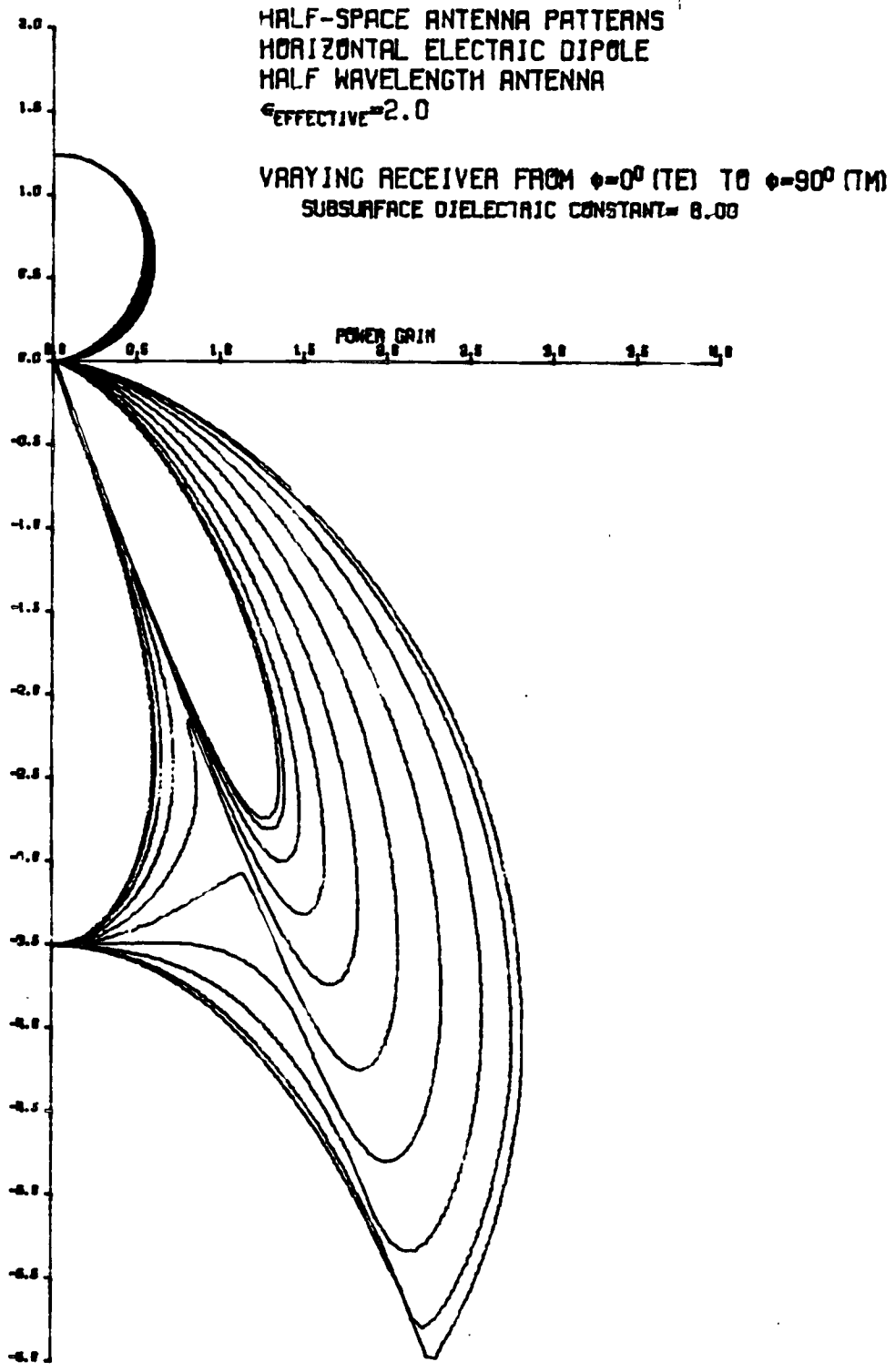
HALF-SPACE ANTENNA PATTERNS
HORIZONTAL ELECTRIC DIPOLE
HALF WAVELENGTH ANTENNA
$\epsilon_{EFFECTIVE}$=2.0
VARYING RECEIVER FROM ϕ=0° (TE) TO ϕ=90° (TM)
SUBSURFACE DIELECTRIC CONSTANT= 8.00
POWER GAIN

FIGURE 3-18

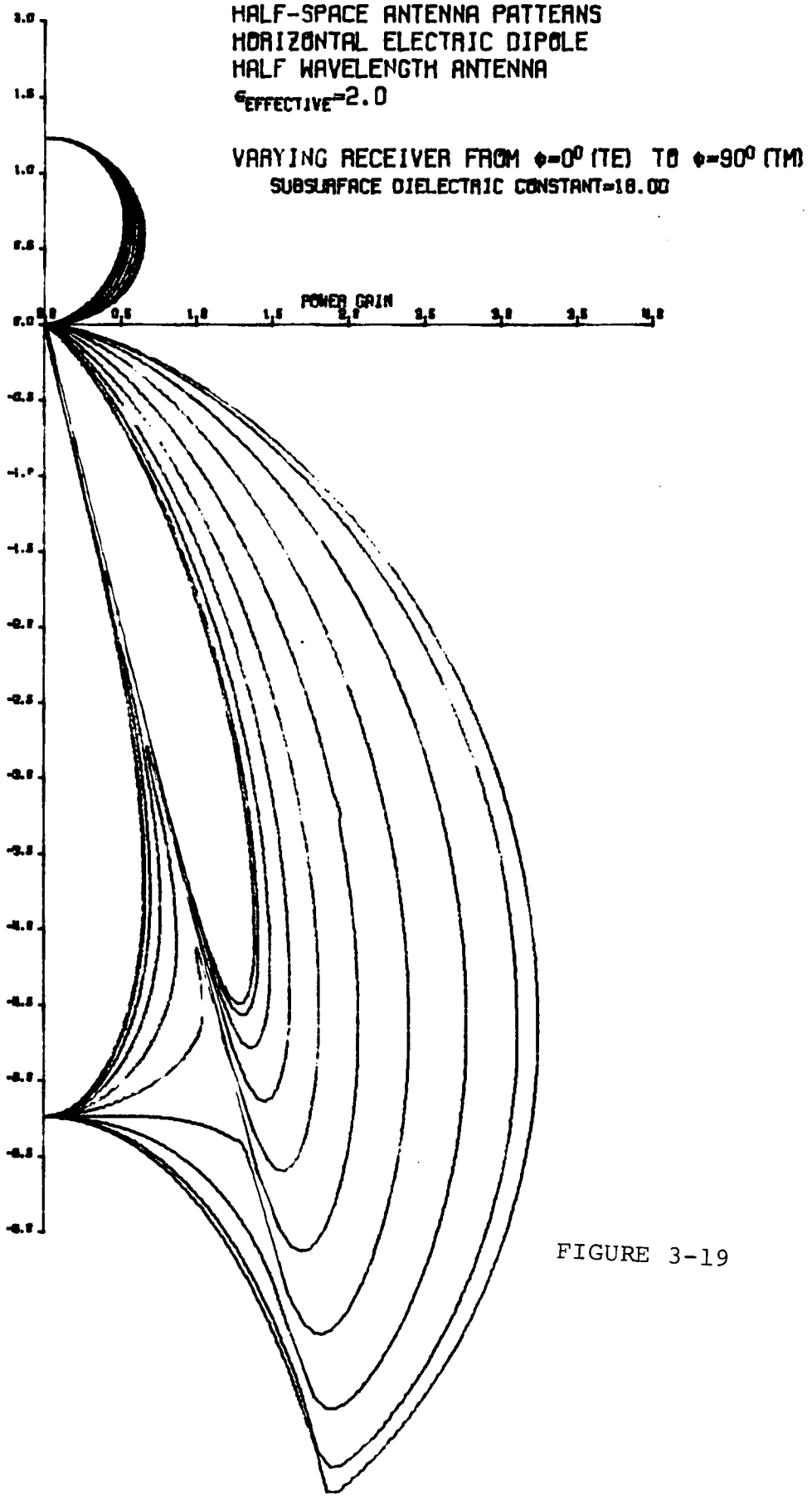
HALF-SPACE ANTENNA PATTERNS
HORIZONTAL ELECTRIC DIPOLE
HALF WAVELENGTH ANTENNA
$\epsilon_{EFFECTIVE}$=2.0
VARYING RECEIVER FROM ϕ=0° (TE) TO ϕ=90° (TM)
SUBSURFACE DIELECTRIC CONSTANT=18.00
POWER GAIN

FIGURE 3-19

$$\frac{\epsilon_{-2}}{\epsilon_1} = 18 \tag{3-52}$$

$$\frac{\epsilon_{-1}}{\epsilon_1} = \frac{\epsilon_{-1}}{\epsilon_0} = 3 \tag{3-53}$$

and

$$\left|M_1^{\frac{5}{2}}\right|^2 \simeq \left[\frac{4}{\pi}\left\{\frac{\cos\left[\frac{3\pi}{2}\sin\theta\cos\phi\right]}{1-9\sin^2\theta\cos^2\phi}\right\}\right]^2 \tag{3-54}$$

Since the current distribution remains that of a half wavelength antenna, no new lobes are introduced in the radiation patterns. In addition, the interference between air waves and lateral or surface waves should provide dielectric constant information with depth, i.e. the longer the wavelength of the transmitted frequency, the greater the depth over which the phase velocity of the subsurface lateral waves is averaged.

3.4 Summary

The fields induced by half wavelength dipoles over stratified media have been derived and compared with the fields induced by infinitesimal dipoles. The radiation patterns, the circular field patterns, and the surface fields have been derived to provide the basis for the analysis of data from practical applications of the radio interferometry technique such as the depth sounding of glaciers and the study of lunar

subsurface layering.

Chapter 4

Field Test Equipment for the Field Trials on the Athabasca Glacier

4.0 Introduction

A study of the applicability of the radio frequency interferometry technique to the determination of the sub-surface electrical properties of the moon has been conducted at M.I.T. and the University of Toronto since 1968. This study culminated in the award by NASA of a contract to M.I.T. and the University of Toronto for the design of the Lunar Surface Electrical Properties (SEP) experiment for Apollo 17. A subcontract was awarded to Raytheon Corporation for the hardware development.

As part of the pre-launch development of the SEP experiment, field trials were conducted on the Athabasca Glacier in Alberta, Canada. During these field trials, the current distribution measurements for half wavelength dipoles, used in Chapters 3 and 5 were obtained. A glacier was chosen as the site of the field trials, because glaciers are the only large scale media on earth that have electrical properties similar to the measured electrical properties of lunar samples. The major purposes of the field trials were to evaluate the SEP experiment hardware design, to develop the data reduction system, and to develop data analysis techniques.

When the SEP experiment progressed from the study phase of the contract to the hardware development phase in February

of 1971, an immediate goal in the hardware development was the design, construction, and field testing of the SEP Field Evaluation Model (FEM). The parallel developments of a data reduction system and peripheral test equipment were undertaken to provide the basis for a complete field evaluation of the SEP hardware design.

Raytheon Corporation personnel in Sudbury, Massachusetts, designed, constructed, and electrically tested the FEM. The system integration of the FEM and data recording equipment into an all-terrain tracked vehicle was accomplished at M.I.T. in Cambridge, Massachusetts. The data reduction system (DRS), including an interface between the recording equipment and a small, programmable calculator, was designed and developed at NASA Manned Spacecraft Center in Houston, Texas.

All of this equipment was available for field use in early July 1971 and field tests were conducted on the Athabasca Glacier in Alberta, Canada through the first week in September 1971. The field equipment and the logistics of the field trials are described in the following sections.

4.1 Field Test Hardware

The SEP field test hardware can be divided into two general categories: the field test equipment for gathering data on the glacier, and the field test equipment for performing data reduction and analysis at the field camp site. The field test equipment for gathering data on the glacier can be subdivided into the following categories:

1) the SEP Field Evaluation Model

2) the data recording equipment

3) the instrumented all-terrain vehicle

4.1.1 Field Evaluation Model

The FEM consists of a transmitter, transmitting antennas, receiver, and receiving antennas. The FEM was constructed to withstand the rigors of glacier use and constrained to be compatible with commercial recording equipment. The FEM mechanical design was not constrained to the rigid weight, size and thermal requirements applicable to the flight model design so there is no mechanical resemblance between the flight model and the FEM. However, the FEM was designed to be an electrical analog of the flight model with the following exceptions:

1. The data sampling rate used in the flight model design is greater than the sampling rate used in the FEM.
2. The transmitting antenna design was tailored to the dielectric constant of glacier ice.
3. The signal frequencies of the FEM design are 1,2,4,8,16 and 32 MHz; whereas, the signal frequencies of the flight hardware design are 1,2.1,4,8.1,16 and 32.1 MHz.
4. Circuits were added to the FEM transmitter to provide the capability of continuous wave operation at each of the SEP experiment frequencies.

5. Sample and hold circuits were added to the FEM receiver to provide electrical output signals proportional to the measured field strengths and compatible with the input circuits of a multi-channel chart recorder.

The FEM transmitter illustrated in Figure 4-1 was deployed on the glacier surface and connected to two orthogonal horizontal electric field dipole (HED) antennas termed N-S and E-W antennas. Radio frequency power was radiated alternately from the two antennas. An alternate transmission mode was available for the continuous transmission of a selectable frequency from either antenna. RF power at the input terminals of the energized antenna was 3.75 watts at 1 MHz and 2 watts at all other frequencies. DC power was derived from a battery supply located within the transmitter casing.

The transmitting antennas of the FEM consisted of two 76 meter lengths of number 22 gauge wire with "traps" and "suppressors" interspersed along the antenna lengths. The traps and suppressors were resonant circuits located at multiples of quarter wavelengths from the antenna feed point. The purpose of these resonant circuits was to limit radiation at each frequency to the corresponding quarter wavelength antenna section nearest to the antenna feed point. In effect, each antenna was approximately a half wavelength electric field dipole at each SEP experiment frequency.

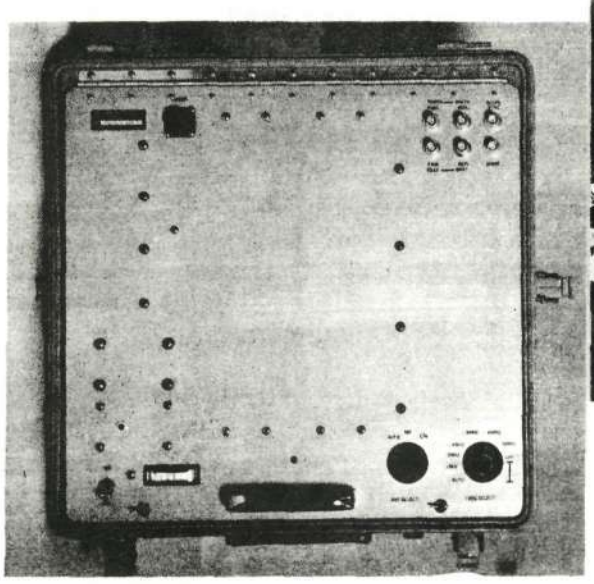

The front panel controls are added to provide the capability of performing antenna tests.

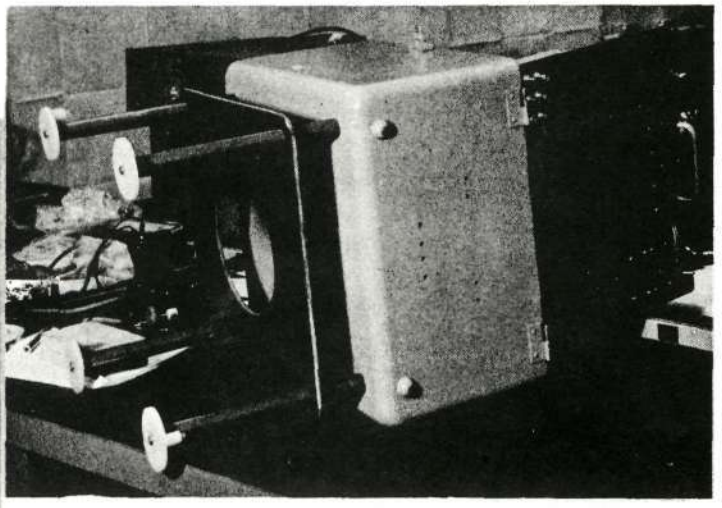

The transmitter is elevated from the glacier surface to provide protection from surface water.

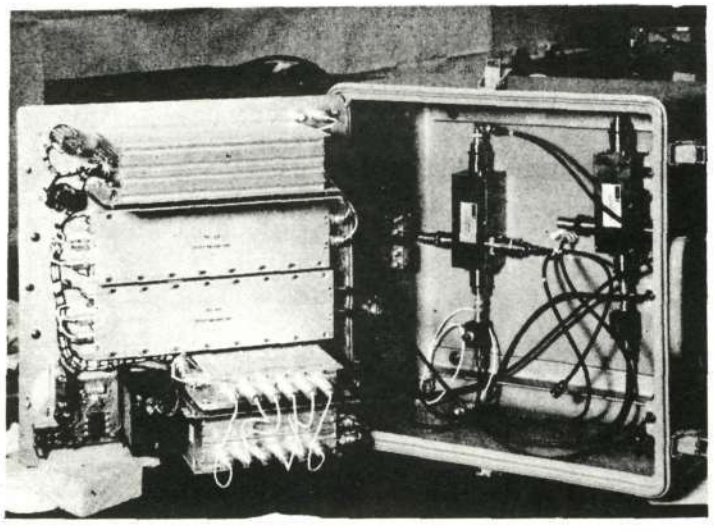

Hybrid circuits are provided in the transmitter house to permit antenna tests on the glacier.

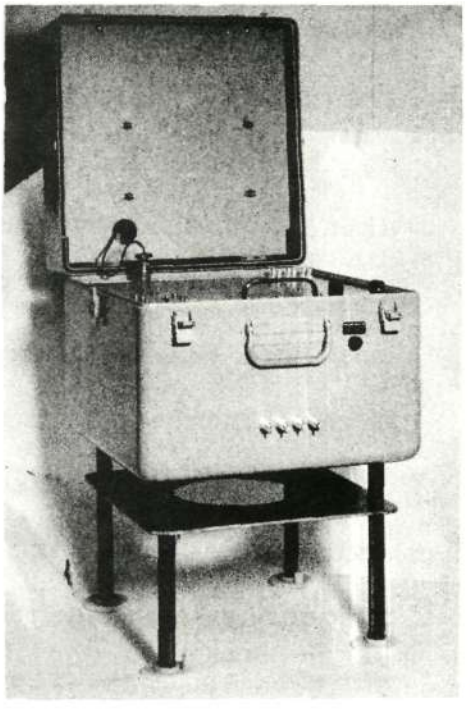

A battery supply is enclosed in the hinged lid.

Figure 4-1
FEM Transmitter

The FEM receiver illustrated in Figure 4-2 was a large rack-mountable assembly which was enclosed in an equipment rack in the tracked vehicle. The receiving antennas were attached to the receiver by a horizontal, cylindrical mast, four feet in length. Three receiving antennas labeled x, y, and z were orthogonal loop antennas designed to measure the orthogonal field components of the magnetic field on a vehicle-centered coordinate system. Reception occurred on each loop in a switching sequence coherent with the sequence of radiated frequencies illustrated in Figure 4-3. Signals proportional to the field strength of the orthogonal signal components induced at the loop antennas were recorded on magnetic tape. The receiver was maintained in time synchronization with the transmitter by the recognition of a particular sequence of pulses transmitted at the end of each data frame.

The data format used in the FEM is illustrated in Figure 4-3. Each subframe included eight intervals of 400 milliseconds. In each subframe, one interval was used for the recognition of synchronization between the transmitter and receiver and for the measurement of the temperature of the receiver, one interval was used for a gain calibration of the receiver, and the remaining six intervals were used for the measurement of the fields induced by the transmitter at each of the six experiment frequencies. During each of the six field measurement intervals, the transmitting antennas were energized alternately for 200 milliseconds each. In each 200

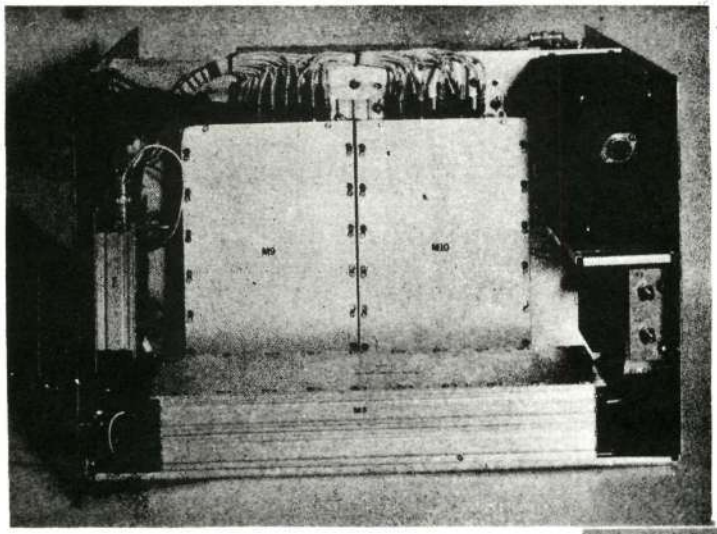

Breadboard type modules used in the FEM receiver are mounted in a standard 19" relay rack style chassis.

Sample and hold circuits were included in the FEM receiver as interface circuitry with a chart recorder.

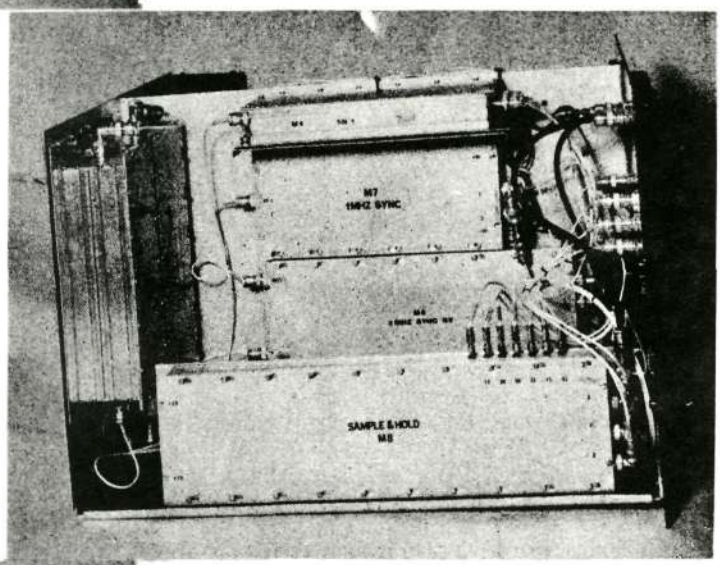

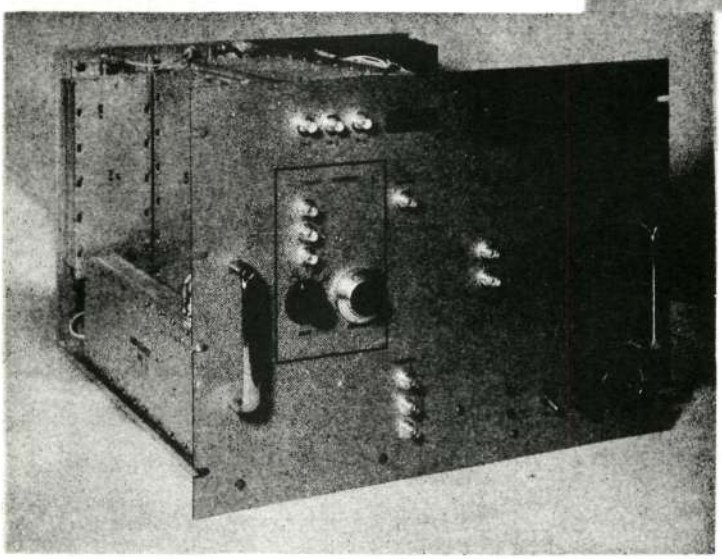

All interface connections are provided on the front panel.

Figure 4-2
FEM Receiver

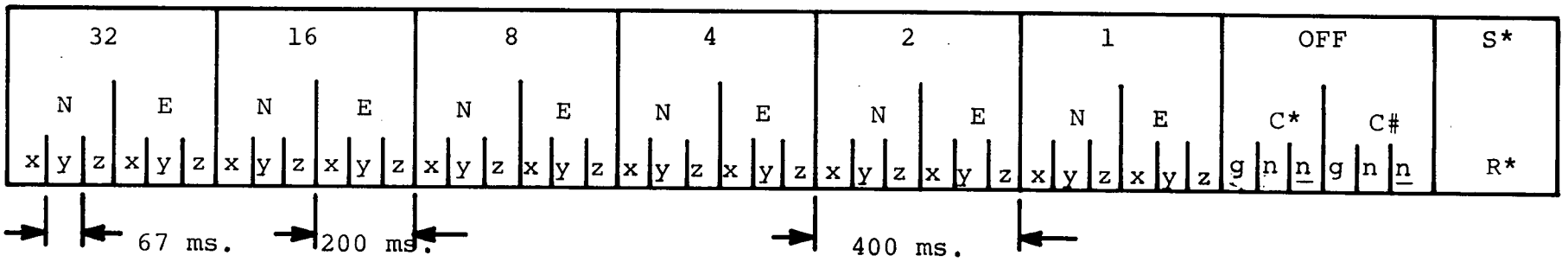

DATA FRAME = 6 x 3.2 = 19.2 seconds

	C* =	C# =	S* =	R* =
S1 - Subframe as above	32	16	N-S	x
S2 - Subframe as above	8	4	E-W	y
S3	2	1	N-S	z
S4	32	16	E-W	x
S5	8	4	N-S	y
S6	2	1	E-W	z

Figure 4.3 Data Format (Field Evaluation Model)

millisecond interval, the three receiving antenna output signals were sampled for 67 milliseconds each.

A full data frame in the transmitter included two subframes differentiated by the fact that the synchronization code was transmitted alternately on the N-S and E-W antennas in each subframe. A data frame in the receiver includes three subframes differentiated by the fact that the x, y, and z receiving antennas were used to sample the synchronization code transmission, and by the fact that the receiver gain calibration measurement was conducted at 32 & 16, 8 & 4 and 2 & 1 MHz in sequential subframes. Signal transmission was suspended during each sixteenth transmitter subframe, to provide a measure of the background noise in the vicinity of the receiver.

4.1.2 The Data Recording Equipment

The data recording equipment consisted of an analog seven-channel instrumentation tape recorder and a modified four-channel chart recorder. The purpose of the tape recorder was to record the following signals:

1. a 5200 Hz frequency reference from the FEM receiver;
2. a sequence of frequency modulated timing signals from the FEM receiver;
3. the voltage controlled oscillator (VCO) signal output from the FEM receiver;
4. an amplitude modulated 400 Hz signal from an odometer;

5. audio signals from a microphone.

The reasons for recording these signals are included in the description of the DRS in Section 4.2.1.

The purpose of the chart recorder was to provide a real-time visual display of the amplitudes of three received field components corresponding to a selected experiment frequency. The purchased chart recorder was designed to record the amplitude of an input signal on the vertical, or Y, axis versus time on the horizontal, or X, axis; in this mode of operation, the chart recorder paper is advanced by a synchronous motor drive. An alternate paper drive system was used to provide the capability of recording input signal versus distance traveled; in this mode of operation, the chart recorder paper was advanced by a servo-motor drive which was controlled by an odometer system such that the chart recorder paper was advanced at a rate proportional to the rate of speed of the vehicle as measured at the odometer wheel trailed behind the vehicle. During most of the field trials, the odometer drive system was used to advance the chart recorder paper.

4.1.3 Vehicle Instrumentation

The SEP experiment is a traverse experiment where data is gathered as the receiving equipment is conveyed across the lunar surface by the Lunar Roving Vehicle. A Thiokol IMP all-terrain tracked vehicle was rented and instrumented with the FEM receiver and antennas, recorders, and peripheral equipment, so that analogous traverse data could be taken over

the glacier surface. A picture of the instrumented vehicle at one of the glacier test sites is shown in Figure 4-4. The rear cab of the vehicle, a wooden structure, was designed and constructed at M.I.T., and mounted on the load platform of the tracked vehicle. The rear cab was used as an enclosure for the field test equipment and test personnel. The field test equipment was mounted in a console inside the rear cab. The equipment in the console included:

1. the FEM receiver;
2. the instrumentation tape recorder;
3. the chart recorder;
4. an audio amplifier and speaker;
5. an oscilloscope;
6. a DC/DC converter for supplying power to the tape recorder;
7. the odometer electronics and 400 Hz inverter;
8. a microphone.

Power for the test equipment was supplied by two 105 AH lead acid batteries mounted on the outside of the cab in a metal enclosure. The battery power was used directly in the form of 12 VDC and also in the form of 115 VAC, 60 Hz, through inverters. The inverters were mounted in a desk top enclosure beside the equipment console. Interconnection and power distribution diagrams are shown by Figures 4-5 and 4-6. The receiving antennas were mounted externally on a horizontal mast attached at one of the rear corners of the cab, and the odometer wheel was mounted on a bracket trailing behind

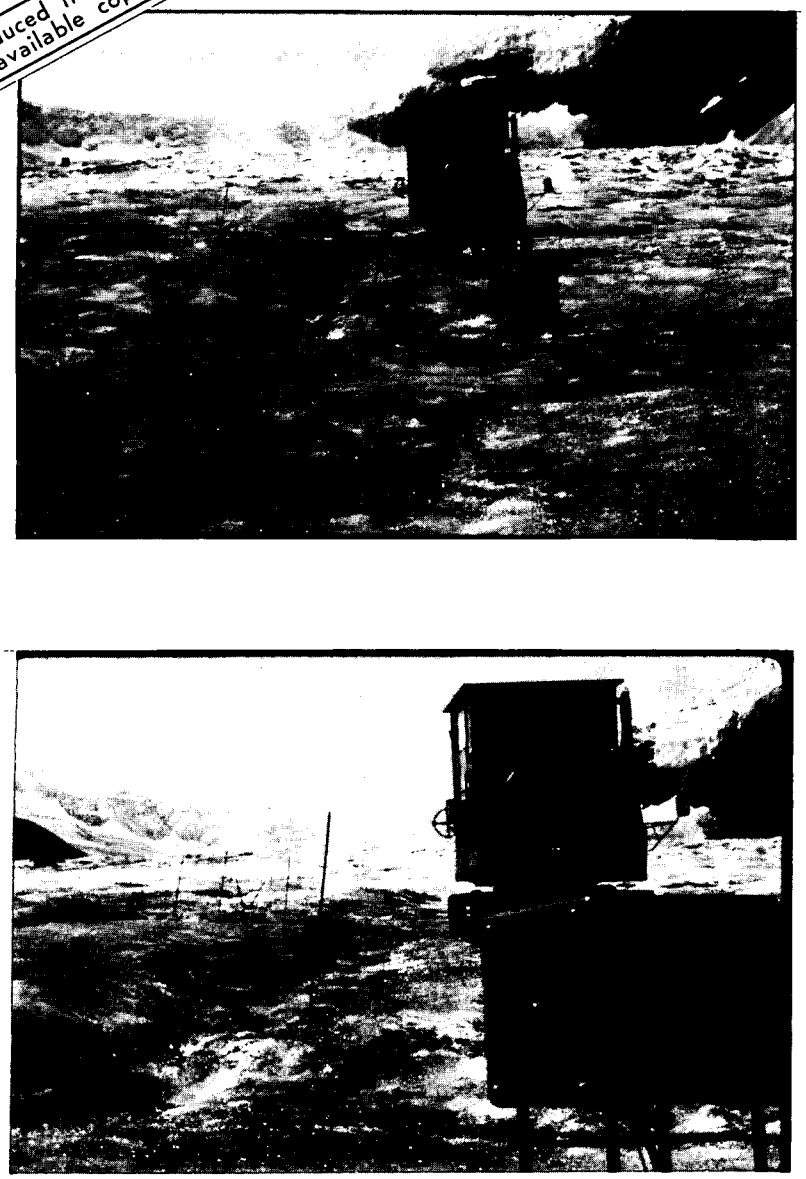

Figure 4-4
The SEP Field Test Equipment

FIELD TEST EQUIPMENT INTERCONNECTION DIAGRAM

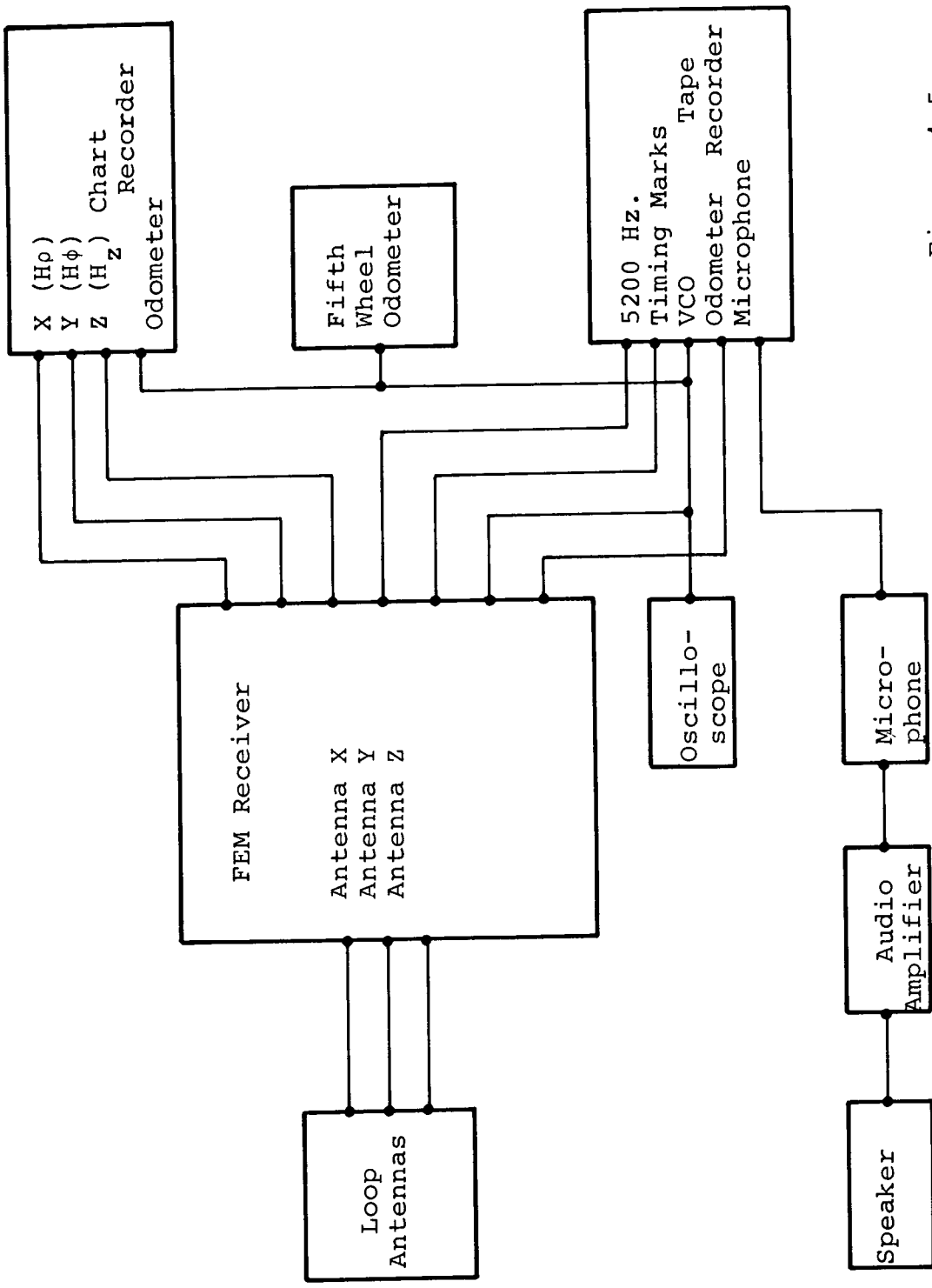

Figure 4-5

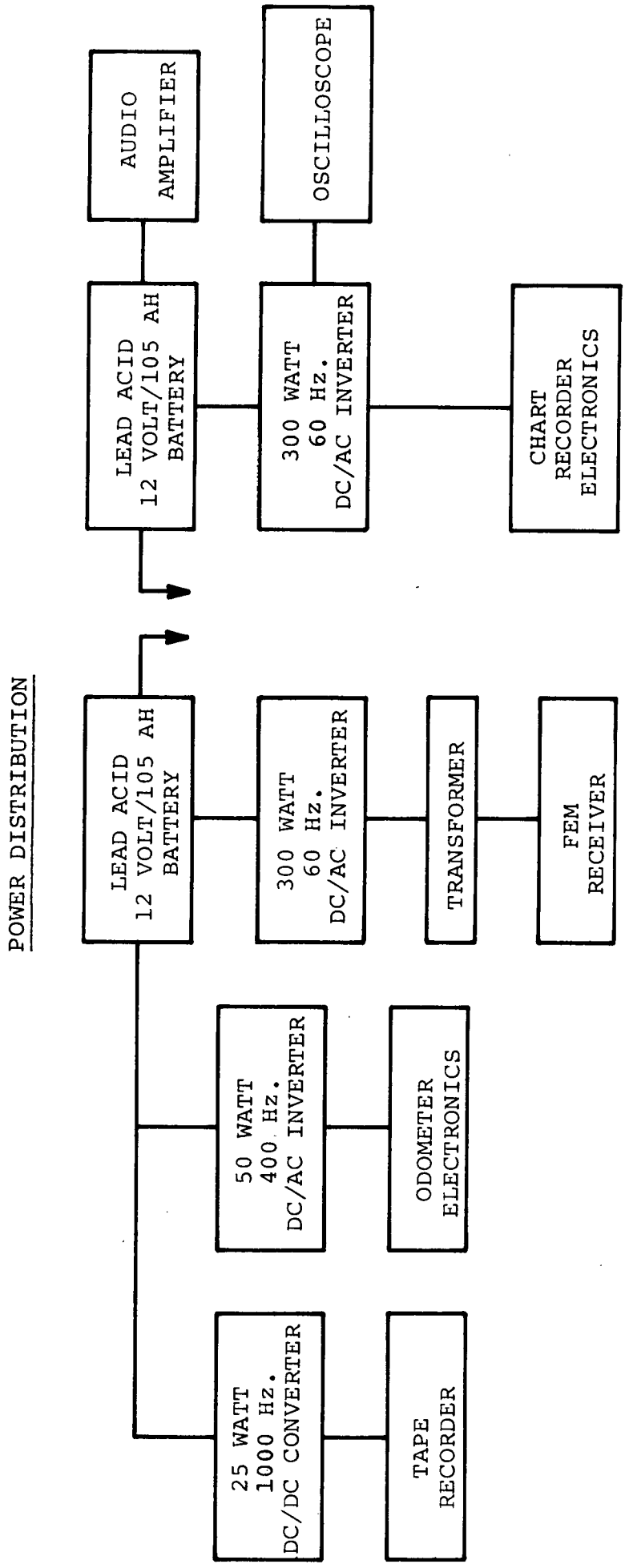
POWER DISTRIBUTION
LEAD ACID
12 VOLT/105 AH
BATTERY
300 WATT
60 Hz.
DC/AC INVERTER
TRANSFORMER
FEM
RECEIVER
50 WATT
400 Hz.
DC/AC INVERTER
ODOMETER
ELECTRONICS
25 WATT
1000 Hz.
DC/DC CONVERTER
TAPE
RECORDER
LEAD ACID
12 VOLT/105 AH
BATTERY
300 WATT
60 Hz.
DC/AC INVERTER
CHART
RECORDER
ELECTRONICS
AUDIO
AMPLIFIER
OSCILLOSCOPE

Figure 4-6

the tracked vehicle. Other features of the instrumented cab include:

1) two seats mounted in the rear cab for test personnel use;
2) a front shelf in the rear cab for storing supplies and peripheral equipment;
3) external brackets for holding rope and ice axes;
4) a heater mounted in the rear cab and connected to the cooling system of the tracked vehicle.

Communication between the personnel in the vehicle, at the camp site, and on the glacier, was provided by transceivers in the front cab of the vehicle and at the camp site, and by portable walkie-talkies. Communication between the vehicle driver in the front cab and test personnel in the rear cab was provided by an intercom system.

4.2 Field Test Equipment for Performing Data Reduction

The field test equipment for performing data reduction at the field camp site consisted of a magnetic tape reader, a data reduction system (DRS), and a programmable calculator. The output signals of the tape reader were connected directly to the DRS which converted the tape reader output signals into a digital form compatible with the input requirements of the calculator. The functions of the calculator, in turn, were to provide printouts and graphs of the data gathered

on the glacier. The magnetic tape reader and the calculator are commercially available equipment. The DRS, however, is a special purpose analog to digital converter which was designed and built at Manned Spacecraft Center, Houston, Texas. The operation of the DRS is described in the following paragraphs.

The signals recorded on the glacier are listed in Section 4.1.2. The first four of these signals were processed by the DRS. The fifth signal, the voice track, was used to provide identifications of the data runs and to record for posterity cryptic comments on the untold pleasures of gathering data over large masses of ice. The functions of the four inputs to the DRS are:

1. The 5200 Hz signal was used as a clock reference for the DRS.
2. The frequency modulated timing channel was used to provide recognition of the synchronization between the transmitter and receiver data channels and to indicate the beginning of each data sequence.
3. The VCO signal indicated the magnitude of the measured field data. The frequency recorded during each data frame was related to the field strength measured during the same data frame. In the frequency range of 300 to 3000 Hz and the signal power range of -135 dBm to -35 dBm,

referenced to the receiver input, the calibration of frequency versus signal power is given approximately by the numerical ratio of 2.7 Hz/dBm.

4. The amplitude modulated 400 Hz odometer signal was a measure of the distance travelled over the glacier surface by the instrumented tracked vehicle. Each zero crossing of the modulation was an indication of an incremental distance travelled of approximately 0.6 meters.

The DRS was designed to determine the beginning of a data sequence by the recognition of a unique signal time duration in the timing channel. This unique signal occurs immediately preceding the initiation of a data sequence. Synchronization between the transmitter and receiver data channels was determined by the recognition of synchronization confidence pulses in the timing channel. The 5200 Hz signal from the tape reader was used as the timing reference for determining the rate at which the VCO signal was to be sampled by the DRS. When synchronization was detected, the VCO signal was sampled at a rate consistent with the rate of the transmitted data. The number of cycles of the VCO signal in each sample were then counted to achieve analog to digital conversion. With the recognition of the beginning of a data sequence and the knowledge of the receiver mode

of operation, the sequence of samples of the digitized VCO signals were identifiable measures of the received fields. To complete the conversion of the analog signals into digital form, the odometer signals were digitized by the simple process of amplitude modulation detection of the 400 Hz signal and an odometer pulse was generated for each zero crossing of the modulation. The digitized VCO signals, the odometer pulses, and data sequence identification and initiation pulses constituted the inputs to the calculator. A block diagram illustrating the functions of the DRS is included as Figure 4-7.

4.3 Logistics

4.3.1 General Area of Glacier

The Athabasca Glacier was chosen as one site for the Surface Electrical Properties Experiment field trials because of its accessibility by tracked vehicle and its well-known topology. The Athabasca Glacier is located in the Jasper National Park in Alberta, Canada. The glacier is within 300 miles of two large industrial cities, Calgary and Edmonton, as illustrated in Figure 4.8. The small, tourist-oriented town of Jasper is only 65 miles from the glacier, and expendable supplies such as food, fuel and lumber can be obtained there. However, Calgary and Edmonton provide the closest industrial facilities and international airports. With permission from the National Parks Service, temporary living quarters and laboratory facilities were established in rented

BLOCK DIAGRAM OF DATA REDUCTION SYSTEM

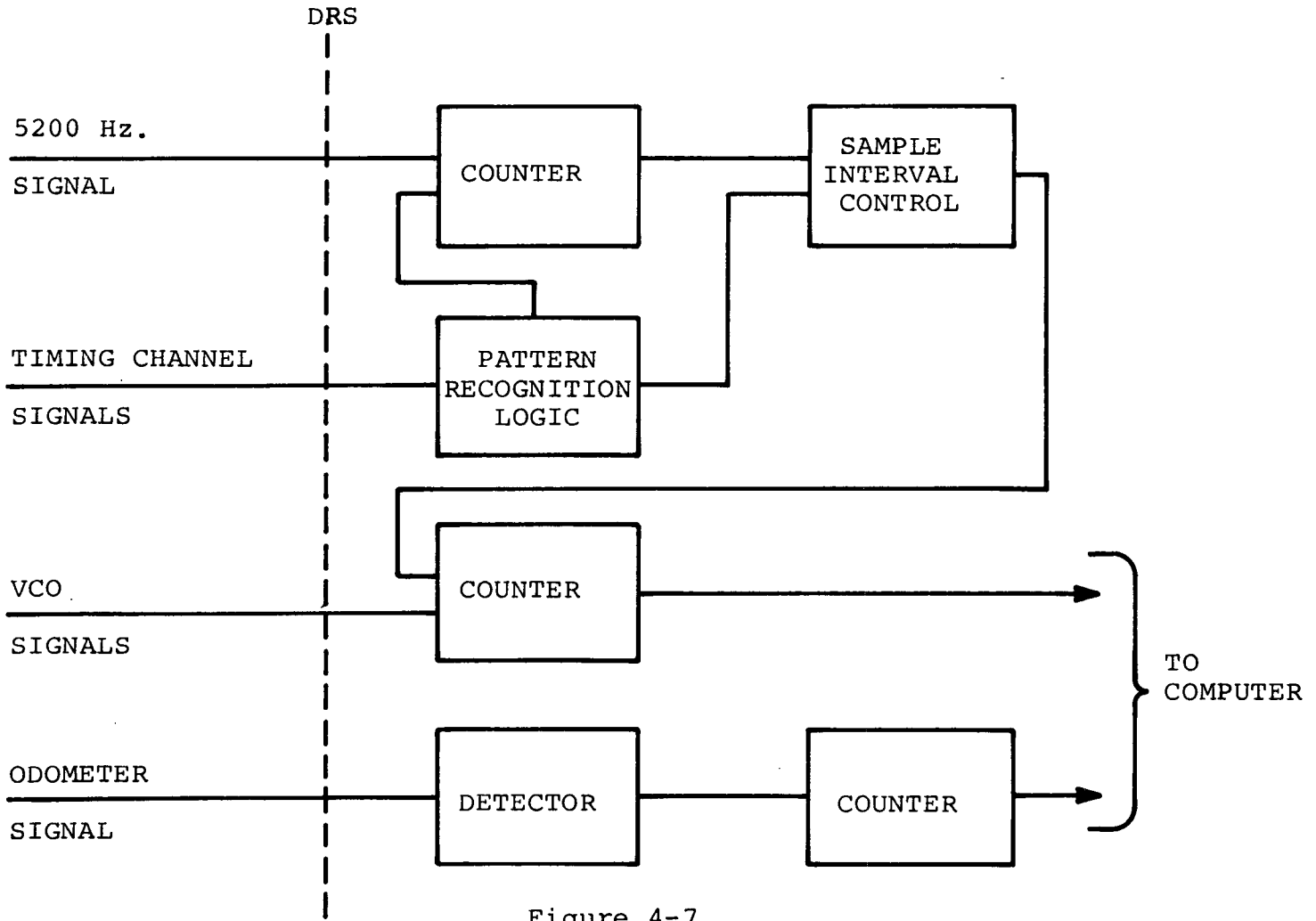

Figure 4-7

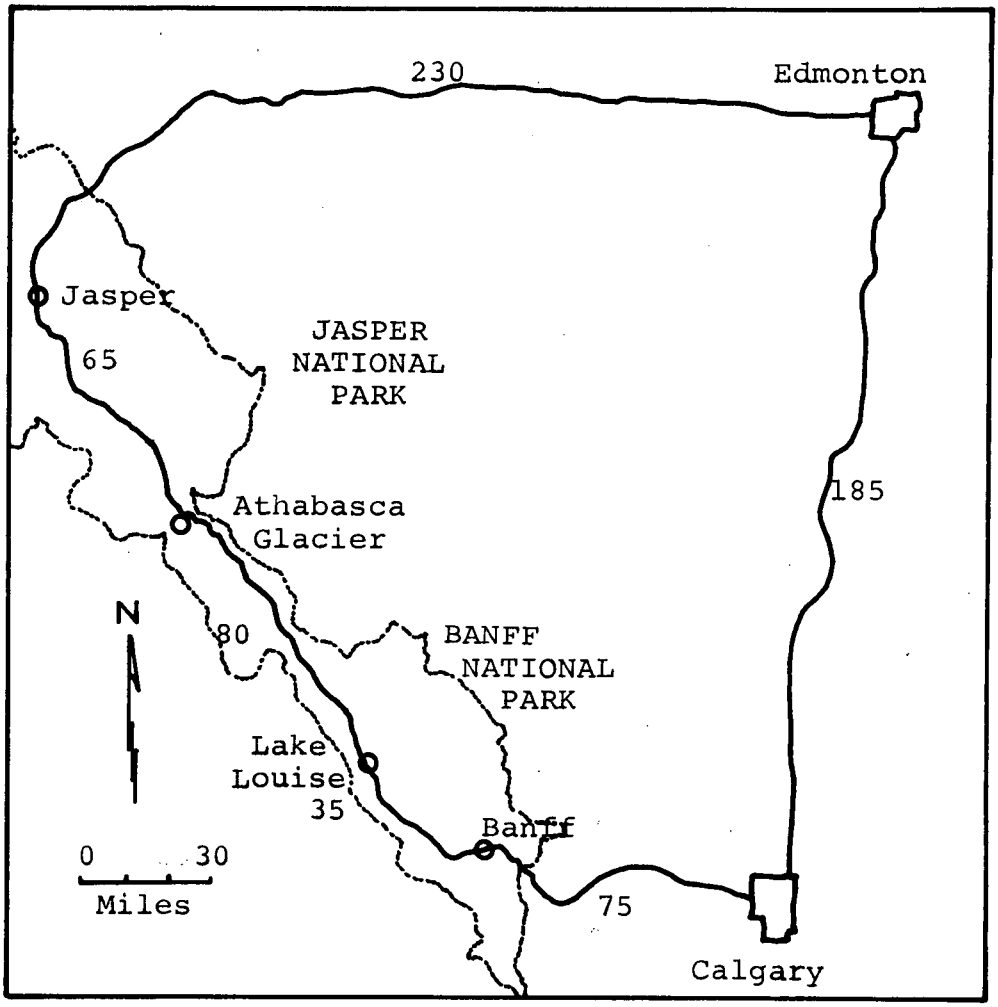

Athabasca Glacier Location Map

Highway distance in miles

Figure 4-8

trailers at the Jasper National Park Highway Maintenance Camp at Tangle Creek, five miles west of the glacier.

The Athabasca Glacier is a tourist attraction during the summer months and snowmobile tours are conducted over the surface of the glacier. A paved road extends from the main highway to the Snowmobile Tours concession located on the eastern lateral moraine of the glacier approximately one mile from the toe. As the Athabasca Glacier has receded in the past 50 years, large lateral moraines have been left in its wake, and to gain access to the glacier the snowmobile tours concession has constructed and maintained a dirt road down the lateral moraine to the glacier surface. This road is steep but is passable by all-terrain type vehicles.

4.3.2 Description of the Athabasca Glacier

The Athabasca Glacier is a valley glacier which flows northwest from the Columbia Icefields, a 100 square mile body of ice. The glacier is situated between Mt. Athabasca and Mt. Andromeda in the east and Mt. Snow Dome in the west. The headwall of the Athabasca Glacier, where the glacier juts out from the Columbia Icefield, is distinguished by three large icefalls. Near the toe or terminus, the glacier becomes extensively crevassed as the downward slope changes from approximately 5° to approximately 40°. Between these topological extremes, the downward south to north slope ranges 3 to 5° for a distance of approximately two miles. In this region of minimal slope, the glacier surface during the summer

is marred by crevasses of the order of meters across and tens of meters in depth, hillocks up to four meters high, moulins up to ten meters across, and an extensive number of water drainage channels. The width of the glacier between the lateral moraines is approximately 600 to 700 meters and the shape of the glacier valley is approximately parabolic. The measured depths of the ice range from approximately 50 meters near the toe to approximately 300 meters near the headwall. A depth contour map of the Athabasca Glacier, with the test sites used in this field trial, is illustrated in Figure 4-9. The altitude of the glacier is approximately 7000 feet above sea level.

Despite the roughness of the glacier surface, most of the scheduled tests for the summer 1971 field trials were conducted with no difficulty. However, the large tracked vehicle, used for obtaining traverse data, proved to be too unstable for straight-line traverses across the glacier. A smaller all-terrain, four-wheel drive, vehicle, trade name Coot, was rented as a logistics and personnel transport, and proved capable of traversing, without difficulty, any part of the glacier of interest to test personnel. In future field tests, a smaller tracked vehicle, the Cushman Trackster, which is about the same size as the Coot, will be used for obtaining traverse data.

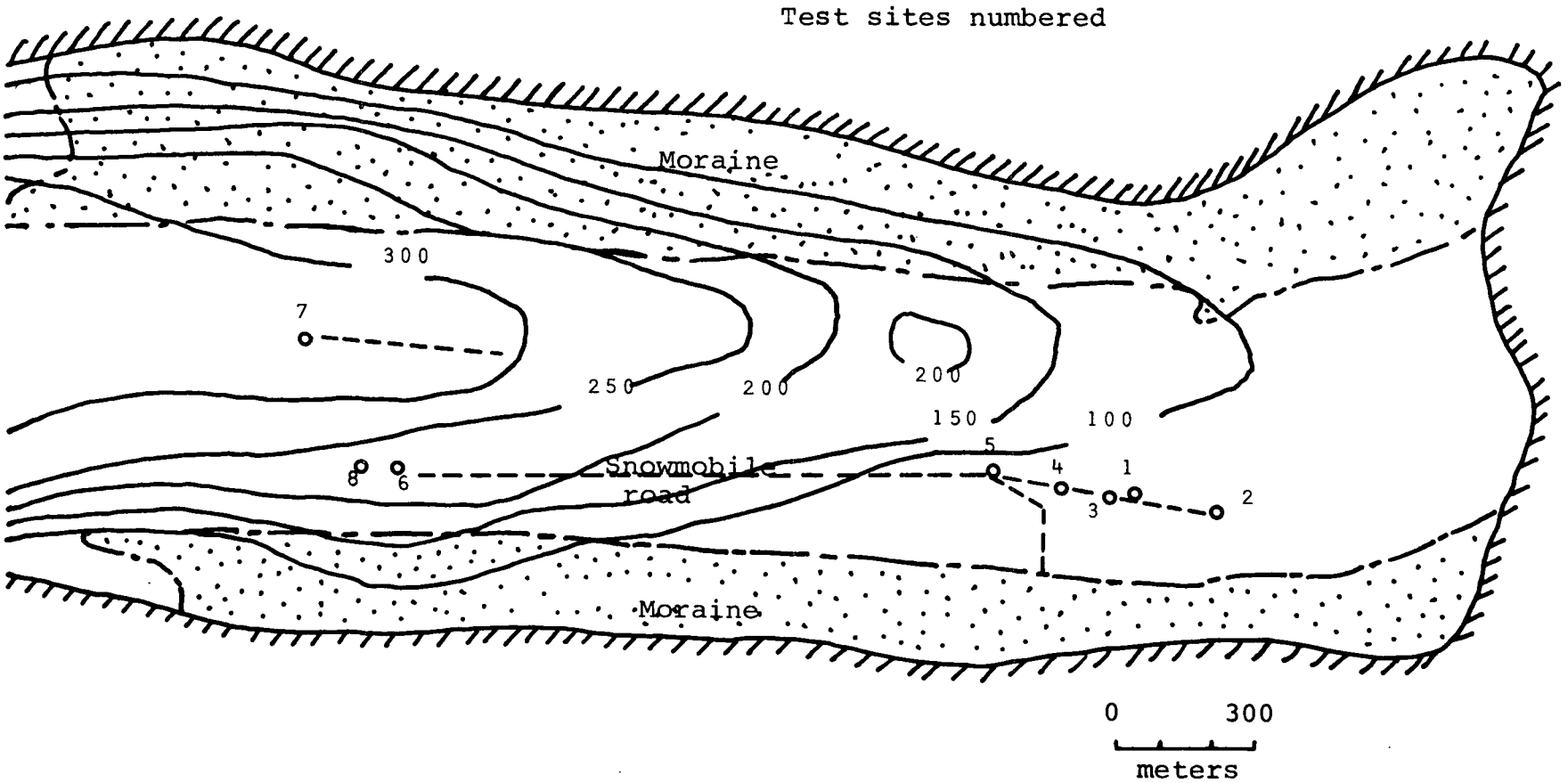

Figure 4-9: Depth contour map of the Athabasca Glacier, indicating the location of SEP traverse sites, summer 1971.
Depth contours are in meters, and are reconstructed from drilling and seismic studies.

Chapter 5

Field Test Measurements

5.0 Introduction

During the summer of 1971 more than eighty tests were conducted at eight test sites on the Athabasca Glacier. The two categories of tests conducted on the glacier were antenna measurements and measurements of received field strengths. The antenna tests included the following:

1. Current distribution measurements on the transmitting antennas deployed on the surface of the glacier;
2. Transmitting antenna driving point impedance measurements;
3. Measurements of the effective dielectric constant as seen by the transmitting antenna;
4. Receiving antenna circular calibration patterns.

Received field strengths were measured during linear and circular traverses of the glacier. The linear traverse tests were measurements of the induced magnetic field components near the air-ice interface as functions of the transmitter and receiver separation and the bearing measured with respect to the line of the transmitting antenna. An illustration of a linear traverse is shown in Figure (5-1). Circular traverse tests were measurements of the magnetic fields as the receiving equipment was conveyed in a constant

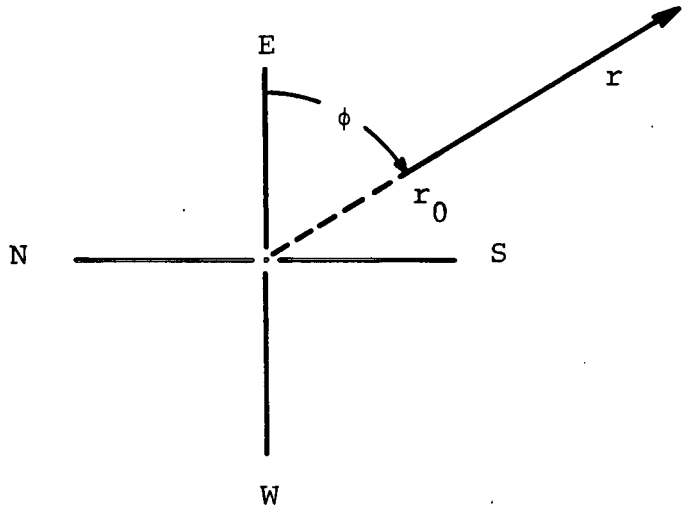

r_0 is the starting point of the traverse.

$r - r_o$ is the distance traveled in a straight line.

ϕ is the bearing of the traverse line relative to the linear extent of the E-W transmitting antenna.

STRAIGHT LINE TRAVERSES

Figure 5-1

radius circle around the transmitting antenna.. An illustration of a circular traverse is shown in Figure (5-2). In the following sections of this chapter, the antenna measurements and traverse measurements as related to the characteristics of the antennas are described and evaluated.

5.1 Antenna Test Results

5.1.1 Purpose of Tests

Antenna tests were conducted on the Athabasca Glacier to provide data for an evaluation of the transmitting antenna design and a calibration of the receiving antennas. The transmitting antennas were designed to have a real impedance for a specific subsurface dielectric constant with the antenna wire roughly conforming to the irregularities of the glacier surface. The current distribution measurements and the driving point impedance measurements were conducted to establish the validity of this design. The dielectric constant measurements were conducted to provide a design center for the calculations of the trap and suppressor locations on the antenna wire. The receiving antenna calibration patterns were measured to determine the effect of the tracked vehicle on the received signals.

5.1.2 Comparison of Actual and Theoretical Models of the Transmitting Antenna

Before evaluating the current distribution and driving point impedance measurements of the multi-frequency HED antenna over the glacier surface, the characteristics of the theoretical antenna model are compared with those of the

CIRCULAR TRAVERSE

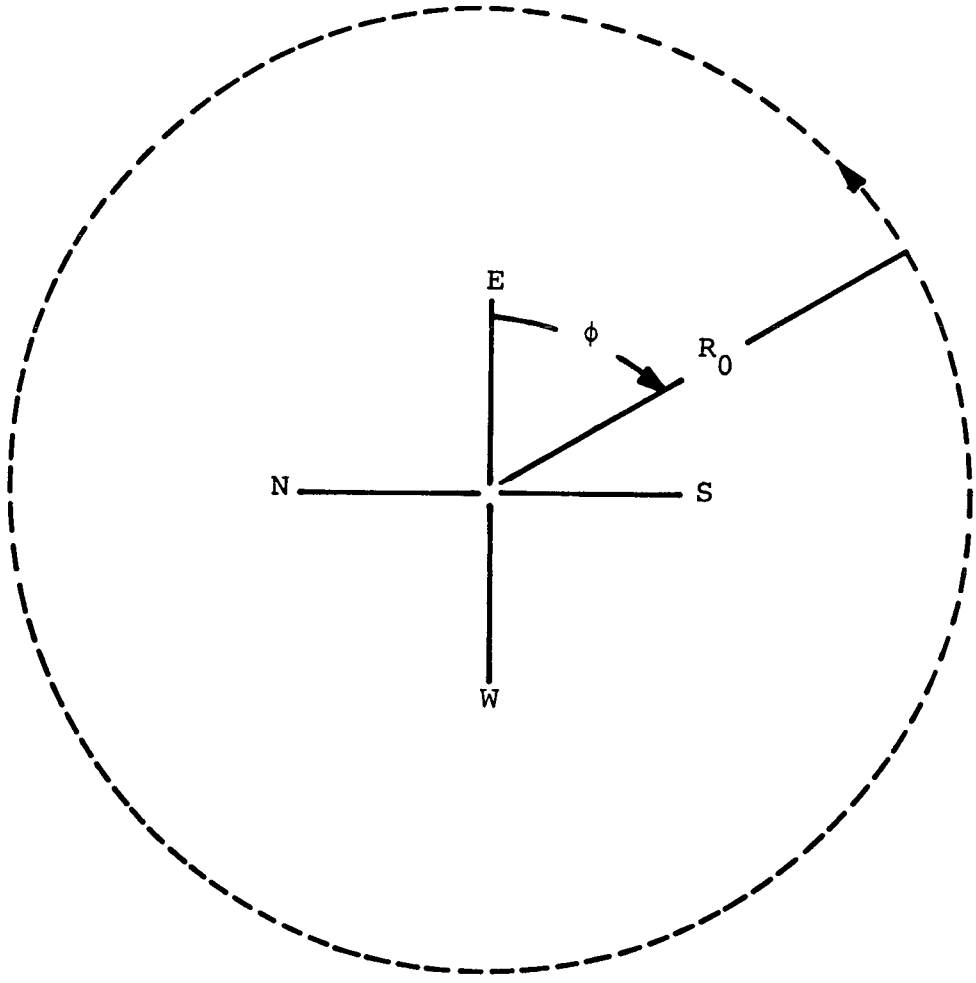

Figure 5-2

actual multi-frequency HED antenna.

To obtain the theoretical array factors for the transmitting antenna described in Chapter 3 and the Appendices, the following simplyifing assumptions were used:

1. The antenna was a half wavelength HED;
2. The antenna wire was a perfect conductor;
3. The transmitting source was an ideal delta function generator;
4. The entire antenna was situated exactly at the interface between two dielectrics;
5. The coefficients a,b,c and d in equation (3-4) were functions only of the ratio of wire length to diameter and the subsurface loss tangent.

The multi-frequency antenna however, were characterized by the following traits:

1. The antenna was effectively less than half wavelength at each experiment frequency;
2. The antenna wire was copper which has a finite conductivity;
3. The transmitter was a finite source with an output impedance of approximately 85 ohms;
4. The antenna wire was draped over the hummocky glacier surface such that over most of its length the antenna wire conformed with the surface features. However, much of the antenna was either in water or suspended a few inches off the ice;

5. The resonant circuit traps and suppressors, interspersed along the antenna length, were major factors in the impedance of the antenna.

Since the multi-frequency antenna was effectively less than a half wavelength, the imaginary part of the measured driving point impedance was capactive whereas the reactance of the theoretical half wavelength antenna model was inductive. In addition, the effects of the impedances of the traps and suppressors and the non-uniform height of the antenna wire off the ice surface were to further complicate the measurement of the antenna impedance. Therefore, a direct comparison of the reactive terms is unrealistic. However, the following general traits can be attributed to the current distribution for both the theoretical antenna model and actual antenna:

1. As the loss tangent of the subsurface is increased, the phase variation of the current with position on the antenna is increased;
2. The phase of the current distribution consists of a constant term plus a position dependent term. If the constant term is near zero, the effect of the position dependent term on the field solutions will be negligible, also.

Both of these observations can be deduced by noting that the general form of equation (3-6) is valid for the multi-frequency HED antenna although the coefficients a,b,c and d must be re-calculated for the shorter lengths of the multi-frequency antenna, for the average height of the antenna above the

glacier surface, and for the effects of the traps, suppressors and source impedances. For a known average height, the terms K_{eff} and $K_{\varepsilon_{eff}}$ in equation (3-6) can be adjusted using curves of effective dielectric constant versus height compiled by Raytheon personnel. In addition, for antenna lengths less than half-wavelengths, equation (3-6) should be written as:

$$\frac{I_x}{V_o\sqrt{K_{\varepsilon_{eff}}}} \simeq a' \frac{\sin K_{eff}\left(\frac{L}{2} - |x|\right)}{\sin K_{eff}\frac{L}{2}} + b\frac{\sin K_{eff}|x|}{\sin K_{eff}\frac{L}{2}}$$

$$+ jc\frac{\sin K_{eff}\left(\frac{L}{2} - |x|\right)}{\sin K_{eff}\frac{L}{2}} + jd\frac{\sin K_{eff}|x|}{\sin K_{eff}\frac{L}{2}} \qquad (5\text{-}1)$$

The array factors for the current distribution represented by equation (3-6) derived in Appendix A-3 can be written in the form:

$$M_i^{\xi} = \frac{I_1}{\sqrt{I_1^2+I_2^2}} e^{j\psi_1} M_i - \frac{I_2}{\sqrt{I_1^2+I_2^2}} e^{j\psi_2}\left(N_i + O_i\right) \qquad (5\text{-}2)$$

5.1.3 Current Distribution and Impedance Measurements

The current distribution curves in Figures (3-4) - (3-9) were obtained by the use of a measurement technique

devised by Raytheon personnel. A measure of current amplitude at discrete points along the antenna length was obtained from the output signal of a current probe placed around the antenna wire. Two difficulties associated with this measurement were that the antenna wire must be elevated off the ice to attach the current probe, thereby perturbing the current level in the vicinity of the probe and that the current levels measured near traps and suppressors were distorted by the high voltage levels associated with such resonant circuits. Despite these difficulties, the current distribution measurements obtained on the glacier were reasonable approximations to cosinusoidal distributions as indicated in Chapter 3. With reference to Figures (3-4) through (3-9), the current distributions are seen to be spatially continuous, except near traps and suppressors, and to have nearly zero amplitude at quarter wavelength distances from the antenna phase center. The current level is not zero at the quarter wavelength distances because the traps placed at those positions do not have infinite impedances.

The driving point impedance measurements were obtained by the measurement of the voltage standing wave ratio (VSWR) at the input terminals of the transmitting antennas. A representative sample of the results of these impedance measurements is listed below in Table 5-1.

Table 5-1

Driving Point Impedance Measurements on SEP Transmitting Antenna

Frequency (Mhz)	Impedance (Ohms)	Phase (Degrees)
1	121-j11	5.2°
2	140-j12	4.9
4	106-j65	31.5
8	90-j27	16.7
16	76-j70	42.6
32	58-j135	76.8

From Table 5-1, the largest reactive impedance terms are seen to have occurred at the highest frequencies of 16 and 32 MHz. This trait is consistent in similar measurements of the driving point impedance. In addition, the impedance of the antenna varied diurnally due to changes in the surface dielectric constant which were due to temperature variations and consequent changes in the extent of melt water on the glacier surface. (Note: The dielectric constant of water is 81, whereas the dielectric constant of ice is 3.2, and small changes in the average percentage of water to ice at the surface will result in appreciable changes in the dielectric constant.)

5.1.4 Dielectric Constant Measurements

Dielectric constant measurements were conducted on the glacier to provide an accurate measure of dielectric constant to be used for the calculation of antenna wire lengths between traps and suppressors. The test procedure was: an

antenna of approximately half wavelength was deployed at the surface of the ice and the length of the antenna was adjusted such that the VSWR between the transmitter and the transmitting antenna was minimized for maximum power transfer. The dielectric constant of the medium at each of the SEP experiment frequencies was then determined from the resulting antenna length using the equation:

$$K_{\epsilon_{ice}} = \frac{1}{2}\left(\frac{\lambda_o}{L}\right)^2 - 1 \qquad (5\text{-}3)$$

which is obtained by combining equations (3-1) and (3-5) for

$$L = \frac{\lambda_{eff}}{2} \qquad (5\text{-}4)$$

The apparent average dielectric constant of the ice just below the glacier surface was 3.94 which is a higher value than the commonly published dielectric constant for a ice of 3.2. The larger value of 3.94 was probably due to the large amount of water (dielectric constant of 81 on the glacier surface during the summer months.)

5.1.5 Receiving Antenna Calibration

The SEP experiment receiving antennas illustrated in Figure 5-3 are three orthogonal loop antennas, which are designed to measure three orthogonal magnetic field components. These antennas are designed to be electrically decoupled such that each loop is sensitive to the magnetic fields perpendicular

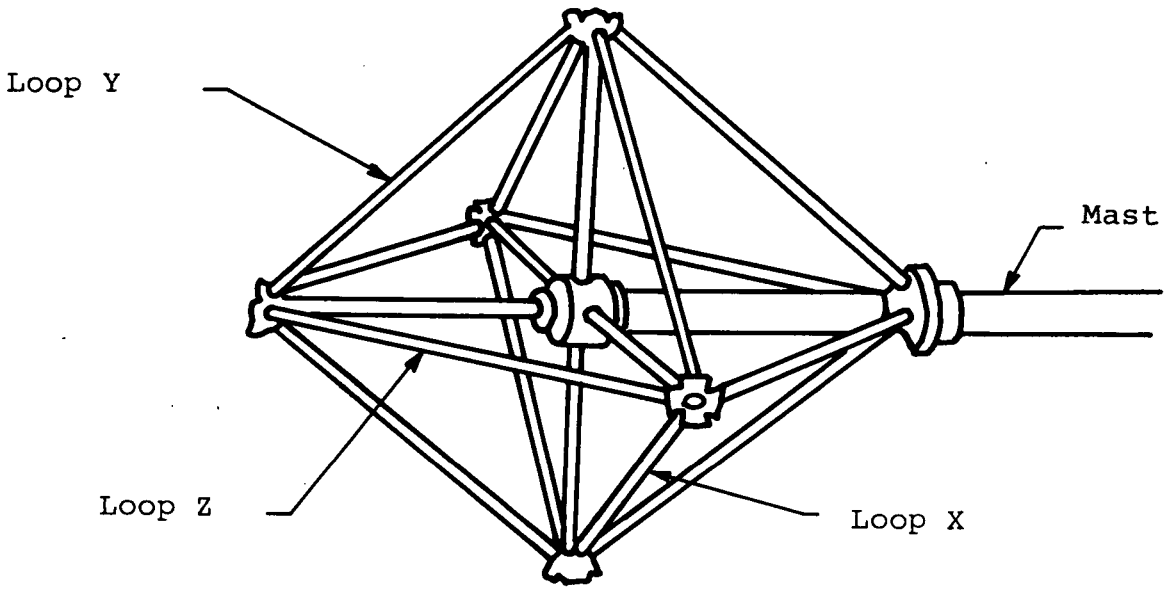

TRI-LOOP RECEIVING ANTENNA

Figure 5-3

to the plane of the loop and is effectively isolated from fields parallel to the plane of the loop. The degree of decoupling between loops is illustrated in Table 5-2 in which the minimum decoupling is shown to be -21.7 dB at 32 MHz, i.e. for a magnetic field perpendicular to the plane of one of the three loops, the error signals measured at the terminals of either of the other loops is at least 21.7 dB below the level of the directly energized loop. In addition, the free space radiation or reception pattern for each loop is that of a free space magnetic dipole, i.e. for rotation about the plane of the loop, the radiation pattern can be described as a figure eight with maximum sensitivity perpendicular to the plane of the loop and minimum sensitivity parallel to the plane of the loop, and for rotation in the plane of the loop, the radiation pattern can be described as a constant.

In the SEP field trials, the loop antennas were attached to the rear of the tracked vehicle. Due to the proximity of such a large conducting body, the loop antenna radiation patterns were distorted from their free space values. Therefore, receiving antenna calibration measurements were conducted on the glacier to provide a measure of the effects of the direction of the tracked vehicle on the measured field strengths.

To determine the effect of the tracked vehicle on the received field strengths, the vehicle, as illustrated in Figure (5-4), was positioned on a flat area of the glacier approximately 100 meters from the transmitter at a bearing of

DECOUPLING BETWEEN ELEMENTS OF TRI-LOOP RECEIVING ANTENNA (LOOPS A,B, AND C REFER TO FIGURE 5-3 FOR ORIENTATION GEOMETRY).

f = 32 MHZ:

A(peak)	0 dB	B(peak)	0 dB	C(peak)	0 dB
B	-28 dB	A	-30 dB	A	-33 dB
C	-23 dB	C	-28 dB	B	-27 dB

f = 16 MHz:

A(peak	0 dB	B(peak)	0 dB	C(peak)	0 dB
B	-26.7 dB	A	-30.8 dB		
C	-21.7 dB	C	-22.3 dB		

f = 8 MHz:

A(peak)	0 dB	B(peak)	0 dB	C(peak)	0 dB
B	-27.7 dB	A	-30.8 dB		
C	-45.3 dB	C	-22.3 dB		

f = 4 MHz:

A(peak)	0 dB	B(peak)	0 dB	C(peak)	0 dB
B	-28.7 dB	A	-32.5 dB		
C	-41.5 dB	C	-32.5 dB		

f = 2 MHz:

A(peak)	0 dB	B(peak)	0 dB	C(peak)	0 dB
B	-27.1 dB	A	-28.4 dB		
C	-37.4 dB	C	-30.2 dB		

f = 1 MHz:

A(peak)	0 dB	B(peak)	0 dB	C(peak)	0 dB
B	-25.2 dB	A	-27.3 dB	A	-25.3 dB
C	-24.7 dB	C	-26.8 dB	B	-24.0 dB

Table 5-2

RECEIVING ANTENNA CALIBRATION TEST CONFIGURATION

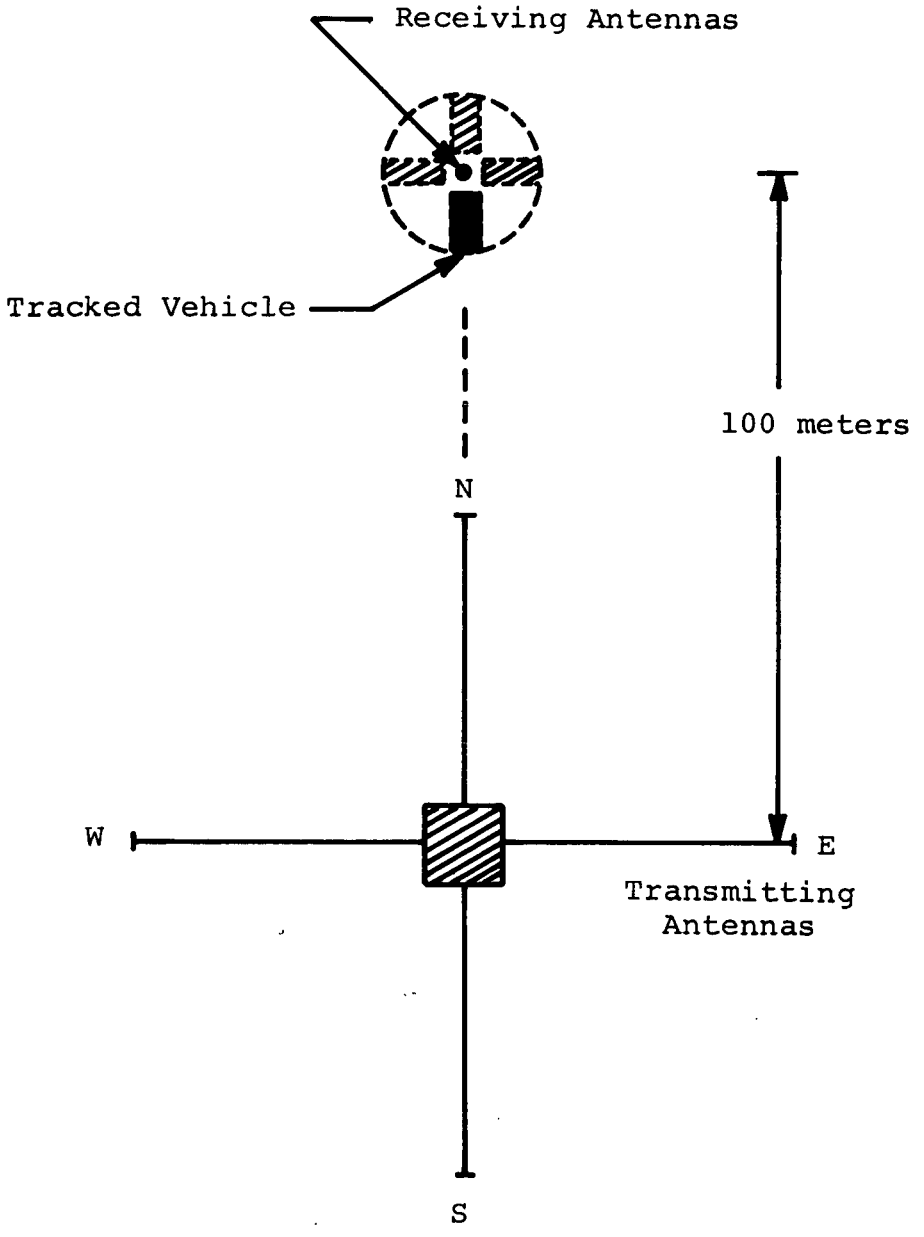

Figure 5-4

90° with respect to the line of the E-W antenna, and rotated through 360° in steps of 90° such that the center of the receiving antenna structure was maintained in its initial position. The heading of the vehicle in its initial position was due north from the transmitter. The magnetic fields induced at the three receiving antennas by each transmitting antenna were measured at the four vehicle headings. The data obtained by these measurements is listed in Tables 5-3 and 5-4.

Along the bearing of the test vehicle, the major field component induced by the N-S (endire) transmitting antenna was the TM component, $H\phi$. The TE components $H\rho$ and Hz should have been zero in the far field, if no energy were scattered in the subsurface medium and if the receiving antennas were completely isolated. In turn, the major fields induced by the E-W antenna were the TE components $H\rho$ and $H\phi$ while the TM component $H\phi$ should have been zero in the far field.

However, the range of the vehicle during the receiver calibration tests was only 100 meters, the receiving antennas were shown not to be completely isolated, and RF energy was scattered in the subsurface medium especially at the three highest frequencies.[14] Therefore, measureable field strengths were induced in all three receiving antennas at all six experiment frequencies by both transmitting antennas. The difficulty in maintaining the center of the receiving antenna structure in its initial calibration position was manifested

TABLE 5-3

RECEIVING ANTENNA CALIBRATION DATA -NS ANTENNA POWERED

f(MHz)	Vehicle Compass Direction	Magnetic Field Components (dB)		
		H_ρ	H_ϕ	H_z
1	N	32	42	24
1	W	8	46	24
1	E	2	46	28
1	S	34	48	28
2	N	35	48	27
2	W	24	51	28
2	E	18	51	24
2	S	37	48	26
4	N	32	53	28
4	W	34	56	32
4	E	35	56	28
4	S	38	53	32
8	N	*	64	64
8	W	*	72	65
8	E	64	60	68
8	S	70	70	66
16	N	54	59	62
16	W	61	62	66
16	E	53	58	51
16	S	60	54	63
32	N	66	53	63
32	W	54	51	64
32	E	68	62	66
32	S	59	69	62

*The receiving antenna is near an interference null in the field component.

TABLE 5-4

RECEIVING ANTENNA CALIBRATION DATA - EW ANTENNA POWERED

f(MHz)	Vehicle Compass Direction	Magnetic Field Components (dB)		
		Hρ	Hϕ	Hz
1	N	44	12	44
1	W	40	11	45
1	E	40	20	45
1	S	43	16	45
2	N	46	16	40
2	W	42	18	41
2	E	42	20	41
2	S	46	16	42
4	N	44	30	48
4	W	40	32	49
4	E	40	30	48
4	S	43	30	49
8	N	58	60	62
8	W	65	70	60
8	E	56	60	60
8	S	68	68	*
16	N	68	70	64
16	W	*	69	63
16	E	67	66	66
16	S	58	65	59
32	N	54	55	63
32	W	60	61	58
32	E	54	56	59
32	S	58	58	50

*The receiving antenna is near an interference null in the field component.

at the higher frequencies (16 and 32 MHz) where perturbations in the received fields of up to 5 dB were noted for positioning errors of less than 0.3 meters. In addition, field measurements near interference fringes, where variations in the field strength are of the order of tens of decibels for range changes of the order of meters, were neglected.

One aspect of the data in Table 5-3 was that when the vehicle was rotated $\pm 90°$ from its initial position, significant variations in the measured H_ρ field occurred at the two lowest experiment frequencies such that at 1 MHz, the H_ρ component induced by the N-S antenna was effectively nullified, and at 2 MHz, the H_ρ component was reduced by as much as 19 dB. In both Tables 5-3 and 5-4, the field strengths were shown to have been approximately the same whether the vehicle was driven toward or away from the transmitter and since all the test linear traverses were conducted with the vehicle headed either toward or away from the transmitter, no modification of the data was required. However, when the SEP experiment is conducted on the lunar surface, the astronaut will not be constrained to straight line traverses, and an accurate receiving antenna calibration will be necessary. A receiving antenna calibration is planned with the antenna mounted on a mockup of the lunar rover.

5.2 Traverse Measurements

Most of the tests conducted on the Athabasca Glacier in the summer of 1971 involved linear traverses of the

instrumented vehicle across the glacier during which time the magnetic fields induced in the receiving antennas were recorded. The main reason for these traverse measurements was to collect radio interferometry data from a known topography in order to develop analytical techniques for the study of interferometry data to be gathered on the lunar surface by the Apollo 17 crew. A preliminary study of this glacier data has been done by Rossiter, Watts, and Strangway.[14] Additional traverse measurements were conducted to determine certain characteristics of the transmitting antennas: the multi-frequency antenna designed by Raytheon personnel, a simple half wave antenna, and an "infinitesimal" dipole antenna (the actual antenna size was nearly 1/7 of a free-space wavelength). The purposes of conducting these tests were to verify the validity of the approximation of the multi-frequency antenna as a half wave antenna and to verify the assumption that the infinitesimal dipole field solutions could be used to approximate the field solutions of a finite-length antenna.

The linear traverse measurements were conducted at a bearing angle of 90° (broadside) with respect to the aforementioned transmitting antennas. The transmitter was used in the continuous wave mode and only the Hz field component was measured. The traverse measurements of the received Hz components induced by each of these antennas are illustrated in Figure 5-5 in which the received field strengths are

shown to have the same spatial nature, i.e. peaks and troughs occurring at roughly the same receiver - transmitter separation. An exception to this similarity in the data is the existence of a trough in two of the curves, A and B, in Figure 5-5 at a transmitter-receiver separation of approximately 230 meters. The data in runs A and B was obtained during a traverse toward the transmitter whereas the data for run C was obtained during a traverse away from the transmitter. After further investigation of this trough at a range of 230 meters, the trough was found to have been masked by the vehicle when the vehicle was headed away from the receiver and was not a characteristic peculiar to the longer transmitting antennas used in runs A and B. The trough in runs A and B at a range of 230 meters may have been due to interference from energy back-scattered from a subsurface cave or stream such that the reception of the interfering energy was dependent upon the spatial relationships between the receiving antennas, the vehicle, and the subsurface anomaly. The above phenomenon has not been observed in data runs to and from the transmitter at the other seven test sites.

FIELD STRENGTH PROFILES

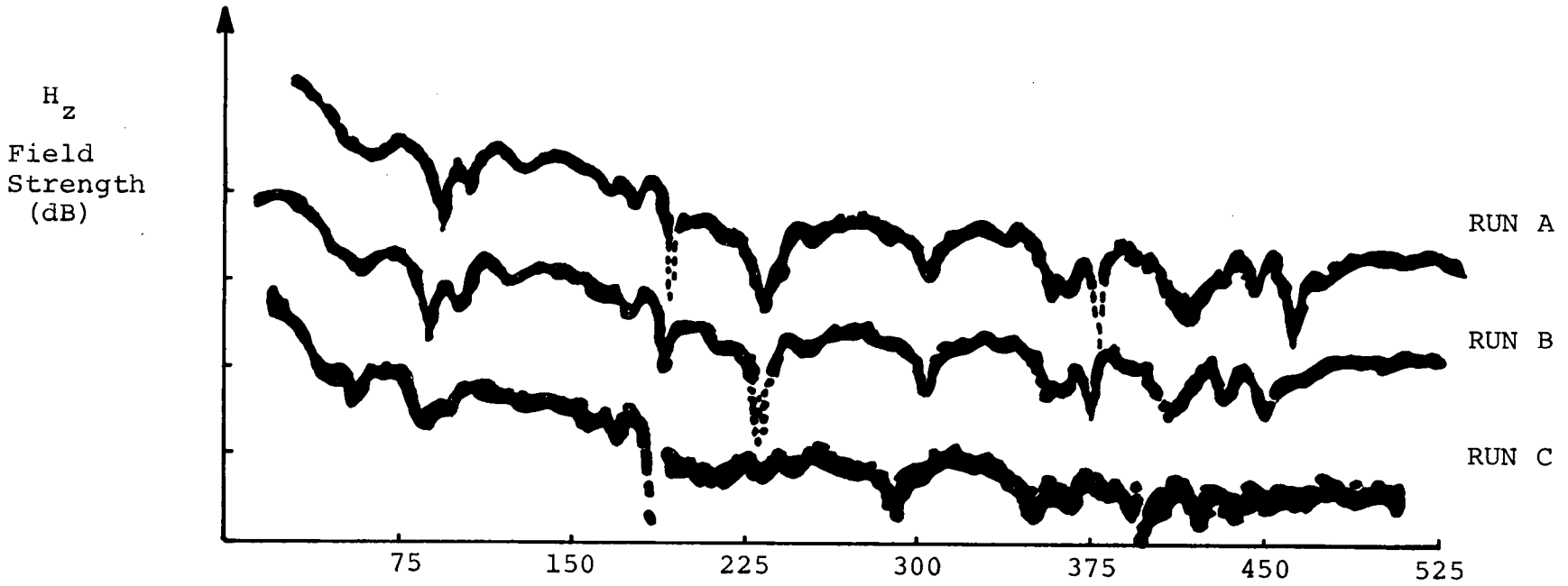

RUN A - Multi-frequency transmitting antenna
RUN B - Half wavelength transmitting antenna
RUN C - "Infinitesimal" transmitting antenna

Figure 5-5

Chapter 6

Summary

6.0 Description of the Field Solutions

The field solutions for half wavelength dipoles over stratified media have been derived in Chapters 2 and 3. In particular, the surface fields and the surface field patterns for half wavelength dipoles have been derived because in most practical applications the measurement of the fields is constrained to the surface over which the antenna is deployed. The radiation patterns have been derived to determine the gain and directionality of subsurface radiation from the dipole antennas, so that the general nature of surface fields reflected from subsurface layers can be predicted.

6.1 Salient Features of the Field Solutions

The solutions for the fields induced by a half wavelength dipole have been shown to be similar to the solutions for the fields induced by an infinitesimal dipole. However, the differences between these solutions are significant in terms of the practical application of the radio interferometry technique. For instance, near the half wavelength dipole, the existence of large broadside TM fields (zero for the infinitesimal dipole) can be explained in terms of the cross-coupling between the radial TE and the tangential TM fields and, far from the half wavelength dipole antenna, the bearing angle dependence of the magnetic surface fields can be explained in terms of the application of the array factor to the infinitesimal dipole

field solutions.

6.2 Areas for Further Theoretical Study

The field solutions included in this thesis can be used with a more accurate current distribution measurement to provide a more detailed field formulation. Since future applications of the radio interferometry technique may involve the use of transmitting antennas other than half wavelength dipoles, future studies of the source antennas should be carried out with the goal of tailoring the antenna design to a desired radiation pattern.

6.3 Data from the Athabasca Field Trials

In Chapters 4 and 5, the instrumentation used on the summer 1971 SEP field trials and field trial measurements related to the operational characteristics of the transmitting and receiving antennas are described and evaluated. The current distribution for the SEP multi-frequency transmitting antenna have been shown to be approximately cosinusoidal, and the receiving antenna patterns have been shown to have been affected by the presence of the instrumented vehicle.

6.4 Recommendations for Future Field Trials

The current distribution measurements as described in Chapter 5 should include the measurement of the phase as well as the amplitude of the current at a minimum of ten points per quarter wavelength leg of the antenna to provide an accurate representation of the non-cosinusoidal terms in the antenna current distribution. A more detailed receiving antenna calibration measurement should be devised and implemented at

the beginning of each field trial to improve the quality of the traverse data.

6.5 General Comments

Many interesting and challenging analytical problems associated with the application of the radio frequency interferometry technique have been solved but the analysis is not complete. Analytical studies of the subsurface scattering of electromagnetic energy and the effects of a more complicated topographic model than the simple horizontal layering model should be investigated.

Although further study will be necessary, hopefully, the material in this thesis will be useful in the development of the radio frequency interferometry technique as a practical geophysical tool for sounding low conductivity media.

APPENDIX A-1 SOLUTION OF BOUNDARY CONDITIONS

For a transverse current at the z = 0 interface the current density $\underline{J}$ is described by the equation

(A1-1)

Figure A1-1

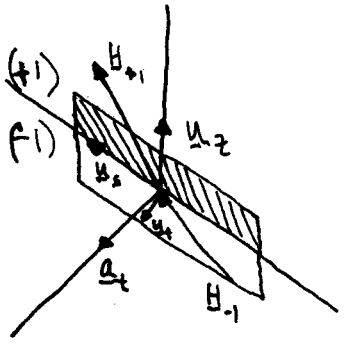

For a current source in the form of a delta Dirac function as in Figure A1-1.

$$\left(\underline{H}_{+1} - \underline{H}_{-1}\right) \cdot \underline{u}_s \, e^{-j\underline{k}_t \cdot \underline{r}} = \underline{J} \cdot \underline{u}_t \qquad \text{(A1-2)}$$

using the vector identity

$$\underline{A} \times \left(\underline{B} \times \underline{C}\right) = \left(\underline{A} \cdot \underline{C}\right)\underline{B} - \left(\underline{A} \cdot \underline{B}\right)\underline{C} \qquad \text{(A1-3)}$$

$$\left[\underline{H}_{+1} - \underline{H}_{-1}\right] \underline{u}_t = \left\{\left(\underline{H}_{+1} - \underline{H}_{-1}\right) \times \left(\underline{u}_t \times \underline{u}_s\right) + \left(\underline{H}_{+1} - \underline{H}_{-1}\right) \cdot \underline{u}_t \right\} \underline{u}_s \tag{A1-4}$$

and

$$\underline{J} = \underline{u}_z \times \left(\underline{H}_{+1} - \underline{H}_{-1}\right) e^{j\underline{k}_t \cdot \underline{r}} = \underline{a}_t \, e^{j\underline{k}_t \cdot \underline{r}} \tag{A1-5}$$

$$\text{where } \underline{U}_z = \underline{U}_s \times \underline{U}_t \tag{A1-6}$$

$$\text{and} \qquad \underline{U}_z \times \left(\underline{H}_{+1} - \underline{H}_{-1}\right) = \underline{a}_t \tag{A1-7}$$

Again using the vector identity in equation (A1-3) and performing a cross product vector manipulation

$$\underline{u}_z \times \underline{a}_t = \underline{u}_z \times \left[\underline{u}_z \times \left(\underline{H}_{+1} - \underline{H}_{-1}\right)\right] \tag{A1-8}$$

$$= \underline{u}_z \cdot \left(\underline{H}_{+1} - \underline{H}_{-1}\right) \underline{u}_z - \left(\underline{u}_z \cdot \underline{u}_z\right)\left(\underline{H}_{+1} - \underline{H}_{-1}\right) \tag{A1-9}$$

$$= \underline{u}_z \cdot \left(\underline{H}_{+1} - \underline{H}_{-1}\right) \underline{u}_z - \left(\underline{H}_{+1} - \underline{H}_{-1}\right) \tag{A1-10}$$

For the tangential components of $\underline{H}$

$$-\underline{u}_z \times \underline{a}_t = \left(\underline{H}_{+1} - \underline{H}_{-1}\right) = \left(\underline{H}_{+1,t} - \underline{H}_{-1,t}\right) \tag{A1-11}$$

APPENDIX A-2 CURRENT DISTRIBUTION FORMULATION

With reference to Figure 3-1 and the replacement of ($K_{\varepsilon_{eff}}$) for (ε_r), the current distribution[5] of a half wavelength dipole in a dissipative medium is represented by the equation:

$$\frac{I_x}{V_0\sqrt{K_{\varepsilon_{eff}}}} = \frac{j\,2\pi(1-\alpha/\beta)}{\zeta_0\,\psi_{V_2}}\left[W(\tfrac{1}{4})\cos K_{eff}\,x + \sin K_{eff}|x| - 1\right] \qquad \text{(A2-1)}$$

where

$$\zeta_0 = \sqrt{\frac{\mu_0}{\varepsilon_0}} = 120\pi \text{ ohms} \qquad \text{(A2-2)}$$

$$\alpha = \frac{\pi}{\lambda_0}\sqrt{K_{\varepsilon_{eff}}}\,\tan\delta, \text{ attenuation factor nepers/meter} \qquad \text{(A2-3)}$$

$$K_{eff} = \frac{2\pi}{\lambda_{eff}} = \sqrt{K_{\varepsilon_{eff}}}\,\frac{2\pi}{\lambda_0} \text{ phase factor (radians/meter)} \qquad \text{(A2-4)}$$

$$\lambda_0 = \text{free space wavelength (meters)} \qquad \text{(A2-5)}$$

X = distance along the antenna half length from the antenna phase center (meters) (A2-6)

$$W(\lambda/4) = \frac{\left(1 - J\frac{\pi}{2}\frac{\alpha}{\beta}\right)\left(\psi_{V_2} + \psi_S(\lambda/4)\right)}{\left(1 - J\frac{\pi}{2}\frac{\alpha}{\beta}\right)\psi_C(\lambda/4) - J\frac{\pi}{2}\frac{\alpha}{\beta}\psi_u}$$

$$\psi_u = 2\sinh^{-1}(h/a_0) - J0.633 - \alpha/\beta(1.571 + J0.571) \tag{A2-7}$$

$$\psi_{V_2} = 4\sinh^{-1}\left(\frac{h}{a_0}\right) - 2\sinh^{-1}\left(\frac{2h}{a_0}\right) - 1.747 - J0.384 \tag{A2-8}$$

$$\psi_C(\lambda/4) = 0.709 - J1.219 + J\frac{\pi}{2}\frac{\alpha}{\beta} \tag{A2-9}$$

$$\psi_S(\lambda/4) = 2\sinh^{-1}\left(\frac{2h}{a_0}\right) - 2\sinh^{-1}\left(\frac{h}{a_0}\right) - 1.219 - J0.709 + J\frac{\alpha}{\beta} \tag{A2-10}$$

(A2-11)

To obtain the current distribution calculations listed in Table 3-1, the following values of the parameters were used:

$$K_{\varepsilon_{eff}} = 2.15 \tag{A2-12}$$

$$\tan\delta = 0.3/f \quad f \text{ in MHz} \tag{A2-13}$$

$$a_0 = 3.22 \times 10^{-3} \text{ meters} \tag{A2-14}$$

and equation A2-1 was put in the form:

$$\frac{I_x}{V_0\sqrt{K_{\varepsilon_{eff}}}} = a\cos K_{eff}x + b\left(\sin K_{eff}|x| - 1\right)$$

$$+jc\cos K_{eff}x + jd\left(\sin K_{eff}|x| - 1\right)$$

(A2-15)

where a = Real Part $\left[\left(\frac{j2\pi(1-\alpha/\beta)}{\zeta_0\,\psi_{v_2}}\right)\left(W(1/4)\right)\right]$

c = Imaginary Part $\left[\left(\frac{j2\pi(1-\frac{\alpha}{\beta})}{\zeta_0\,\psi_{v_2}}\right)\left(W(1/4)\right)\right]$

b = Real Part $\left[\frac{j2\pi(1-\alpha/\beta)}{\zeta_0\,\psi_{v_2}}\right]$

d = Imaginary Part $\left[\frac{j2\pi(1-\alpha/\beta)}{\zeta_0\,\psi_{v_2}}\right]$

APPENDIX A-3 SURFACE FIELD ARRAY FACTOR

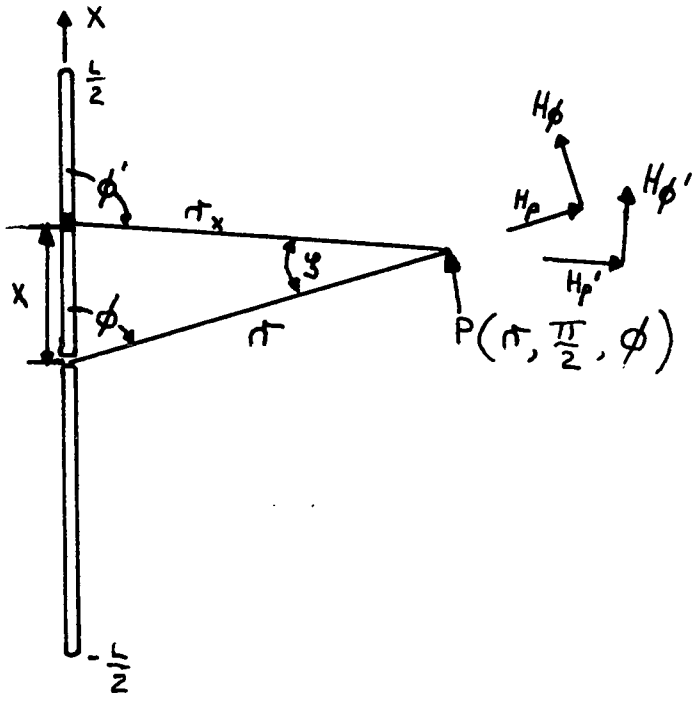

Figure A3-1

With reference to Figure A3-1, at a point $P(r,\frac{\pi}{2},\phi)$, the half-space surface field components H_ρ, and H_ϕ, due to radiation from an infinitesimal HED located at a distance x from the half wavelength HED antenna phase center, are represented by the equations[2]:

$$H_{\rho'}^{S} \cong -2a_t \sin\phi' \left\{ \frac{H_{-1}}{H_1 K} \frac{k_{c_1}}{r_x} G_1^{x} - \frac{H_1}{H_{-1}(-jK)} \frac{k_{c_{-1}}}{r_x} G_{-1}^{x} \right\} \tag{A3-1}$$

$$H_{\phi'} \cong -2a_t \cos\phi' \left\{ \frac{\epsilon_{-1}}{\epsilon_1 \mathbb{K}} \frac{k_{c_1}}{\pi_x} G_1^x - \frac{\epsilon_1}{\epsilon_{-1}(-\mathbb{K})} \frac{k_{c_{-1}}}{\pi_x} G_{-1}^x \right\}$$

(A3-2)

where $$G_i^x = \frac{e^{-jk_{c_i}\pi_x}}{4\pi\pi_x}$$

(A3-3)

In the coordinate system (r,ϕ), the surface field components $H^s_{\rho,i}$ and $H^s_{\phi,i}$ are related to the surface field components $H^{s'}_{\rho}$ and $H^{s'}_{\phi}$ by the equations:

$$H^s_{\rho,i} = H^s_{\rho'} \cos\zeta + H^s_{\phi'} \sin\zeta$$

(A3-4)

$$H^s_{\phi,i} = -H^s_{\rho'} \sin\zeta + H^s_{\phi'} \cos\zeta$$

(A3-5)

where $$\zeta = \phi' - \phi$$

(A3-6)

The terms $\sin\zeta$ and $\cos\zeta$ can be written in terms of r and ϕ with the resulting equations:

$$\sin\phi' = \frac{r}{r_x}\sin\phi \tag{A3-7}$$

$$\cos\phi' = \left(\frac{r_x^2 - r^2\sin^2\phi}{r_x^2}\right)^{\frac{1}{2}} \tag{A3-8}$$

Since r_x is represented in terms of r and ϕ in the equation:

$$r_x = \left(r^2 + x^2 - 2xr\cos\phi\right)^{\frac{1}{2}} \tag{A3-9}$$

Equations (A3-7) and (A3-8) can be written as:

$$\sin\phi' = \left(\frac{B}{D}\right)^{\frac{1}{2}} \tag{A3-10}$$

$$\cos\phi' = \left(\frac{A}{D}\right)^{\frac{1}{2}} \tag{A3-11}$$

where

$$A = r^2\cos^2\phi + x^2 - 2xr\cos\phi \tag{A3-12}$$

$$B = r^2\sin^2\phi \tag{A3-13}$$

$$D = r^2 + x^2 - 2xr\cos\phi \tag{A3-14}$$

From Equations (A3-4) and (A3-6) $\sin\zeta$ and $\cos\zeta$ can be written as:

$$\cos\zeta = \cos(\phi' - \phi) = \cos\phi'\cos\phi + \sin\phi'\sin\phi \tag{A3-15}$$

$$\sin\zeta = \sin(\phi' - \phi) = \sin\phi'\cos\phi - \cos\phi'\sin\phi \tag{A3-16}$$

and substituting Equations (A3-10) and (A3-11) for $\sin\phi'$ and $\cos\phi'$ in Equations (A3-15) and (A3-16) yields the relationships:

$$\cos\zeta = \left(\frac{A}{D}\right)^{\frac{1}{2}}\cos\phi + \left(\frac{B}{D}\right)^{\frac{1}{2}}\sin\phi \tag{A3-17}$$

$$\sin\zeta = \left(\frac{B}{D}\right)^{\frac{1}{2}}\cos\phi - \left(\frac{A}{D}\right)^{\frac{1}{2}}\sin\phi \tag{A3-18}$$

Noting that $H_\rho^{s'}$ and $H_\phi^{s'}$ can be put in the forms:

$$H_\rho^{s'} = a_t \sin\phi' L_\rho' \tag{A3-19}$$

and $$H_\phi^{s'} = a_t \cos\phi' L_\phi' \tag{A3-20}$$

where $$L_\rho' = -2\left\{\frac{M_{-1}}{M_1 K}\frac{K_{c_1}}{\pi_x} G_1^x - \frac{M_1}{M_{-1}(-jK)}\frac{K_{c_{-1}}}{\pi_x} G_{-1}^x\right\} \tag{A3-21}$$

$$\text{and } L_\phi^{\,1} = 2\left\{ \frac{\epsilon_{-1}}{\epsilon_1 K} \frac{k_{c_1}}{\pi_x} G_1^{\,x} - \frac{\epsilon_1}{\epsilon_{-1}(-jK)} \frac{k_{c_{-1}}}{\pi_x} G_{-1}^{\,x} \right\}$$

(A3-22)

the surface field components $H^s_{\rho,i}$ and $H^s_{\phi,i}$ become:

$$H^s_{\rho,i} = a_t \left\{ L_\rho' \left(\frac{B}{D}\right)^{\frac{1}{2}} \left[\left(\frac{A}{D}\right)^{\frac{1}{2}} \cos\phi + \left(\frac{B}{D}\right)^{\frac{1}{2}} \sin\phi \right] + L_\phi' \left(\frac{A}{D}\right)^{\frac{1}{2}} \left[\left(\frac{B}{D}\right)^{\frac{1}{2}} \cos\phi - \left(\frac{A}{D}\right)^{\frac{1}{2}} \sin\phi \right] \right\} \quad \text{(A3-23)}$$

$$H^s_{\phi,i} = a_t \left\{ L_\phi' \left(\frac{A}{D}\right)^{\frac{1}{2}} \left[\left(\frac{A}{D}\right)^{\frac{1}{2}} \cos\phi + \left(\frac{B}{D}\right)^{\frac{1}{2}} \sin\phi \right] - L_\rho' \left(\frac{B}{D}\right)^{\frac{1}{2}} \left[\left(\frac{B}{D}\right)^{\frac{1}{2}} \cos\phi - \left(\frac{A}{D}\right)^{\frac{1}{2}} \sin\phi \right] \right\} \quad \text{(A3-25)}$$

Thus, $H^s_{\rho,i}$ and $H^s_{\phi,i}$ are described by Equations (A3-23) and A3-24) for radiation from an infinitesimal HED at any point along the x axis. A half wave HED can be assumed to consist of an infinite sum of infinitesimal HED's located at distances x_i along the antenna length. The amplitude of these infinitesimal HED's are described by letting a_t be a function of the distance x from the phase center, and dx be the length of each infinitesimal HED. Thus, the amplitudes of the continuous array of

infinitesimal HED's can be related to the current distribution of the half wavelength HED antenna by the equation:

$$a_t = I(x)\,dx \tag{A3-25}$$

and the surface field components H_ρ^S and H_ϕ^S, due to radiation from a half wavelength HED antenna can be represented by the equations:

$$H_\rho^S = \int_{-\frac{L}{2}}^{\frac{L}{2}} dx\ I(x) \left\{ L_\rho' \left(\frac{A}{D}\right)^{\frac{1}{2}} \left[\left(\frac{A}{D}\right)^{\frac{1}{2}} \cos\phi + \left(\frac{B}{D}\right)^{\frac{1}{2}} \sin\phi \right] + L_\phi' \left(\frac{B}{D}\right)^{\frac{1}{2}} \left[\left(\frac{B}{D}\right)^{\frac{1}{2}} \cos\phi - \left(\frac{A}{D}\right)^{\frac{1}{2}} \sin\phi \right] \right\} \tag{A3-26}$$

and

$$H_\phi^S = \int_{-\frac{L}{2}}^{\frac{L}{2}} dx\ I(x) \left\{ L_\phi' \left[\left(\frac{A}{D}\right)^{\frac{1}{2}} \cos\phi + \left(\frac{B}{D}\right)^{\frac{1}{2}} \sin\phi \right] \left(\frac{A}{D}\right)^{\frac{1}{2}} - L_\rho' \left(\frac{B}{D}\right)^{\frac{1}{2}} \left[\left(\frac{B}{D}\right)^{\frac{1}{2}} \cos\phi - \left(\frac{A}{D}\right)^{\frac{1}{2}} \sin\phi \right] \right\} \tag{A3-27}$$

Far from the source, the following approximations can be made:

$$r_x \cong r - x\cos\phi \tag{A3-28}$$

and

$$\phi' = \phi \tag{A3-29}$$

and H_ρ^s and H_ϕ^s become:

$$H_\rho^s \cong \int_{-\frac{L}{2}}^{\frac{L}{2}} dx\, I(x)\, L_\rho' \sin\phi \tag{A3-30}$$

$$H_\phi^s \cong \int_{-\frac{L}{2}}^{\frac{L}{2}} dx\, I(x)\, L_\phi' \cos\phi \tag{A3-31}$$

Substituting Equations (A3-21) and (A3-22) for L_ρ' and L_ϕ', Equations (A3-30) and (A3-31) become:

$$H_\rho^s \cong \int_{-\frac{L}{2}}^{\frac{L}{2}} dx \left[I(x) \sin\phi \right] \cdot \left[-2 \left[\frac{H_{-1}}{H_1 K} \frac{K_{c_1}}{\pi_x} G_1^x - \frac{H_1}{H_{-1}(-jK)} \frac{K_{c_{-1}}}{\pi_x} G_{-1}^x \right] \right] \tag{A3-32}$$

$$H_\phi^s \cong \int_{-\frac{L}{2}}^{\frac{L}{2}} dx \left[I(x) \cos\phi \right] \cdot 2 \left[\frac{\epsilon_{-1}}{\epsilon_1 K} \frac{K_{c_1}}{\pi_x} G_1^x - \frac{\epsilon_1}{\epsilon_{-1}(-jK)} \frac{K_{c_{-1}}}{\pi_x} G_{-1}^x \right] \tag{A3-33}$$

Noting that in Equation (A3-27) the correction term x cos ϕ can be neglected in the calculation of the amplitudes, but not the phases of the surface field terms H_ρ^s and H_ϕ^s, Equations (A-32) and (A3-33) become:

$$H_\rho^s = -2\sin\phi\left\{\frac{H_{-1}}{H_1 K}\frac{K_{c_1}}{\pi}G_1\int_{-L/2}^{L/2} dx\, I(x)\, e^{jK_{c_1}x\cos\phi}\right.$$

$$\left. -\frac{H_1}{H_{-1}(-jK)}\frac{K_{c_{-1}}}{\pi}G_{-1}\int_{-L/2}^{L/2} dx\, I(x)\, e^{jK_{c_{-1}}x\cos\phi}\right\} \qquad \text{(A-34)}$$

$$H_\phi^s = 2\cos\phi\left\{\frac{\epsilon_{-1}}{\epsilon_1 K}\frac{K_{c_1}}{\pi}G_1\int_{-L/2}^{L/2} dx\, I(x)\, e^{jK_{c_1}x\cos\phi}\right.$$

$$\left. -\frac{\epsilon_1}{\epsilon_{-1}(-jK)}\frac{K_{c_{-1}}}{\pi}G_{-1}\int_{-\frac{L}{2}}^{\frac{L}{2}} dx\, I(x)\, e^{jK_{c_{-1}}x\cos\phi}\right\} \qquad \text{(A-35)}$$

The integral common to both equations (A3-34) and (A3-35) is:

$$I = \int_{-\frac{L}{2}}^{\frac{L}{2}} I(x)\, e^{j k_{c_i} x \cos\phi}\, dx \tag{A3-36}$$

where $i = \pm 1$ (A3-37)

and $$I(x) = I_1 e^{j\psi_1} \cos k_{eff} x + I_2 e^{j\psi_2} (\sin k_{eff}|x| - 1) \tag{A3-38}$$

Using the exponential form of the cosine, the first term of equation (A3-36) becomes:

$$I' = \frac{I_1}{2} e^{j\psi_1} \int_{-\frac{L}{2}}^{\frac{L}{2}} \left(e^{j k_{eff} x} + e^{-j k_{eff} x} \right) e^{j k_{c_i} x \cos\phi}\, dx \tag{A3-39}$$

$$= I_1 e^{j\psi_1} \frac{L}{2} \left\{ \frac{\sin\left[(k_{eff} + k_{c_i} \cos\phi) \frac{L}{2} \right]}{(k_{eff} + k_{c_i} \cos\phi) \frac{L}{2}} + \frac{\sin\left[(k_{eff} - k_{c_i} \cos\phi) \frac{L}{2} \right]}{(k_{eff} - k_{c_i} \cos\phi) \frac{L}{2}} \right\} \tag{A3-40}$$

and for

$$k_{eff} \frac{L}{2} = \frac{\pi}{2} \tag{A3-41}$$

equation (A3-40) can be written as:

$$I' = \left(I_1 \frac{L}{2}\right) e^{j\psi_1} M_i\left(\frac{\pi}{2}, \phi\right)$$

(A3-42)

where

$$M_i\left(\frac{\pi}{2}, \phi\right) = \frac{4}{\pi} \left\{ \frac{\cos\left[\sqrt{\frac{\epsilon_i}{\epsilon_{eff}}} \frac{\pi}{2} \cos\phi\right]}{1 - \frac{\epsilon_i}{\epsilon_{eff}} \cos^2\phi} \right\}$$

(A3-43)

Following the same procedure, the second term of equation (A3-36) can be written as:

$$I'' = -I_2 e^{j\psi_2} \frac{L}{2} \left\{ N_i\left(\frac{\pi}{2}, \phi\right) + O_i\left(\frac{\pi}{2}, \phi\right) \right\}$$

(A3-44)

where

$$N_i\left(\frac{\pi}{2}, \phi\right) = \frac{4}{\pi} \left\{ \frac{\sqrt{\frac{\epsilon_i}{\epsilon_{eff}}} \frac{\pi}{2} \cos\phi \sin\left[\sqrt{\frac{\epsilon_i}{\epsilon_{eff}}} \frac{\pi}{2} \cos\phi\right]}{1 - \frac{\epsilon_i}{\epsilon_{eff}} \cos^2\phi} \right\}$$

(A3-45)

and

$$O_i\left(\frac{\pi}{2},\phi\right) = \frac{4}{\pi}\left\{\frac{\sin\sqrt{\frac{\epsilon_i}{\epsilon_{eff}}}\,\frac{\pi}{2}\cos\phi}{\sqrt{\frac{\epsilon_i}{\epsilon_{eff}}}\cos\phi}\right\}$$

(A3-46)

Then, equation (A3-36) can be written as:

$$I = \frac{L}{2} I_1 e^{j\psi_1} M_i\left(\frac{\pi}{2},\phi\right) - I_2 e^{j\psi_2}\left(N_i\left(\frac{\pi}{2},\phi\right) + O_i\left(\frac{\pi}{2},\phi\right)\right)$$

(A3-47)

$$= \left(\sqrt{I_1^2+I_2^2}\,\frac{L}{2}\right)\left\{\frac{I_1 e^{j\psi_1}}{\sqrt{I_1^2+I_2^2}} M_i\left(\frac{\pi}{2},\phi\right) - \frac{I_2 e^{j\psi_2}}{\sqrt{I_1^2+I_2^2}}\left(N_i\left(\frac{\pi}{2},\phi\right) + O_i\left(\frac{\pi}{2},\phi\right)\right)\right\}$$

$$= \left(\sqrt{I_1^2+I_2^2}\right)\left(\frac{L}{2}\right) M_i^{\mathcal{F}}\left(\frac{\pi}{2},\phi\right)$$

(A3-48)

and, in the far field, the components H_ρ^{sh} and H_ϕ^{sh} per unit dipole moment are represented by the equations:

$$H_\rho^{sm} = -2\sin\phi\left\{\frac{H_{-1}}{H_1 K}\,\frac{k_{c_1}}{\pi}\,G_1 M_i^{\mathcal{F}}\left(\frac{\pi}{2},\phi\right) - \frac{H_1}{H_{-1}(-jK)}\,\frac{k_{c_{-1}}}{\pi}\,G_{-1} M_{-1}^{\mathcal{F}}\left(\frac{\pi}{2},\phi\right)\right\}$$

(A3-49)

$$H_\phi^{sm} = 2\cos\phi\left\{\frac{\epsilon_1}{\epsilon_{-1} K}\,\frac{k_{c_1}}{\pi}\,G_1 M_1^{\mathcal{F}}\left(\frac{\pi}{2},\phi\right) - \frac{\epsilon_1}{\epsilon_{-1}(-jK)}\,G_{-1} M_{-1}^{\mathcal{F}}\left(\frac{\pi}{2},\phi\right)\right\}$$

(A3-50)

The vertical magnetic surface field component H_z^{sn} obtained from the H_ρ^{sn} (TE) field by applying equation (A3-48) to equation (2-90) with the result:

$$H_z^{SM} = -2\sin\phi \frac{H_{-1}^2 K_{c_1}^2}{H_1 K^2 r}\left[G_1 M_1^{\xi}\left(\tfrac{\pi}{2},\phi\right) - \left(\frac{H_1}{H_{-1}}\right)\left(\frac{K_{c_{-1}}}{K_{c_1}}\right)^2 G_{-1} M_{-1}^{\xi}\left(\tfrac{\pi}{2},\phi\right)\right] \tag{A3-51}$$

At the surface, equations (A3-45) and (A3-46) are valid only far from the source, since the horizontal tangential components are geometrically coupled near the source, as illustrated in equations (A3-26) and (A3-27). However, the vertical magnetic field component is effectively decoupled from the horizontal magnetic field components at the surface and equation (A3-51) is valid in the same region as equation (2-90); i.e. at distances of one or two wavelengths from the source where higher order field terms can be neglected.

APPENDIX A-4

Array Factor for Radiation Patterns

With reference to Figure 3-10, at a point $P(r,\theta,\phi)$ far from the transmitting antenna and far from the surface, the array factor can be written as:

$$M_i^{\xi}(\theta,\phi) = \frac{I_1}{\sqrt{I_1^2+I_2^2}} e^{j\psi_1}\left[\frac{4}{\pi}\left\{\frac{\cos\left(\sqrt{\frac{\epsilon_i}{\epsilon_{eff}}}\frac{\pi}{2}\sin\theta\cos\phi\right)}{\left(1-\frac{\epsilon_i}{\epsilon_{eff}}\sin^2\theta\cos^2\phi\right)}\right\}\right]$$

$$-\frac{I_2}{\sqrt{I_1^2+I_2^2}} e^{j\psi_2}\left[\frac{4}{\pi}\left\{\frac{\left(\sqrt{\frac{\epsilon_i}{\epsilon_{eff}}}\sin\theta\cos\phi\right)\left(\sin\left(\sqrt{\frac{\epsilon_i}{\epsilon_{eff}}}\frac{\pi}{2}\sin\theta\cos\phi\right)\right)}{\left(1-\frac{\epsilon_i}{\epsilon_{eff}}\sin^2\theta\cos^2\phi\right)}\right\}\right]$$

$$-\frac{I_2}{\sqrt{I_1^2+I_2^2}} e^{j\psi_2}\left[\frac{4}{\pi}\left\{\frac{\sin\left(\sqrt{\frac{\epsilon_i}{\epsilon_{eff}}}\frac{\pi}{2}\sin\theta\cos\phi\right)}{\sqrt{\frac{\epsilon_i}{\epsilon_{eff}}}\sin\theta\cos\phi}\right\}\right] \qquad \text{(A4-1)}$$

which can be written in the form:

$$M_i^{\xi}(\theta,\phi) = \frac{I_1}{\sqrt{I_1^2+I_2^2}} e^{j\psi_1} M_i(\theta,\phi) - \frac{I_2}{\sqrt{I_1^2+I_2^2}} e^{j\psi_2} \left(N_i(\theta,\phi) + O_i(\theta,\phi)\right)$$

(A4-2)

Following the procedure described in Section 2.3, the power radiated per unit of solid angle from a half wavelength HED can be represented by the equation:

$$\frac{dP^{L}}{d\Omega_i}(\theta,\phi) = \sqrt{\frac{\mu_i}{\epsilon_i}} \left| \frac{k_i}{k_{c_i}} H'_{\phi,TM} \right| \left| M_i^{\xi}(\theta,\phi) \right|^2 + \sqrt{\frac{\epsilon_i}{\mu_i}} \left| \frac{k_i}{k_{c_i}} E'_{\phi,TE} \right| \left| M_i^{\xi}(\theta,\phi) \right|^2$$

(A4-3)

where E'_{ϕ} and H'_{ϕ} are described by equations (2-92) through (2-95) and θ is written in terms of the propagation constants k_i and k_{ci} and:

$$\left| M_i^{\xi} \right|^2 = \left(M_i^{\xi}\right)\left(M_i^{\xi}\right)^*$$

(A4-4)

$$= \frac{I_1^2}{I_1^2+I_2^2} M_i + \frac{I_2^2}{I_1^2+I_2^2} \left(N_i + O_i\right)$$

(A4-5)

Note that for:

$$I_1^2 \gg I_2^2$$

$$\left|M_i^{\xi}\right|^2 \cong M_i^2 \tag{A4-6}$$

(A4-7)

To determine the gain of the half wavelength antenna relative to an isotropic source, the power per unit of solid angle is integrated over all solid angles as illustrated in equation (A4-8).

$$P_i = \int_0^{2\pi} d\phi \int_{k_t/k_{c_i}=0}^{1} \frac{dk_t}{k_{c_i}} \frac{k_t}{k_{c_i}} \frac{k_{c_i}}{k_i} \frac{dP}{d\Omega}^{L}(\theta,\phi)$$

(A4-8)

and the gain is represented by the equation:

$$G = \frac{\frac{dP}{d\Omega_i}^{L}(\theta,\phi)}{\frac{1}{4\pi}\sum_{i=\pm 1} P_i} \tag{A4-9}$$

SELECTED LIST OF REFERENCES

1. Annan, A.P., "Radio Interferometry Depth Sounding," M.S. Thesis, Department of Physics, University of Toronto, January 1970.

2. Cooper, W. W., "Patterns of Dipole Antenna on Stratified Media," Center for Space Research Report TR 71-3, Massachusetts Institute of Technology, July 1971.

3. Sinha, Ajit K., "Theoretical Studies of the Radio-frequency Interferometry Method of Sounding," Department of Physics, University of Toronto, March 1971.

4. Sommerfeld, A. N. (1909 and 1926) The Propagation of Waves in Wireless Telegraphy, Ann. Phys., Series 4, 28, 655; 81, 1135.

5. King, R.W.P. and Harrison, C.W., Antenna and Waves, M.I.T. Press, Cambridge, Massachusetts, 1969.

6. Tsao, C.K.H., "Distributed Shunt Admittance of Horizontal Dipole over Lossy Ground," Proceedings of Conference on Environmental Effects on Antenna Performance, Vol. I, CFSTI, July 1969.

7. Kraus, John D., Antennas, McGraw-Hill Book Co., New York, 1950.

8. Nanda, V. P. and Groener, E. J., A Study of Theoretical Interference Plots for Horizontal Electric Dipole In Three Layer Geometry and Estimation of Medium Parameters, Center for Space Research Memorandum, Massachusetts Institute of Technology, September 1971.

9. van der Pol, B. and Niessen, K. F., On the Spatial Waves of a Vertical Dipole on a Plane Earth, Ann. Phys. 10, 485 (1931).

10. Wait, J.R., Electromagnetic Waves in Stratified Media, Pergamon Press, 1970.

11. Collin, Field Theory of Guided Waves, McGraw-Hill, 1960.

12. Baños, A., Electromagnetic Fields of a Dipole in a Conducting Half-Space, Monographs on Electromagnetic Waves, Pergamon Press, 1965.

13. Rossiter, J.R., "Interferometry Depth Sounding on the Athabasca Glacier," M.S. Thesis, Department of Physics, University of Toronto, March 1971.

14. Rossiter, J.R., Watts, R.D. and Strangway, D.W., Preliminary Science Results Athabasca Glacier, Summer 1971, Surface Electrical Properties Experiment Progress Report for September 1971, prepared by Center for Space Research, M.I.T., Cambridge, Massachusetts, September 1971.